

The use of chiral nematic thin films containing
responsive dopants as time-integrating sensors

Submitted in partial fulfillment of the requirements of the Degree
of Doctor of Philosophy

Pascal Cachelin MChem MRes

August 2017

0.1 Statement of originality

I, Pascal André Cachelin, confirm that the research included within this thesis is my own work or that where it has been carried out in collaboration with, or supported by others, that this is duly acknowledged below and my contribution indicated. Previously published material is also acknowledged below.

I attest that I have exercised reasonable care to ensure that the work is original, and does not to the best of my knowledge break any UK law, infringe any third party's copyright or other Intellectual Property Right, or contain any confidential material.

I accept that the College has the right to use plagiarism detection software to check the electronic version of the thesis.

I confirm that this thesis has not been previously submitted for the award of a degree by this or any other university.

The copyright of this thesis rests with the author and no quotation from it or information derived from it may be published without the prior written consent of the author.

Signature:

Date:

Details of collaboration and publications:

Dr. Joshua Green, Prof. Martin Heeney, Imperial College London (Cachelin et al. (2016a))

Dr. Hitesh Khandewal, Technische Universiteit Eindhoven

Contents

0.1	Statement of originality	1
1	Abstract	6
2	Structure of the thesis	20
3	Literature Review	22
3.1	Liquid crystalline mesophases	22
3.1.1	Nematic liquid crystals	26
3.1.2	Smectic Liquid Crystals	29
3.1.3	Discotic liquid crystals	32
3.1.4	Chiral nematic liquid crystals	34
3.2	Polymer stabilised liquid crystals	39
3.2.1	Types of polymer stabilised liquid crystals	39
3.3	Liquid crystal sensors	44
3.3.1	Interfacial change driven sensors	46
3.3.2	Bulk property change driven sensors	48
3.4	Conclusion	68
4	Theoretical model	70
4.1	Background	70
4.2	Overview	71

4.2.1	Varying helical twisting power (β)	73
4.2.2	Varying the concentration of dopant (c_w)	84
4.2.3	Modelling photodegradation	86
4.2.4	Change in optical activity	88
4.3	Varying the enantiomeric excess (e_e)	91
4.4	Conclusion	93
5	Optical monitoring of ketone vapours	95
5.1	Introduction	95
5.2	Background	96
5.2.1	Acetone	96
5.2.2	Non-liquid crystalline sensors for acetone	99
5.2.3	Liquid crystalline sensors for acetone	100
5.3	Experimental	103
5.3.1	Reaction between acetone and phenylhydrazine	105
5.3.2	Complexation of phenylhydrazine and 1-isopropylidene- 2-phenylhydrazine with TADDOL	105
5.3.3	Exposure of TADDOL/PH complex to acetone vapour	106
5.3.4	Exposure of TADDOL/PH complex to other ketone vapours.	106
5.3.5	Exposure of TADDOL/PH complex to other common sol- vents.	106
5.4	Results and Discussion	107
5.4.1	Reaction between acetone and phenylhydrazine	107
5.4.2	Complexation of phenylhydrazine and 1-isopropylidene- 2-phenylhydrazine with TADDOL	108
5.4.3	Exposure of TADDOL/PH complex to acetone vapour	111
5.4.4	Exposure of TADDOL-PH complex to other ketones	114

5.4.5	Exposure of TADDOL/PH complex to other common sol- vents.	115
5.5	Conclusion	116
6	Optical monitoring of UV dose by photochemical degradation	119
6.1	Introduction	119
6.2	Experimental	121
6.2.1	UV and CD studies of BINOL under HI UV illumination .	121
6.2.2	N* LC thin films containing BINOL as a dopant	121
6.2.3	Exposure of N* LC thin films containing BINOL to HI UV light	121
6.2.4	Dose effect and sensitivity of N* LC thin films containing BINOL	122
6.2.5	Thermal cross-sensitivity	122
6.3	Results and Discussion	122
6.3.1	UV and CD studies of BINOL under HI UV illumination .	122
6.3.2	N* LC thin films containing BINOL as a dopant	126
6.3.3	Exposure of N* LC thin films containing BINOL to HI UV light	126
6.3.4	Dose effect and sensitivity of N* LC thin films containing BINOL	128
6.3.5	Thermal cross-sensitivity	131
6.4	Conclusion	134
7	Optical monitoring of UV dose by photoisomerisation	136
7.1	Introduction	136
7.2	Experimental	138
7.2.1	UV response of dopant 1	138

7.2.2	Response of N* LC thin films containing 1 to UV light . .	138
7.2.3	UV sensitivity of 1	139
7.2.4	Cross sensitivity	139
7.2.5	Tuning sensitivity	139
7.3	Results and discussion	140
7.3.1	UV response of dopant 1	140
7.3.2	Response of N*LC thin films containing 1 to UV light . .	140
7.3.3	UV sensitivity of 1	142
7.3.4	Cross sensitivity	144
7.3.5	Tuning sensitivity	145
7.4	Conclusion	147
8	Conclusions & future work	149
8.1	Summary of main points	149
8.2	Problems and recommendations	150
8.2.1	Reaction times	150
8.2.2	Cross-sensitivity	152
8.2.3	Sensitivity	157
8.3	Potential systems	158
8.3.1	‘Click’ reactions	158
8.3.2	Loss of optical activity	160
8.4	Computer simulation	162
8.5	Conclusion	162

Chapter 1

Abstract

Chiral nematic thin films containing responsive dopants have previously been considered as sensors and dosimeters. Some systems have been developed, with mixed results. The investigation so far has been piecemeal, with little attention paid towards understanding the properties that govern how these sensors operate. By carefully considering these properties, we believe that it is possible to predict the effectiveness of a sensor, and therefore a framework can be established which would allow only sensors with significant potential to be investigated.

The applications of a variety of chiral nematic thin films incorporating responsive dopants is modelled and then investigated experimentally. The systems chosen for investigation were selected using the criteria of commercial potential and synthetic simplicity. In each case it was found that the behaviour of these systems could be predicted well from simple experimental data.

The systems chosen for investigation were judged on the basis of two key criteria:

- They must be systems that deal with a target that is of commercial interest, so that performance expectations for ‘real-life’ applications can be given at the start of the research process.

- They must be manufactured only using materials and processes that are commercially available.

These limitations were chosen to highlight the conditions under which such a model would be expected to operate.

In this work, a successful model that predicts sensors behaviour from basic experimental information was developed and shown to match well with experimental results. In the process, three new sensing systems were developed, all with potential commercial significance. Additionally, some observations regarding the methods of operation which are most likely to result in high sensitivity and low cross-sensitivity have been made.

List of abbreviations

β		Helical Twisting Power
ACGIH	American Conference of Government Industrial Hygienists	
BINOL		bis-2-naphthol
c_w		Concentration by Weight
CD		Circular Dichroism
CNT		Carbon Nanotube
CuAAC	Copper (I) catalysed Azide-Alkyne Cycloaddition	
DKA		Diabetic Ketoacidosis
DLC		Discotic Liquid Crystal
DNA		Deoxyribonucleic Acid
e_e		Enantiomeric Excess
GC-MS		Gas Chromatography - Mass Spectrometry
HSE	(United Kingdom) Health and Safety Executive	
IPN		Interpenetrating Polymer Network

IR	Infrared radiation
ITO	Indium Tin Oxide
LC	Liquid Crystal
LCD	Liquid Crystal Display
MBBA	N-(4-methoxybenzylidene)-4-butylaniline
N* (LC)	Chiral Nematic (Liquid Crystal)
NMR	Nuclear Magnetic Resonance
<i>p</i>	Helical Pitch
PA	1-isopropylidene-2-phenylhydrazine
PAA	para-azoxyanisole
PDLC	Polymer Dispersed Liquid Crystal
PH	Phenylhydrazine
PNS(N*)LC	Polymer Network Stabilised (Chiral Nematic) Liquid Crystal
POM	Polarised Optical Microscopy
PSCT	Polymer Stabilised Cholesteric Texture
PSLC	Polymer Stabilised Liquid Crystal
QCMB	Quartz Crystal Microbalance
RMS	Root Mean Square
RSS	Root Sum of Squares
S _A	Smectic A mesophase
SEM	Scanning Electron Microscopy
STEL	Short Term Exposure Limit
T1DM	Type 1 Diabetes Mellitus
TADDOL	$\alpha,\alpha,\alpha',\alpha'$ -tetraaryl-2,2-disubstituted-1,3-dioxolane-4,5-dimethanol
TWA	Time Weighted Average
UV	Ultraviolet radiation
VOC	Volatile Organic Compound

XRD

X-ray Diffraction

List of Figures

3.1	The mesophasic behaviour of <i>para</i> -azoxyanisole.	23
3.2	The mesophasic behaviour of cholesterol myristate.	23
3.3	A schematic of the solid, liquid crystalline and liquid phases. The rods show the alignment of the long axis of the mesogen.	24
3.4	A graph illustrating the impact of temperature on the order parameter (S). T_{iso} refers to the nematic-isotropic point.	26
3.5	Schematic showing the polarisation of light after passing through crossed polarisers without a liquid crystal intermediary. The horizontal line indicates the direction of propagation.	27
3.6	A schematic showing the impact on the polarisation of light by incorporating a twisted nematic LC thin film between crossed polarisers. The horizontal line indicates the direction of propagation.	28
3.7	An image of a nematic thin film displaying the classic threading associated with the mesophase. Creative Commons: Prof. Clyne/DoITPoMS	28
3.8	The compounds and composition of the liquid crystal mixture E7. The actual composition can vary by manufacturer. Zakerhamidi et al. (2014).	29
3.9	Schematic of the smectic A mesophase.	30

3.10	A schematic indicating Bragg reflection from a regularly oriented crystalline substance.	31
3.11	XRD diffraction pattern associated with the crystalline (lower right), smectic (lower left), nematic (upper right) and isotropic liquid (upper left) phase of LC M24. Reproduced from [Azároff (1980)].	32
3.12	An image of a smectic A thin film, displaying the characteristic ‘fanning’ pattern associated with the mesophase. Viewed through crossed polarisers.	33
3.13	The structure of tricycloquinazoline.	33
3.14	Schematic showing the structure of the nematic (N_D) and columnar (N_C) mesophases of the discotic mesogens.	34
3.15	A schematic of the N^* mesophase.	36
3.16	A polarised optical micrograph of an aligned chiral nematic thin film. Cachelin et al. (2016b).	38
3.17	An SEM image showing bubbles of LC isolated within the polymer (grey background). Reproduced from [Yamagishi et al. (1989)].	40
3.18	The difference in the alignment of the director in on and off states of PDLC visualised. Reproduced from [Bloisi and Vicari (2003)].	41
3.19	Reactive Mesogens 62 and 257, two examples of monomers for the creation of PNS-LCs.	42
3.20	Schematic showing the (dashed) hydrogen bonds stabilising a phenylic carboxylic acid dimer.	44
3.21	Schematic showing the impact of cis-trans isomerisation on the alignment of the liquid crystal molecules above it [Ichimura et al. (1988)].	47
3.22	Schematic indicating functional surface-based sensing of chemical analytes. Reproduced from [Shah and Abbott (2003)].	47

3.23	The chemical structure of N-(4-Methoxybenzylidene)-4-butylaniline (MBBA).	49
3.24	A plot of the inverse pitch against the concentration of heroin for LCs MBBA (solid line) and PCH (dashed line) [Bertocchi et al. (1984)].	50
3.25	The change in the wavelength of the scattering maximum as a function of temperatures for blends of cholesterol derivatives [Ferguson et al. (1966)].	51
3.26	The percentage change in absorbance at λ_{max} when exposed to 0.1 wt% solvent vapour plotted against the molecular mass of the solvent [Mujahid et al. (2010)].	53
3.27	The percentage change in absorbance at λ_{max} when exposed to 0.1 wt% solvent vapour plotted against the mass-normalised sensor response [Mujahid et al. (2010)].	54
3.28	A plot showing the change in both the wavelength of the reflection band ($\Delta\lambda$) and the electrical resistance of a hybrid N*LC-CNT film as the concentration of acetone vapour changes. [Chang et al. (2012b)].	55
3.29	The reaction between a trifluoroacetate and a primary amine.	56
3.30	The response of a sensor containing a trifluoroacetyl functionalised cholesterol derivative to 1-butylamine and diethylamine vapours [Kirchner et al. (2006)].	56
3.31	A graph showing the linear relationship between detection limits and molecular mass (units gmol^{-1} of primary amine sensors [Sutarlie et al. (2010)]. Chain lengths are marked as C3-C10.	57

3.32	Graph showing the change in reflection maximum (λ_{max}) and thickness in response to changes in relative humidity. Stumpel et al. (2015)	59
3.33	The thermally controlled display developed by Hu et al. (2009). The inset shows images of the sample described by the inset graph, labelled Sample 2.	61
3.34	An illustration of a) the embossing process and b) the relaxation of the pitch above the glass transition temperature [Davies et al. (2013)].	62
3.35	A crown-ether functionalised cholesterol derivative [Shinkai et al. (1990)].	62
3.36	A plot of reflection maxima (λ_R) against metal thiocyanate concentration for a variety of alkali metals [Shinkai et al. (1990)]. . .	64
3.37	Reaction scheme for the formation of a BINOL dimer that is sensitive to water vapour [Saha et al. (2012a)].	65
3.38	Illustration of the transoid and cisoid BINOL forms, which are dependent on the dihedral angle θ . [Eelkema and Feringa (2006)].	65
3.39	The change in wavelength of the reflection maximum as observed as a function of time exposed to air of 75% relative humidity. [Saha et al. (2012b)]	66
3.40	The reaction between 1,2-diphenylhydrazine and CO ₂ , as used by Han et al. (2010b).	67
3.41	The complex between TADDOL and 1,2-diphenylhydrazine that formed the responsive component of the CO ₂ sensor developed by Han et al. (2010b).	67
4.1	A graph showing the effect of changes in β_i on the value of Δp . e_e and c_w are assumed to be constant.	72

4.2	Optical microscopy images of a chiral nematic liquid crystal in a wedge cell showing Grandjean steps. Taken through crossed polarisers.	74
4.3	Illustration of the Grandjean-Cano method using a wedge cell. Podolsky et al. (2008)	74
4.4	Optical microscopy image of a chiral nematic liquid crystal under a lens showing the Grandjean steps. Taken through crossed polarisers.	75
4.5	A graph comparing the theoretical values, with errors obtained by the RSS and RMS methods, with experimental results from Chapter 5. The error bars on the experimental data indicate the measurement uncertainty of ± 0.5 nm.	80
4.6	A comparison of the theoretical and experimental values of $\Delta\lambda$ for the UV sensor based on the photodegradation of R,R'-bis-2-naphthol. Experimental details are included in Chapter 6.	87
4.7	The reaction between an analyte (A) and a chiral dopant resulting in the formation of an achiral compound.	88
4.8	An illustration of the molecular selectivity of this dopant system. In this case, molecules A and B share a functional moiety that is targeted by the reactive chiral dopant, but are structurally dissimilar.	89
4.9	The reaction between the silicate ester of BINOL and water yielding BINOL. Note the reaction is irreversible, hence this sensor acts as a time integrating sensor, or a dosimeter.	89
4.10	The predicted change in λ_{max} compared to the observed values. N.B. this does not include the contribution from BINOL. Experimental details located in Saha et al. (2012b).	90

4.11	A representation of a stereogenic centre. Note that the two molecules are not superimposable, despite having identical structures.	91
5.1	The ketogenic pathway that results from the breakdown of free fatty acids.	98
5.2	A schematic of a gas detection tube.	101
5.3	The reaction between Brady's reagent and a carbonyl. The colour of the product can be used to determine the type of carbonyl present, and melting point analysis can be used to compare to a library of known carbonyls.	104
5.4	The reaction between PH and acetone, resulting in the formation of the imine product, 1-isopropylidene-2-phenylhydrazine (PA).	105
5.5	The structure and formation of the three dopants discussed. Clockwise from upper right: TADDOL, TADDOL-PH, TADDOL-PA.	105
5.6	Relative abundance of PH and PA over time, as measured by GC intensity. Reaction was carried out without an acid catalyst. Solvent = E7.	107
5.7	¹ H-NMR of the product of the reaction between PH and acetone. The unassigned peaks correspond to unreacted acetone. Solvent is CDCl ₃	108
5.8	¹ H-NMR spectra of (top) TADDOL, (middle) PH and (bottom) TADDOL/PH.	109
5.9	The absorption spectrum of (a) TADDOL (<i>c_w</i> = 3.56), (b) TADDOL-PAc (<i>c_w</i> = 4.01) and (c) TADDOL-PH (<i>c_w</i> = 4.00) in E7 before and after exposure to 10,000 ppm acetone vapour. All spectra recorded at the same temperature (20 °C).	112
5.10	A plot of acetone concentration vs. change in λ_{max} ($\Delta\lambda$).	113

5.11	A plot of ketone analyte against β of the resultant complex with TADDOL-PH.	115
6.1	The CD measurements of solutions of BINOL in toluene after illumination with high intensity UV light ($I = 132.02 \text{ mWcm}^{-2}$). Sample was contained in a quartz cell with path length $l = 1 \text{ cm}$	123
6.2	The UV/Vis absorption spectrum for a 5 wt% solution of (R)-(+)-1,1'-bi(2-naphthol) in toluene. Sample was contained in a quartz cell with path length $l = 1 \text{ cm}$	124
6.3	UV spectrum of BINOL following progressive irradiation with UV light ($I = 132.02 \text{ mWcm}^{-2}$). Sample was contained in a quartz cell with path length $l = 1 \text{ cm}$	125
6.4	The UV/Vis/NIR transmission of 20 μm cells containing 7.5 wt% of BINOL in E7 before and after exposure to high intensity UV light ($I = 0.5 \text{ mWcm}^{-2}$).	127
6.5	The reflection band of a cell containing 12% (R)-(+)-1,1'-bi(2-naphthol) in E7 before and after being exposed to unpolarized direct sunlight (London, 28th June 2016, 11:00 am) for 28 min. $I = 6.67 \text{ mWcm}^{-2}\text{s}^{-1}$. The decreased intensity arises from the use of a LC cell with a small gap (6.8 μm), which limits the number of helical twists present.	128
6.6	The change in λ_{max} ($\Delta\lambda$) as a function of UV dose. UVI = 15.2 mWcm^{-2}	129
6.7	A plot of normalised UV peak intensity at 333 nm against dose.	130
6.8	Predicted c plotted against UV dose.	132
6.9	Comparison of the experimental and theoretical values of $\Delta\lambda_{max}$ for BINOL in E7 as a function of UV dose.	133

6.10	The sensitivity of the BINOL/LC mixture to UV light at different temperatures. This also includes results from different UV sources, demonstrating that the dosimeters are source agnostic.	134
7.1	The UV-induced photo-isomerisation of a functionalised menthone derivative, 1 , received from Philips.	137
7.2	The (<i>E</i>) and (<i>Z</i>) isomers of 1 . Geometry optimised by MM2 method.	138
7.3	The structure of the UV absorbing compound Tinuvin 328.	140
7.4	UV/Vis absorption of a 5% solution of 1 in toluene. Sample was contained in a quartz cell with path length $l = 1$ cm.	141
7.5	The UV/Vis spectra of solutions of 1 following progressive illumination.	141
7.6	The UV/Vis spectra of 1 in LC6553 ($c_w = 0.101$) before and after exposure of UV light for 5 seconds ($UVI = 56.6 \text{ mWcm}^{-2}$).	142
7.7	The UV/Vis spectrum of LC6553 in a $7.7 \mu\text{m}$ gap cell containing anti-parallel ITO electrodes.	143
7.8	The change in λ_{max} for a given UV dose (bottom axis) or exposure time (top axis).	143
7.9	The changes in the value of λ_{max} as a function of exposure time for samples containing 1 exposed to simulated sunlight ($UVI = 6.67 \text{ mW/cm}^2$).	144
7.10	The combined dose response for the two above experiments, with different UV intensities.	145
7.11	The impact of temperature on sensitivity. All samples exposed to simulated sunlight ($UVI = 6.67 \text{ mJcm}^{-2}$) for 15 seconds at a controlled temperature.	146
7.12	The UV/Vis spectra of a mixture containing 0.53 wt% of Tinuvin 328 as a UV absorber. $I = 10.14 \text{ mWcm}^{-2}$	146

8.1	The CuAAC reaction. Unlike the Huisgen's 1,3-dipolar cycloaddition, only the 1,4-isomer is formed, fulfilling the stereospecificity requirement.	159
8.2	The thiol-ene 'click' reaction. The reaction can also proceed as a Michael addition, through the use of a nucleophile or base as a catalyst.	160
8.3	One method of decreasing the optical activity of a chiral compound is through the creation of a mirror plane. Note that a different compound, e.g. R ⁴ -Y, would not result in the formation of a mirror plane.	161
8.4	Cadaverine (1) and putrescine (2). Both molecules result from the decomposition of fish.	161

List of Tables

3.1	Ionic radii and wavelengths of maximum reflection for N*LC films containing crown-ether functionalised cholesterol derivatives when exposed to various anions.	63
4.1	Dopant structure, reflection maxima, weight contribution and enantiomeric excess for the chiral dopant before and after the reaction with acetone. Experimental details, including manufacture, are included in Chapter 5.	78
4.2	Dopant structure, β , RSS error and RMS error for the chiral dopant before and after the reaction with acetone.	79
5.1	The exposure limits set out by the UK and US health and safety bodies for exposure to acetone vapour.	97
5.2	The λ_{max} , c_w , pitch and β for solutions of the dopants in E7.	110
5.3	Values of λ_{max} , pitch and β for a variety of ketone analytes.	114
7.1	The effect of Tinuvin 328 concentration on the sensitivity of the dosimeter.	147

Chapter 2

Structure of the thesis

This work focuses on the sensing applications of the chiral nematic mesophase of liquid crystals by incorporating a variety of reactive dopants. The introduction will therefore be split into two sections. The first will focus on liquid crystalline mesophases, in particular the chiral nematic mesophase, as well as introducing key techniques in the analysis and characterisation of liquid crystalline thin films. The second part will look more explicitly at the sensing applications of liquid crystalline materials, including those based on other mesophases.

In order to establish a strong theoretical framework, as well as explaining the motivation for the different analytes selected, a theoretical model that was developed over the course of my research is included in Chapter 4. This examines the fundamental properties that govern the chiral nematic mesophase, and the impact that different sensing mechanisms can be predicted to have. As part of this section, a predictive model is developed, and then tested against both existing sensors and the sensors developed later in this work.

Afterwards, the individual sensors developed will be discussed individually. This will include the motivation behind the choice of analyte, as well as a brief overview of the sensing technologies that constitute the state-of-the-art within the

field. The experimental procedures follow and the results will be presented and discussed. This constitutes Chapters 4-6.

Due to the nature of the predictions made within the theoretical framework concerning the performance of different sensors, I will also discuss the scope, potential and challenges of future work within this very new field alongside a general conclusion in Chapter 8

I would like to present my thanks to Profs. Cees Bastiaansen and Ton Peijs for their supervision and support of this work. I would also like to thank Dr. Olivier Picot for his advice and support in dealing with the technical aspects of liquid crystal film fabrication. The work on the ketone sensor presented in Chapter 5 could not have been achieved without contribution from Joshua Green and his supervisor Prof. Martin Heeney, who synthesised compounds and performed NMR and GC-MS analyses. Likewise, I am indebted to Dr. Hitesh Khandelwal for the CD data in Chapter 6 and various characterisation techniques in Chapter 7.

Chapter 3

Literature Review

3.1 Liquid crystalline mesophases

Liquid crystals (LCs) represent a unique group of materials, which exhibit both liquid and crystalline properties. More strictly, they are part of a wider class of mesophasic materials that exhibit more than a single phase transition between the crystalline and liquid states. There exist two categories of LC:

- Thermotropic LCs, where the emergence of mesophasic behaviour arises with variations in temperature;
- Lyotropic LCs, where mesophasic behaviour emerges on the addition of a solvent to an otherwise non-mesogenic compound

This work focuses entirely on thermotropic liquid crystals, and as such the explanations and terms introduced below should be understood within this context.

An individual LC might only exhibit a single phase, such as para-azoxyanisole (PAA), an early nematic LC that was critical in the development of liquid crystal displays (Figure 3.1) [Kawamoto (2006); Castellano (2005)]. Conversely, it might

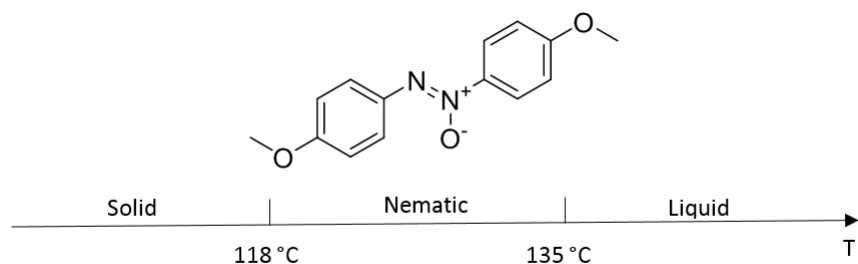


Figure 3.1: The mesophasic behaviour of *para*-azoxyanisole.

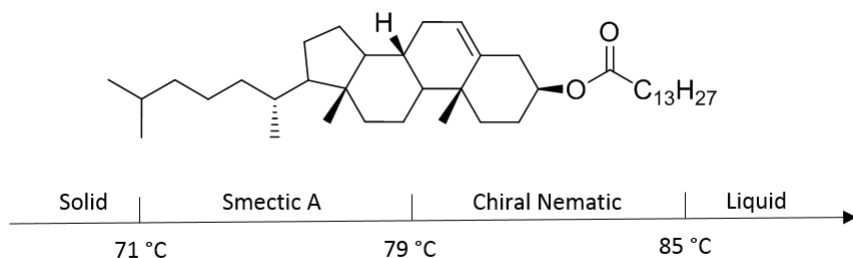


Figure 3.2: The mesophasic behaviour of cholesterol myristate.

exhibit multiple mesophases, as is the case for cholesterol myristate, one of the first LCs identified by Reinitzer in 1888 (Figure 3.2) [Reinitzer (1888)].

Before identifying the individual mesophases mentioned in Figures 3.1 and 3.2, it is important to first understand what makes a LC material different from a liquid or solid and why only some materials exhibit a LC phase. The latter of these depends on the nature of the specific mesophase. In general, molecules which exhibit mesophasic behaviour, called mesogens, consist of an inflexible planar core, such as the fused rings in cholesterol myristate in Figure 3.2, and a flexible ‘tail’. This results in the molecule having a high ‘aspect ratio’, and therefore a high degree of anisotropy in terms of molecular geometry. The actual link between structure and the mesophase is discussed more fully in Shri Singh’s *Liquid Crystals: Fundamentals* [Singh (2002)].

This anisotropy causes the mesogenic behaviour of the material. If the individ-

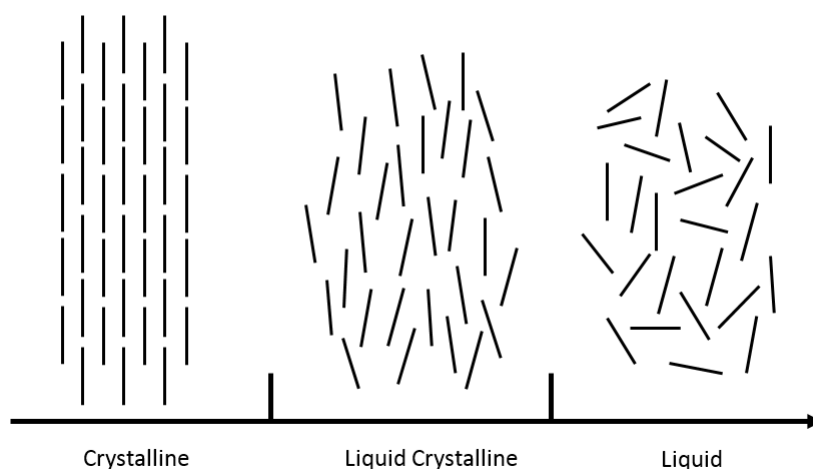


Figure 3.3: A schematic of the solid, liquid crystalline and liquid phases. The rods show the alignment of the long axis of the mesogen.

ual LC molecules are visualised as rods, the separate phases can be categorised by the amount of organisational order they contain. Within the solid phase, the molecules align uniformly, with no variation in the direction of the long axis of the molecule. The molecules are fixed in place. In contrast within the liquid phase the molecules are isotropic, with no common orientation. They also move and rotate freely. The LC phase consists of a middle ground, where there exists some degree of anisotropy with regard to the long axis of the molecule, while individual molecules are still able to move and rotate (Figure 3.3).

Although it is simple to qualitatively state that a liquid crystalline system is more ordered than an isotropic liquid, it is clear that it would be advantageous to be able to quantify the amount of order within a LC phase. In order to do this it is first necessary to determine the axis along which the individual LC molecules are preferentially aligning. One method is to use a unit vector, which would be able to describe the orientation and direction of the molecule. This is termed the director, and is referred to by the notation, \vec{n} . By approximating the structure of the mesogen to that of a rigid rod, however, we place the following restrictions on

the molecule:

1. The molecule is cylindrical around \vec{n} .
2. There is no dipole along the long axis of the molecule, such that \vec{n} and $-\vec{n}$ are equivalent.
3. The direction of \vec{n} is arbitrary in space.

Within the bulk LC material, many different directors will be present. In order to encourage a liquid crystalline material to adopt a common director, and to therefore increase the overall anisotropy within a sample, it is preferential to produce thin films on a substrate that contains grooves to fix the orientation of the LC molecules near to the surface, and to therefore create a template that should extend to the whole film. If the film is too thick, the effect of the alignment layer is lost, and this can be seen by the film turning to the milky colour associated with liquid crystalline materials.

Once the director has been established, it is possible to determine the average variation from the director by measuring the angle (θ) between an individual LC molecule and \vec{n} . Obviously it would be beneficial to have a system where the degree of alignment can be easily determined and compared. For this purpose the order parameter (S) is introduced (Equation 3.1). The benefit of using the order parameter over simply the mean of θ is that it produces an output of $S = 1$ for perfect alignment, and $S = 0$ for a completely isotropic liquid.

$$S = \left\langle \frac{3 \cos^2 \theta - 1}{2} \right\rangle \quad (3.1)$$

The order parameter is particularly useful in describing the transition from the nematic to the liquid phase for thermotropic LCs such as PAA (Figure 3.4). In

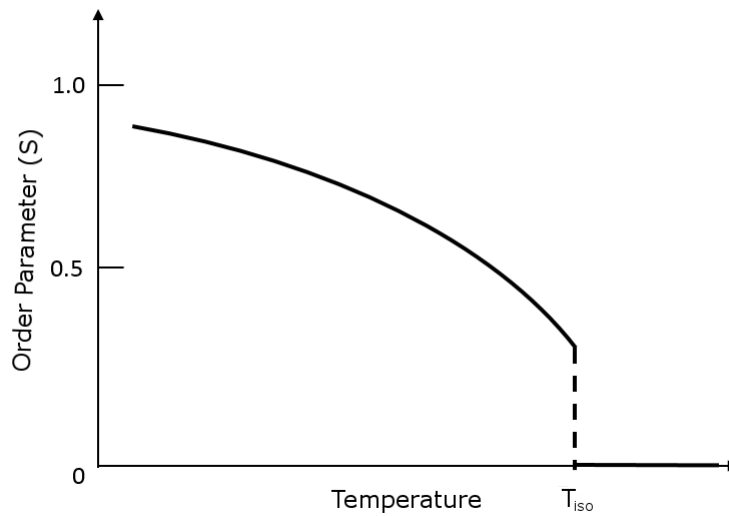


Figure 3.4: A graph illustrating the impact of temperature on the order parameter (S). T_{iso} refers to the nematic-isotropic point.

such cases, the value of S decreases as the temperature increases, with the phase change marking the point where $S = 0$.

The concepts of the order parameter and the director are key in understanding the differences between various mesophases. While there exist a wide range of mesophases, these can be broadly divided into 4 categories: nematic, smectic, discotic and chiral nematic. The first three are briefly discussed below, alongside the introduction of key characterisation techniques for LC materials. After that follows a more in-depth discussion of the chiral nematic phase which forms the basis of the sensors discussed in this work.

3.1.1 Nematic liquid crystals

The nematic phase is the one that most closely matches the ‘rod’ model already discussed. The presence of this mesophase can be confirmed by a variety of methods, but the simplest is to observe a thin film of the LC in question through polarised optical microscopy. If two linear polarisers are held so that the axes

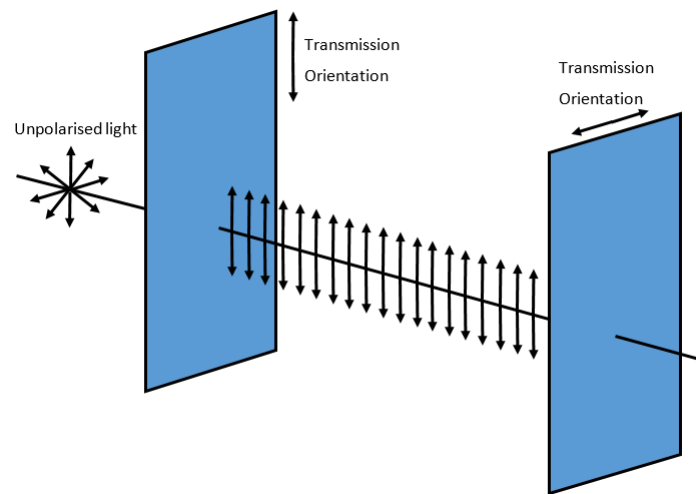


Figure 3.5: Schematic showing the polarisation of light after passing through crossed polarisers without a liquid crystal intermediary. The horizontal line indicates the direction of propagation.

of polarisation are perpendicular, this would normally result in no light passing through, as the polarisation of light that is not filtered out by the first polariser is filtered out by the second (Figure 3.5).

When an aligned LC thin film is incorporated between the polarisers, this behaviour can change. As linearly polarised light can be considered as consisting of orthogonal light waves with a zero phase difference, the polarisation which aligns with the director will propagate through the LC at a different rate to the polarisation which is orthogonal to the director, due to the birefringent nature of LCs. This leads to an elliptical polarisation of light, with some light therefore being able to pass through the second polariser (Figure 3.6).

When viewed through crossed polarisers, nematic LC films display a thread-like texture which is the source of their name (Figure 3.7). These threads arise from disclinations, violations in the rotational symmetry due to a change in the director. Nematic LCs are the mesophase used in most LCD devices, and consequently much research is focussed on their optical and electrical properties.

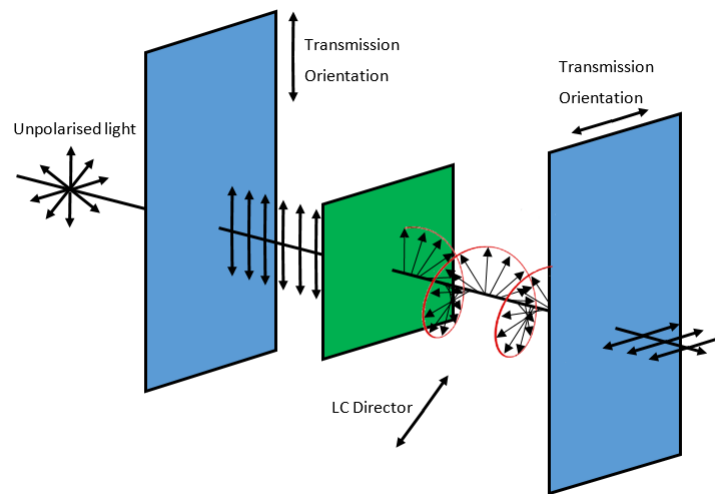


Figure 3.6: A schematic showing the impact on the polarisation of light by incorporating a twisted nematic LC thin film between crossed polarisers. The horizontal line indicates the direction of propagation.

Unlike with smectic mesophases, there exist only two nematic mesophases, simple nematics and biaxial nematics. The latter consist of molecules with three distinct optical axes, as opposed to the two axes seen in simple nematics. These have been observed as both lyotropic [Yu and Saupe (1980)] and thermotropic [Madsen et al. (2004)] phases, although the latter only exists at high temperatures.

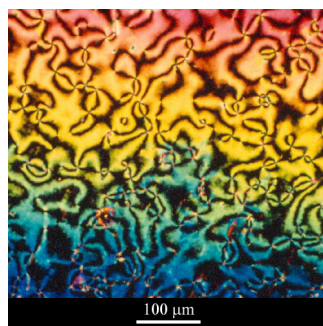


Figure 3.7: An image of a nematic thin film displaying the classic threading associated with the mesophase. Creative Commons: Prof. Clyne/DoITPoMS

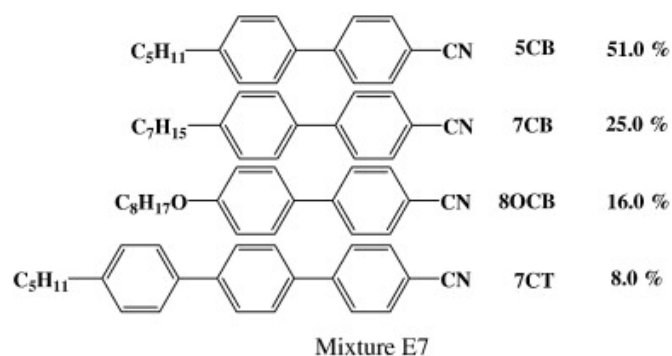


Figure 3.8: The compounds and composition of the liquid crystal mixture E7. The actual composition can vary by manufacturer. Zakerhamidi et al. (2014).

E7

While the nematic phase was initially observed only at raised temperatures, it was quickly found that by mixing together mesogens it was possible to extend the size of the ‘nematic window’, the range of temperatures at which mesogenic mixtures displayed nematic behaviour. One such mixture is E7: a mixture of 4 mesogenic compounds that is widely studied and used, as it is nematic at room temperature. E7 is a mixture of cyano-biphenyls and a cyano-triphenyl, although the composition varies with the manufacturer. The compounds involved and an estimated composition is shown in Figure 3.8.

The nematic window for E7 extends from ca. $-60\text{ }^{\circ}\text{C}$ to $60\text{ }^{\circ}\text{C}$, with an average refractive index of $\bar{n} = 1.52$. The supplier of E7 for this work was Synthon Chemicals GMBH.

3.1.2 Smectic Liquid Crystals

Unlike the nematic or chiral nematic phase, which are mutually exclusive, the various smectic mesophases can and do occur alongside other mesophases, as seen in the phase diagram for cholesterol myristate in Figure 3.2.

Named for the soap-like mechanical properties (From the Latin *smecticus* –



Figure 3.9: Schematic of the smectic A mesophase.

cleansing), these mesophases consists of molecules that possess some degree of positional order, alongside the orientational order of a nematic. It is therefore common for nematic mesogens to exhibit a smectic mesophase between the crystalline and nematic phase.

As can be seen in Figure 3.9, as well as the orientational order present in nematic LCs, smectic LCs form layers of aligned LC molecules. This alignment allows for their investigation by a technique that does not normally work on fluid samples: x-ray diffraction (XRD).

XRD is a technique that relies on the reflection of x-rays from a material, governed by Bragg's Law (Equation 3.2), which relates the wavelength of the reflected beam (λ) to the distance between reflectors (d) and the angle of incident light (θ) (Figure 3.10).

$$n\lambda = 2d\sin\theta \quad (3.2)$$

For isotropic liquids, no diffraction is observed as the spacing between reflectors is irregular, and it is therefore not possible to obtain the constructive interference that gives rise to the diffraction pattern.

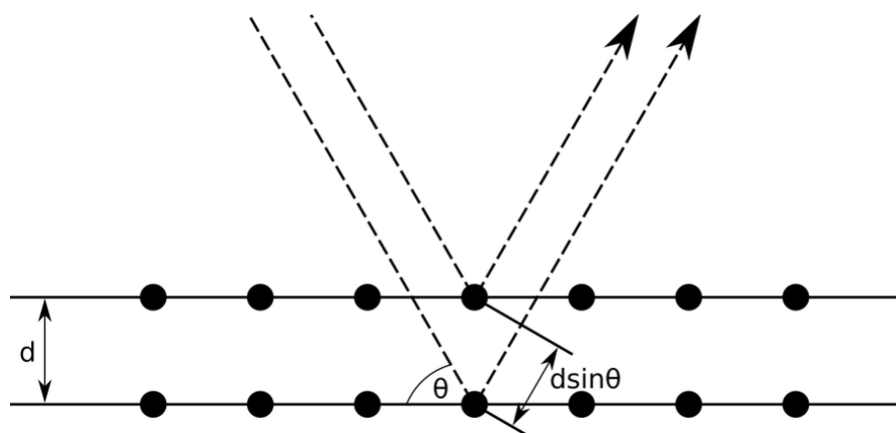


Figure 3.10: A schematic indicating Bragg reflection from a regularly oriented crystalline substance.

Smectic liquid crystals give an intermediate behaviour. Some diffraction is observed, due to the regular spacing between layers of the smectic mesophase, but it is not as distinct as the pattern produced by a crystalline sample, as demonstrated in Figure 3.11.

Due to the regular layers present in smectic LCs, it is possible to determine the spacing between layers by XRD.

XRD is a key technique used in identifying different smectic mesophases. There are many such mesophases, ranging from simple structures such as the smectic A mesophase in Figure 3.9 to more complex chiral mesophases such as the chiral smectic C* phase. These largely vary by the degree of positional or orientational order present, which can be determined by comparing the diffraction patterns produced under XRD.

This contrasts the optical technique introduced in Section 3.1.1, where it can be difficult to determine the precise smectic mesophase purely by looking at the texture displayed through crossed polarisers. Nonetheless, there exists a distinct smectic texture that can easily be used to separate it from other mesophases, with

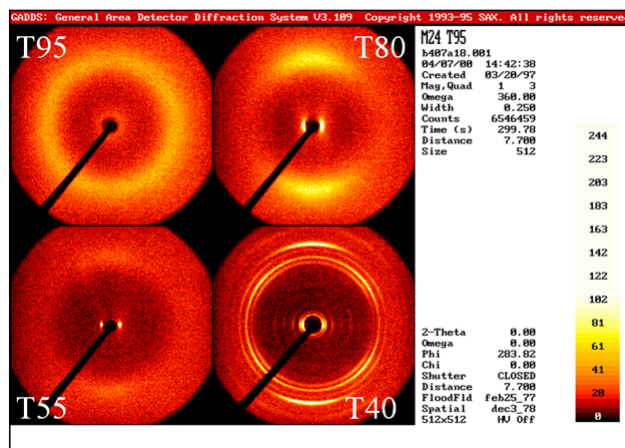


Figure 3.11: XRD diffraction pattern associated with the crystalline (lower right), smectic (lower left), nematic (upper right) and isotropic liquid (upper left) phase of LC M24. Reproduced from [Azároff (1980)].

distinct fan-shaped patterns visible (Figure 3.12). This is known as the focal conic texture, although under certain circumstances a similar texture can be observed in the chiral nematic mesophase.

3.1.3 Discotic liquid crystals

Up until now, the mesogens under discussion have all had a calamitic structure: the liquid crystalline behaviour has been caused by having a rigid-rod type structure. There exists some mesophases which share a different common structure, that of rigid discs. Such materials are referred to as discotic liquid crystals (DLCs), and adopt geometries that are radically different to the calamitic LCs. Unlike calamitic LCs, which are largely investigated for their opto-electronic properties, attention has also been paid to the charge carrying ability of DLCs, including tricycloquinazoline (Figure 3.13) and its derivatives [Kumar et al. (1993); Kaafarani (2011)].

As mentioned previously, DLCs adopt substantially different geometries to calamitic LCs, due to the lack of a long axis around which to preferentially order.

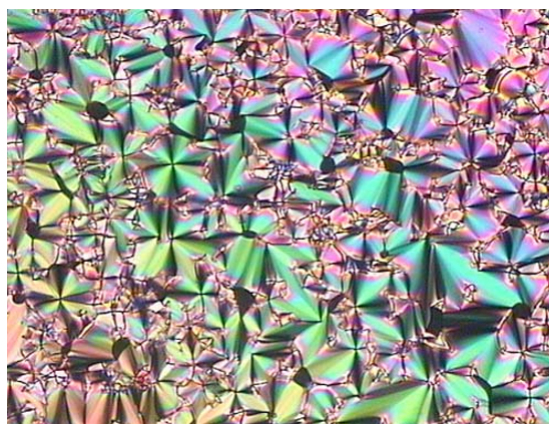


Figure 3.12: An image of a smectic A thin film, displaying the characteristic 'fanning' pattern associated with the mesophase. Viewed through crossed polarisers.

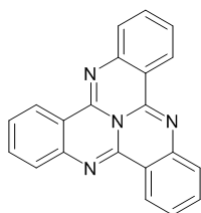


Figure 3.13: The structure of tricycloquinazoline.

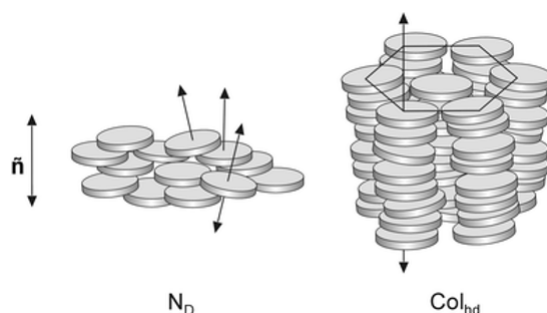


Figure 3.14: Schematic showing the structure of the nematic (N_D) and columnar (N_C) mesophases of the discotic mesogens.

Instead, a number of different DLC mesophases have been identified based on different possible stacking of discs, the main two of which are columnar and nematic DLCs. A schematic of their structures is shown in Figure 3.14.

3.1.4 Chiral nematic liquid crystals

As the name suggests, chiral nematic (N^*) LCs can rightly be considered as an extension of the nematic mesophase. The N^* mesophase arises in one of two conditions: if the mesogen is a chiral compound or if certain chiral compounds are incorporated into a nematic LC material as a dopant. The former of these shall be discussed first, as it was the first to be discovered.

Historically the terms ‘chiral nematic’ and ‘cholesteric’ have been used interchangeably, with the latter slowly falling out of favour as chiral nematic behaviour was observed in a wider and wider range of materials, chemically unrelated to the cholesterol derivatives that generated the name. Both terms are used in this work, but they are not to be considered interchangeable: ‘cholesteric’ is used to refer to N^* LCs that consist of a chiral mesogen or a mixture containing chiral mesogens as the source of chirality. In contrast, ‘chiral nematic’ refers to system which are based on the inclusion of a non-mesogenic chiral compound in an achiral nematic host. This allows us to distinguish between the two principles methods of creating

a N* LC.

Chirality Chirality is an optical property of certain molecules that can exist in mirror forms which are non-superimposable. Such forms are known as optical isomers of each other. Chirality is an exceptionally important concept with many differing impacts.

Optical isomerism has many possible sources. Most commonly, the inclusion of an asymmetric carbon centre, such as in the case of amino-acids, within a molecule results in the formation of a stereogenic centre. The mirror forms are identified as enantiomers, and can be distinguished by the direction in which they will rotate a plane of polarised light.

N*LC phases can be induced by other forms of optical isomers. For this work, the other form of optical isomerisation discussed is atropisomerisation, which refers to optical isomers that, while not inherently chiral, can be separated due to a significant rotational barrier around a single bond allowing for isomeric forms to be separated. This is mostly clearly seen in the case of R,R'-bis(2-naphthol), or BINOL.

Behaviour of N* LCs It is possible to argue that the N* mesophase was one of the first mesophases to be discovered, as it is present in the phase diagram of cholesterol myristate (Figure 3.2), the substance first investigated by Reinitzer in 1888 [Reinitzer (1888)]. It was not identified at this time as a distinct mesophase, however, as the bulk properties of a N* LC are very similar to those of a nematic LC, although Reinitzer did make note of the iridescent sheen that can be seen in N* LCs. If a N* LC is prepared as a thin film on an alignment layer however, a radically different structure is adopted. Due to the chirality of the LC molecule, the preferential alignment of molecules is not along a common director, but skewed slightly to accommodate the chiral nature of the molecule below. If the material

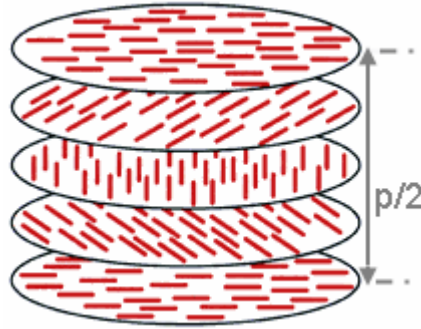


Figure 3.15: A schematic of the N* mesophase.

is chirally pure (e.g. if only one enantiomer is present), the net effect of this is that N* LCs self-assemble into a helical superstructure, with regularly repeating layers of common alignment, separated by a distance equal to a full twist of the helix, termed the helical pitch (p) (Figure 3.15).

As was introduced in Section 3.1.2, regularly repeated layers of molecules sharing an orientation can undergo Bragg reflection of a beam with wavelength equal to $2d\sin\theta$. In this case, the $2d$ in the previous equation is dependent on both the pitch and the mean refractive index (\bar{n}) of the LC. This can be expressed as in Equation 3.3:

$$\lambda = \bar{n}p \quad (3.3)$$

The mean refractive index in turn is defined in terms of the ordinary (n_o) and extraordinary (n_e) refractive indices of the LC (Equation 3.4).

$$\bar{n} = \frac{n_e + 2n_o}{3} \quad (3.4)$$

It is worth noting that due to dispersion, refractive index has a significant wavelength dependence which could affect systems where the wavelength of maximum reflection changes significantly. The extent of this dispersion can be recorded

in dispersion curves, which are known for many nematic hosts such as E7 [Tkachenko et al. (2006)]. In this work the impact of dispersion is ignored, but correcting for dispersion would be relatively simple given the existence of dispersion curves in the visible/near-IR range.

If the pitch of the N* LC is in the range of 350-600 nm, then the wavelength of the reflected beam will be in the visible region of the electromagnetic spectrum when viewed at the normal incidence to the film, and the films will adopt a brightly coloured hue due to the reflection of a narrow band of wavelengths, as determined by the birefringence (Δn) of the LC (Equation 3.6).

$$\Delta n = n_e - n_o \quad (3.5)$$

$$\Delta \lambda = \Delta n p \quad (3.6)$$

Given the angular dependence of the Bragg equation (Eq. 3.2), altering the viewing angle of the film from the normal will result in a change in the wavelength of maximum reflection (λ_{max}). This gives rise to an iridescence in the films when handled, which is characteristic of N* LCs. This iridescence can also make measurements complicated, due to the angular dependence of the values of p . Therefore, by convention only values recorded at normal incidence to the film are reported, a convention which is followed in this work.

As the helix has a given handedness, only light of a polarisation matching the handedness of the helix is reflected. This means that an (*R*)-helix will only reflect right-handed circularly polarised light, while an (*S*)-helix will only reflect left-handed circularly polarised light. This unique behaviour has been the focus of much of the work into N* LCs. As the helices in a N* LC have a given handedness dependent on the chirality of the LC or dopant used, this has the additional

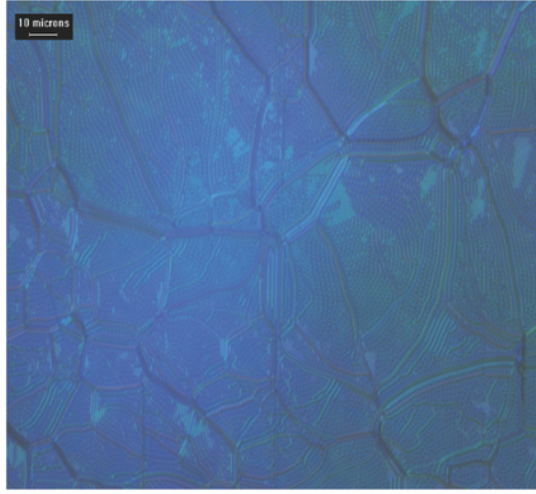


Figure 3.16: A polarised optical micrograph of an aligned chiral nematic thin film. Cachelin et al. (2016b).

impact of limiting the light reflected to that of a single circular polarisation. If illuminated with a combination of right- and left-handed circularly polarised light, a right-handed helix will reflect only right-handed circularly polarised light, while transmitting left-handed circularly polarised light.

This polarisation dependence allows for simple identification of the N^* mesophase by polarised optical microscopy. Under POM, thin films that align perpendicular to the alignment layer adopt a characteristic oil-slick texture, commonly referred to as the Grandjean texture (Figure 3.16).

As mentioned previously, a second method of creating a N^* mesophase is to incorporate a chiral molecule into a nematic LC host. The chiral molecule then acts on the nematic host to create the rotation in the director that gives rise to the N^* mesophase. The efficiency of the molecule in inducing a helix is termed the helical twisting power (β) and arises from the geometry of the dopant in question.

Additionally, the optical purity (as measured by the enantiomeric excess, e_e) and the doping concentration (by weight, c_w) have been shown to impact the pitch of the helix created. These are expressed in Equation 3.7.

$$p = (\beta c_w e_e)^{-1} \quad (3.7)$$

3.2 Polymer stabilised liquid crystals

One feature that limits the application of liquid crystals in some contexts is the fragility of the liquid crystalline films. As noted above, the lack of positional order means that liquid crystals behave in a fluid fashion, and as such can be easily mechanically damaged. Any such damage has the effect of disrupting the order that exists within the LC, reducing its functionality. This has led to the necessity of encapsulating the LC within a cell, typically made of a conductive surface such as indium tin oxide (ITO) coated glass. This has two negative side-effects for LC devices: it substantially increases the cost of devices, whilst ruling out applications such as flexible displays.

In order to counter these problems, LC are often stabilised with a polymeric host material, creating a Polymer Stabilised Liquid Crystal (PSLC). There exist several ways of inducing the formation of a PSLC. These should not be confused with polymeric liquid crystals, as defined in Section 3.1.4, where the mesogenic material is incorporated into the physical structure of the polymer. PSLCs instead consist of phase separated areas of polymer and liquid crystal.

3.2.1 Types of polymer stabilised liquid crystals

Polymer dispersed liquid crystals

The first, and most investigated is termed a polymer-dispersed liquid crystal (PDLC). PDLCs can come in two major morphologies, depending on the fabrication conditions and notably the LC content. The most desirable for electro-optical applications consists of regular small domains of liquid crystal dispersed within a

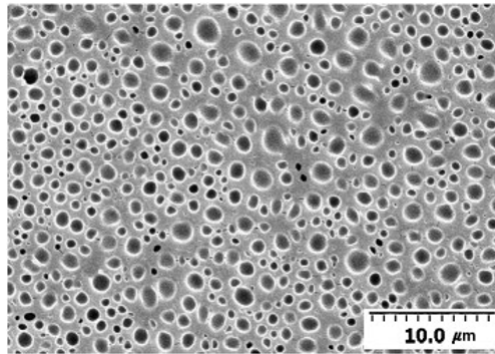


Figure 3.17: An SEM image showing bubbles of LC isolated within the polymer (grey background). Reproduced from [Yamagishi et al. (1989)].

polymer network, as can be seen from the scanning electron microscopy (SEM) image in Figure 3.17. This was termed the ‘Swiss Cheese’ morphology by Yamagishi [Yamagishi et al. (1989)]. The second consists of larger, irregular domains of LC, associated with higher concentrations of LC, and termed as the ‘polymer ball’ morphology.

For the former morphology, within the bubbles the LC director is determined by the polymeric walls of the droplet under normal conditions [Drzaic (1986)], resulting in random alignment of directors and films that strongly scatter light. When an electric field is applied, however, the directors align with the field, allowing the transmission of light (Figure 3.18). If the ordinary refractive index of the polymer and LC are similar, this can result in films that turn from strongly scattering to transparent when powered, which has been exploited to create light shutters. As the transition between the ON and OFF state is continuous, using variable voltages allows for the construction of light modulators [Bloisi and Vicari (2003)]. As might be expected, droplet size and morphology has a strong impact on the performance of the PDLC films, with smaller droplets having quicker relaxation times due to the greater influence of the polymeric walls of the droplet [Lackner et al. (1989)].

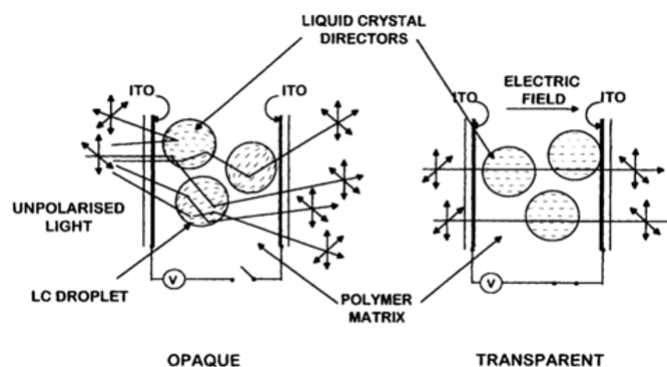


Figure 3.18: The difference in the alignment of the director in on and off states of PDLC visualised. Reproduced from [Bloisi and Vicari (2003)].

For the latter ‘polymer ball’ type PDLCs, due to the lesser impact of the polymer on the phase separated LC regions films exhibit strong memory effect, with the transparent state persisting long after the electric field is removed [Yamagishi et al. (1989); Chang et al. (1996)]. The film can be returned to the scattering state by the application of heat, allowing for thermally addressed displays [Yamaguchi et al. (1992)]. It has since been shown that processing methods have a substantial impact on the electro-optical properties of these PDLCs [Chang et al. (1996)]. The study of ‘polymer ball’ type PDLCs has been limited, although some attention has been paid towards their potential to act as switchable optical gratings [Fuh et al. (2002)].

Polymer network stabilised liquid crystals

Pioneering work on Polymer-Network Stabilised Liquid Crystals (PNS-LCs) was done by Broer in the years 1988-1991 [Broer et al. (1988, 1989b,a, 1991)]. These utilise multi-functional mesogenic reactive monomers at a low concentration (5-10 wt%) as well as an initiator (Figure 3.19) in combination with a liquid crystalline material.

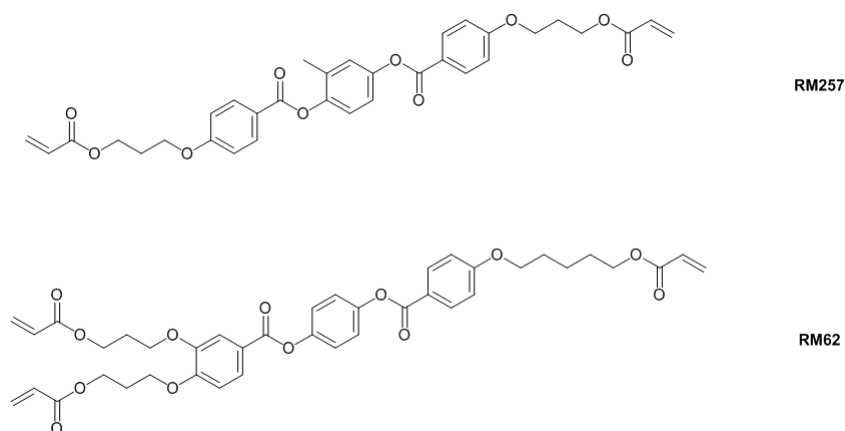


Figure 3.19: Reactive Mesogens 62 and 257, two examples of monomers for the creation of PNS-LCs.

Under illumination, the monomer reacts to form a polymeric network, which then stabilises the liquid crystalline matrix. The LC can be removed post-polymerisation to reveal the underlying polymer network structure. From this, the orientation of the polymer network has been shown to be determined by the director of the LC [Fung et al. (1995)].

This polymeric stabilisation has an effect on more than just the nematic properties of the LC. Samples containing a small percentage of polymer show birefringence well into the isotropic phase at which point such behaviour disappears for pure LC samples. The total birefringence can be expressed as the sum of the contributions from the LC (Δn_{LC}) and the polymer (Δn_p) (Equation 3.8).

$$\Delta n = \Delta n_{LC} + \Delta n_p \quad (3.8)$$

As the contribution from the polymer can be measured to be small (typically on the order of 0.001) the birefringence observed in the isotropic phase must result from residual order within the LC, possibly due to the polymer network acting as a template. This behaviour is seemingly confirmed by a decrease in the

enthalpy associated with the nematic-isotropic transition on increasing polymer concentration [Hikmet (1991)]. which again can be explained in terms of the polymer network encouraging some nematic-like ordering within the isotropic phase. This behaviour has also been confirmed for polymer networks in the SmA phase [Hikmet and Howard (1993)].

A large area of focus in PNS-LCs has been on so-called Polymer Stabilised Cholesteric Textures (PSCTs). First developed by Hikmet at Philips [Hikmet and Zwerver (1991)]. PSCTs consist of a combination of a polymer network and a N* LC. This was an expansion of the work undertaken earlier by Broer and Heynderickx [Broer and Heynderickx (1990); Heynderickx and Broer (1991)]. PSCTs were developed as optical shutters that have the advantage of being able to preserve polarisation information. It is worth noting that PSCTs utilise N* LCs with large pitches (typically several micrometers) that do not reflect optical wavelengths. Further details can be found in Dierking's excellent review paper [Dierking (2000)].

Hydrogen-bonded PNS-LCs An important subcategory within PNS-LCs is those incorporating hydrogen bonds. These come as a natural extension of the importance of hydrogen bonding in liquid crystalline mesophases.

The role of hydrogen-bonding in the formation of mesophases was first studied by Gray *et al.* in 1955. They found that certain non-mesogenic phenylic carboxylic acid derivatives could form a mesophase through dimerisation, which generated sufficient rigidity to allow for nematic and smectic mesophases to develop (Figure 3.20) [Gray *et al.* (1955); Gray (1962)]. Much of the work on these early monomeric hydrogen-bonded mesogens is covered in an excellent review by Paleos and Tsiourvas (1995).

This area of study developed by looking at the interactions between a polymer

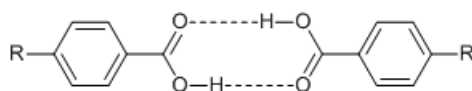


Figure 3.20: Schematic showing the (dashed) hydrogen bonds stabilising a phenylic carboxylic acid dimer.

capable of hydrogen bonding and a small molecule mesogen. Kato and Frechet found that combining a phenolic acid functionalised polyacrylate polymer with a mesogen containing a hydrogen-bond accepting moiety (a pyridyl group) resulted in significant stabilisation of the nematic phase associated with the mesogen [Kato and Frechet (1989)].

3.3 Liquid crystal sensors

The ability of liquid crystals to respond to a variety of stimuli is well known, notably in the now-ubiquitous liquid crystalline display. Alongside display applications liquid crystals have found use as actuators [van Oosten et al. (2007, 2009); Thomsen et al. (2001)], as well as a variety of photonic applications including tuneable filters [Gunning and Pasko (1981); Wu (1989); Hardeberg et al. (2002)], waveguides [Channin (1973); Larsen et al. (2003)], spatial light modulators [Konforti et al. (1988)] and lasers [Kopp et al. (2003)]. (See review by Beeckman *et al.* [Beeckman et al. (2011)].)

The weak forces involved in the liquid crystalline mesophases make them ideal materials to study for sensing applications, as it does not require a large stimulus to change the order parameter of a nematic LC or the pitch of a chiral nematic LC, for example. As such, development of liquid crystalline sensors is an increasing field, with many varied sensing mechanisms being tested. A substantial amount of these applications, summarized in Pasechnik *et al.* in *Liquid Crystals: Viscous and Elastic Properties* [Pasechnik et al. (2009)], are based on

the detection of mechanically-induced perturbations of a liquid crystal. In this work, we will instead focus on the sensing of chemically-induced perturbations, either directly through a reaction with a chemical analyte, or indirectly through a secondary interaction causing a chemical response within the LC matrix, later focussing specifically on those that induce a change in the reflection band of the chiral nematic mesophase. This is still a significant body of work, covering a wide range of sensing mechanisms.

In a recent review, [Carlton et al. (2013)] divide these sensing mechanisms broadly into two categories: those that utilise ‘interfacial phenomena’ in order to induce macroscopic change in the properties of liquid crystalline films, and those that operate by directly changing a property of the bulk LC material. This is a useful distinction as it highlights a central difference in methods of interacting with an analyte. Among the former we can create two classes based on at which interface the recognition event originates. If it is the alignment layer, then such devices are termed command surfaces. Such devices are discussed in Section 3.3.1. For devices that feature an aqueous-LC interface, it is possible to change the alignment of the LC by inducing a change at this interface. These are discussed separately in Section 3.3.1.

Sensors that involve a change in the bulk properties of the LC have been dominated by N*LCs. Within this category, two different sensing mechanisms have been identified. The first of these is swelling of the nematic host in order to increase the pitch of the N*LC helix, either by thermal expansion or the absorption of a solvent. The second sensing mechanism is to include a reactive group as either a mesogenic component or a chiral dopant within a N*LC. Both of these mechanisms are studied in detail in Section 3.3.2.

3.3.1 Interfacial change driven sensors

Command surfaces

These sensors operate on the basis of a change at an interface, normally the alignment layer used to create a common director for the LC, can drastically alter the alignment of the LC. This change in alignment can then be monitored by viewing the sample through crossed polarisers, where a movement from planar to homeotropic alignment, for example, is accompanied by a change from bright to dark of the LC cell. This method has several desirable features for sensing applications:

- It includes a built-in signal amplification;
- Response times are typically low compared to devices involving a change to a responsive component in a LC mixture;
- Monitoring the device output is relatively facile, and does not require significant computation.

Early work by [Ichimura et al. (1988)] was based on the UV-initiated cis-trans isomerisation of azobenenes resulting in a change in the alignment of the LC, as illustrated in Figure 3.21. They coined the term ‘command surface’ to describe these materials, which was picked up by Knobloch *et al.* in their development of optical information storage based on a similar principle [Knobloch et al. (1995)].

This method of altering the surface of the alignment layer in order to change the alignment of the properties has since been extended, notably by [Shah and Abbott (2001)], to include chemical analytes. These rely on competitive binding of LC moieties and analytes to receptors bound to a microstructured surface that acts as the alignment layer for the LC. (Figure 3.22)

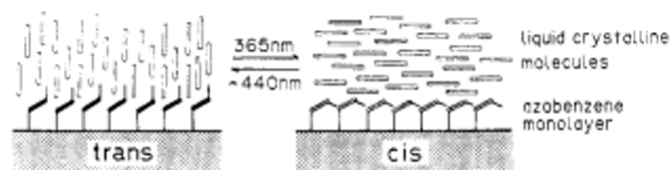


Figure 3.21: Schematic showing the impact of cis-trans isomerisation on the alignment of the liquid crystal molecules above it [Ichimura et al. (1988)].

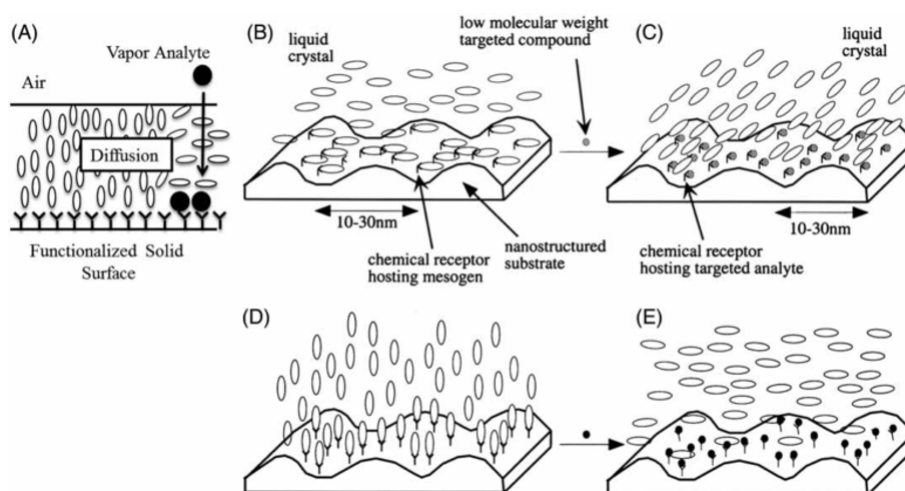


Figure 3.22: Schematic indicating functional surface-based sensing of chemical analytes. Reproduced from [Shah and Abbott (2003)].

This principle has since been extended to a wide range of chemical analytes, including organophosphorus compounds [Cadwell et al. (2007); Adgate et al. (2009)], aldehydes [Bi and Yang (2008)], organoamines [Shah and Abbott (2003)] and glucose [Zhong and Jang (2014)]. Recent advances have extended the sensing to that of larger biomolecular structures, including DNA and viruses [Han et al. (2014)], where the advantages of label-free detection are strongly felt.

LC-aqueous interface sensors

A second, smaller group of interfacial sensors are based on the changes in the orientation of an LC film triggered not at the alignment layer surface, but instead

the open LC-medium surface [Tan et al. (2014); Bi et al. (2009)]. In this second detection mechanism, the ability of molecules, especially amphiphiles, to self-assemble at the interface between thermotropic LCs and aqueous solutions allows for a change in the orientation of the LC [Lockwood et al. (2008)]. This has some advantages over detection at the solid interface: greater mobility in the interface allows for the formation of domains and features not normally observed at the LC-solid interface, as well as lowering the diffusion time for molecules into the LC matrix [Zhong and Jang (2014)]. However, it does limit the range of molecules that can potentially be detected to those that preferentially occupy the interfacial zone.

One significant downside to these interfacially driven sensors is the reliance on polarised light to view the samples. As well as adding to the complexity of the sensors, these can add significant problems in terms of limiting diffusion through a sample. Another is the reliance on either functionalised surfaces, which can be expensive if certain biomolecules are required to be isolated, or on molecules that preferentially locate at the interface between a LC and an aqueous solution.

3.3.2 Bulk property change driven sensors

In the quest for producing sensors that provide a simple optical output, much attention has been paid to chiral nematic LCs. Due to the ability of chiral nematic liquid crystalline thin films to reflect a narrow range of wavelengths of visible light, as outlined in Section 3.1.4, they are ideal candidate materials for visually assayable sensors, something that is desirable for the creation of sensors that can be used in a wide variety of contexts, without the need for access to traditional analytical facilities.

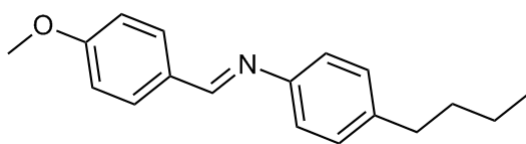


Figure 3.23: The chemical structure of N-(4-Methoxybenzylidene)-4-butylaniline (MBBA).

Nematic liquid crystals as sensors of chirality

One growing field is that of the detection and amplification of chirality. Many techniques have been used to attempt to investigate this field, including helically structured polymers [Yashima et al. (2004)], macromolecular aggregates [Palmans and Meijer (2007)] and functional surfaces [Fasel et al. (2006)].

As noted in Section 3.1.4, incorporating a chiral dopant within a nematic LC can induce a N^* phase, provided the chiral host has sufficient concentration and enantiomeric purity. The pitch of a helix that is generated is given in Equation 3.7.

This property can be exploited to create sensors by monitoring the pitch generated when a chiral substance is introduced. This was exploited by Bertocchi *et al.* to create a cheap and effective heroin sensor [Bertocchi et al. (1984)]. As biologically produced heroin is enantiomerically pure, on introduction to the LC MBBA (Figure 3.23) the host undergoes a phase transition to the N^* mesophase. Bertocchi *et al.* found that using this technique they were able to quantify the amount of heroin present at 100 ppm concentrations, which was comparable to contemporary gas chromatography detection limits.

Sensors based on the swelling of a N^* LC

Ferguson noted early on the potential for chiral nematic LCs to act as sensors [Ferguson (1964); Ferguson et al. (1966)]. He described two behaviours of cholesterol

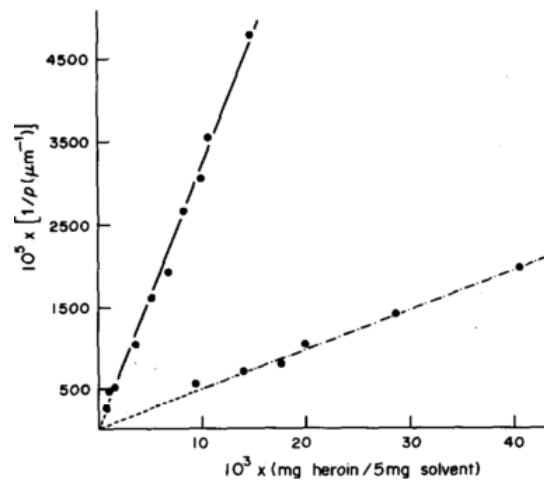


Figure 3.24: A plot of the inverse pitch against the concentration of heroin for LCs MBBA (solid line) and PCH (dashed line) [Bertocchi et al. (1984)].

derivatives. The first was a change in the wavelength at which maximum scattering was observed in response to changes in temperature for both pure materials and blends of mesogens (Figure 3.25).

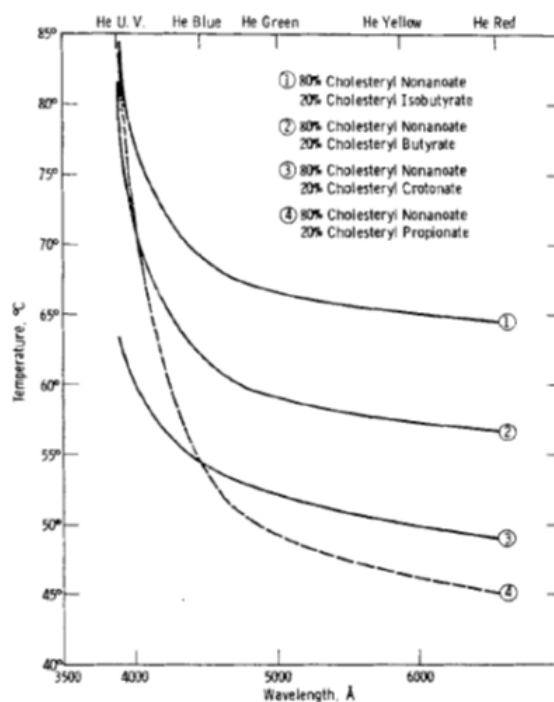


Figure 3.25: The change in the wavelength of the scattering maximum as a function of temperatures for blends of cholesterol derivatives [Ferguson et al. (1966)].

The second observation was exposing films of cholesteric LCs to solvents induced a change in the colour of the film, with different solvents producing different colour changes depending on the cholesterol derivative used. This is due to the absorption of the solvent within the nematic matrix, where it causes swelling which, in turn, increases the pitch of the helix. This property of N*LCs is particularly attractive for the sensing of low-mass organic compounds with few functional groups, which are traditionally difficult to monitor due to the limited interaction with devices [Mujahid et al. (2010)].

The second property has been the basis of a number of sensors, aimed at detecting and identifying volatile organic compounds (VOCs). Early work by [Toliver et al. (1970)] built on their initial reports to attempt to quantify the amount of VOC present in a sample. Another early work used the solvent-induced nematic-

isotropic transition of MBBA in order to quantify the amount of (non-specific) solvent present down to the ppm level [Poziomek et al. (1974)]. These and other early works suffered significantly from the problem of cross-sensitivity: as the mechanism of the change in pitch is simply absorption of solvent into the liquid crystalline matrix, multiple analytes can create a similar response. Dickert *et al.* attempted to address this problem by analysing the response to different solvent concentrations at multiple wavelengths [Dickert et al. (1994)]. They found that chloroform (CHCl_3) vapour caused a substantial reaction in the films, although methanol and tetrahydrofuran gave similar responses. This suggested that functionality was less important than molecular mass in creating responsive sensors. Winterbottom *et al.* expanded on this, looking at the effects of different solvents on films composed of varying mixtures of cholesterol derivatives [Winterbottom et al. (2003)]. In this latter case-study the effect of mass was not as pronounced, with benzene ($M_w = 78.11 \text{ gmol}^{-1}$) and hexane ($M_w = 86.18 \text{ gmol}^{-1}$) resulting in an isotropic phase transition while pyridine ($M_w = 79.10 \text{ gmol}^{-1}$) caused only a small change in the wavelength associated with maximum scattering. This suggested that there were effects beyond those purely associated with the molecular mass of the dopant. Mujahid et al. (2010) further developed this, looking at the change in absorbance at a fixed wavelength when the concentration of a solvent was changed. By plotting the percentage change in the absorbance at the wavelength of maximum reflection (λ_{max}) when exposed to 0.1% concentrations of solvent vapours they found a linear relationship between the molecular mass of the analyte and the response of the sensor (Figure 3.26).

In order to quantify the concentration of the analyte within the LC matrix a second series of experiments, where the active LC layer was placed on a quartz crystal microbalance (QCMB) were carried out. Mujahid found that when the mass of the analyte is accounted for, the linear relationship between the sensor

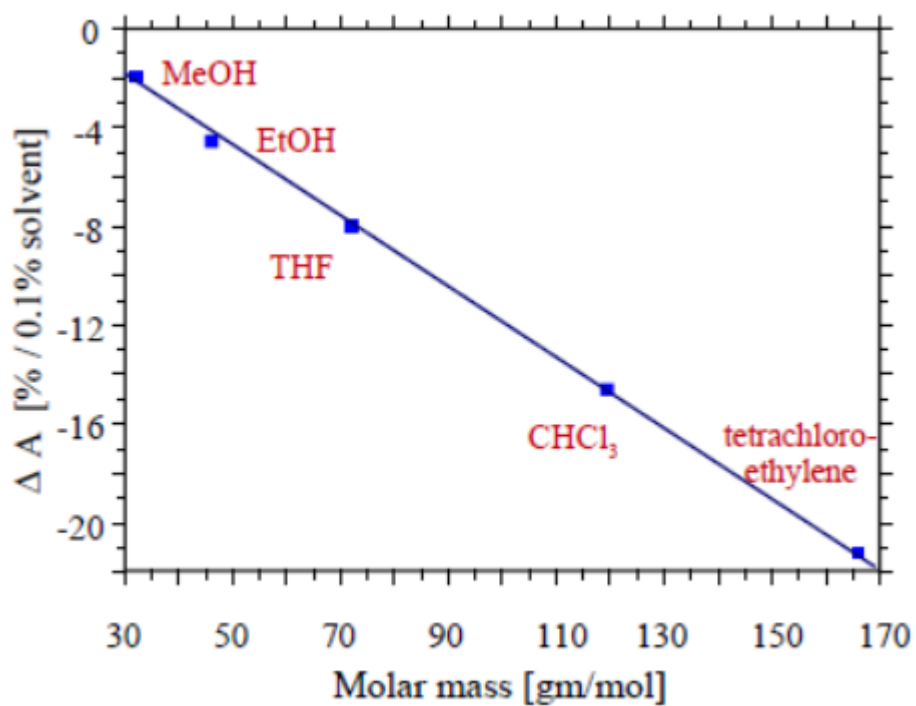


Figure 3.26: The percentage change in absorbance at λ_{max} when exposed to 0.1 wt% solvent vapour plotted against the molecular mass of the solvent [Mujahid et al. (2010)].

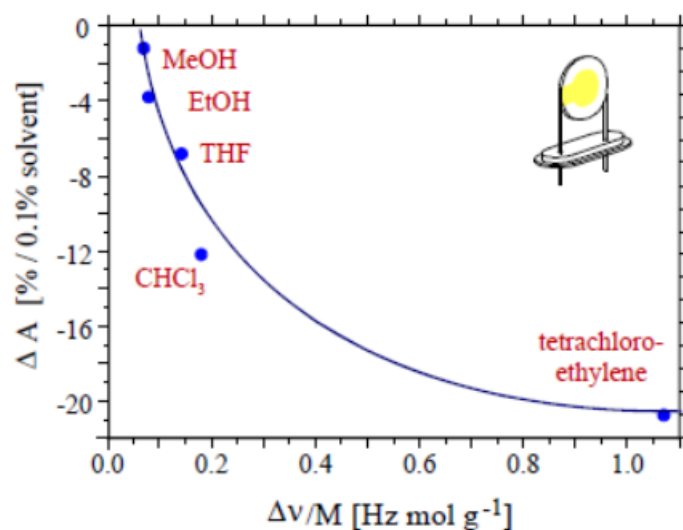


Figure 3.27: The percentage change in absorbance at λ_{max} when exposed to 0.1 wt% solvent vapour plotted against the mass-normalised sensor response [Mujahid et al. (2010)].

response and the molecular mass no longer holds true (Figure 3.27)

A later work by Chang et al. (2011) studied the difference in colour change associated with acetone and toluene, focussing on the difference in polarisation and diffusion constant between the two vapours. They created the approximation in Equation 3.9 where $\Delta\lambda$ is the variation in the reflection maximum, λ_∞ is the reflection maximum at the highest concentration of solvent vapour, before the film becomes isotropic. D is the diffusion coefficient and L is the thickness of the film.

$$\frac{\Delta\lambda}{\lambda_\infty} = \sqrt{t \frac{16D}{\pi L^2}} \quad (3.9)$$

From this equation, the diffusion coefficient for a given solvent can be found, and therefore the time to saturation found. They found that toluene created substantially greater shifts in the reflection maximum, but the higher diffusion coefficient associated with acetone ($0.096 \mu\text{m}^2\text{s}^{-1}$, vs $0.017 \mu\text{m}^2\text{s}^{-1}$ for toluene) meant

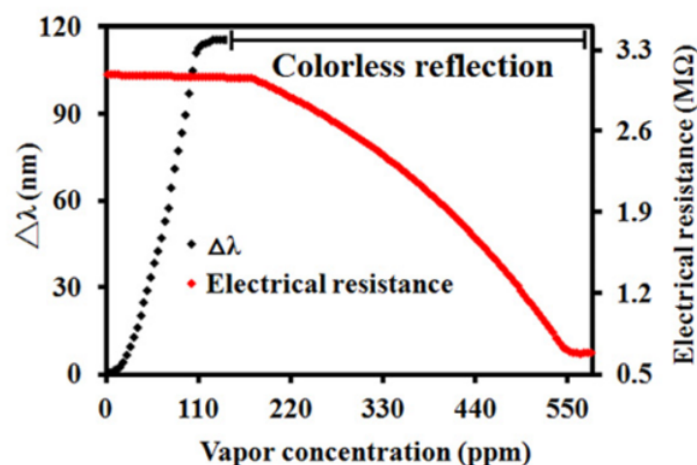


Figure 3.28: A plot showing the change in both the wavelength of the reflection band ($\Delta\lambda$) and the electrical resistance of a hybrid N*LC-CNT film as the concentration of acetone vapour changes. [Chang et al. (2012b)].

it reached saturation much faster. This they attributed to the greater polarity of acetone giving it a higher affinity to E7, the nematic host. They also tested the reversibility of this process, and found that while spectral imaging showed little evidence of hysteresis, POM showed substantial disruption, which was disrupted alignment when the film entered the isotropic phase.

The high diffusion coefficient associated with acetone combined with the low concentrations required to induce an isotropic state within the N*LC (typically < 200 ppm) leads to sensors with a low dynamic range. In order to increase this, Chang *et al.* proposed a hybrid structure, consisting of a nematic host which contained both a chiral dopant and carbon nanotubes (CNTs)[Chang et al. (2012b)]. The sensor was based on the CNTs exhibiting increased conductivity caused by reorganisation as the N*LC transitions from a Grandjean texture to a multidomain texture. It was theorised that this process would allow for the formation of CNT networks, which would lower the overall resistivity of the film. This was confirmed experimentally (Figure 3.28).

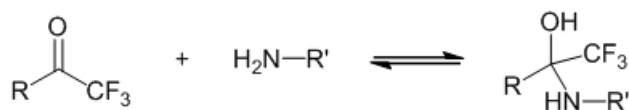


Figure 3.29: The reaction between a trifluoroacetate and a primary amine.

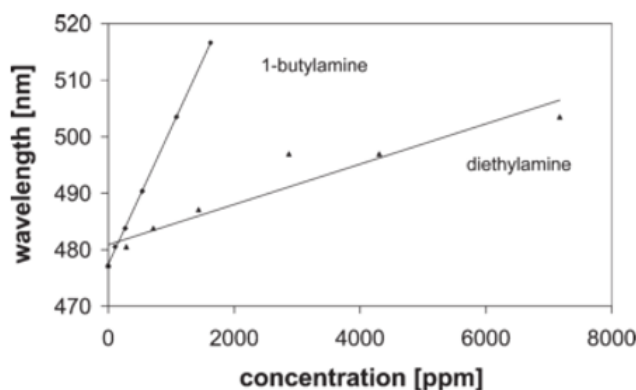


Figure 3.30: The response of a sensor containing a trifluoroacetyl functionalised cholesterol derivative to 1-butylamine and diethylamine vapours [Kirchner et al. (2006)].

Kirchner et al. (2006) attempted to create a PSLC that was capable of discriminating between primary amine derivatives. This was done by the creation of a cholesterol derivative functionalised with a trifluoroacetyl moiety, which shows well-known selectivity towards amines and has previously been used in amine sensors (Figure 3.29) [Mertz et al. (2003)].

They found that on exposure to primary amine 1-butylamine and secondary amine diethylamine the sensor exhibited concentration-dependent changes in reflection band, with changes of 40 nm shown for 1-butylamine and a smaller change of 25 nm for diethylamine. (Figure 3.30). Triethylamine also gave a response (6nm). Surprisingly, no change in the reflection band was reported for high concentrations of acetone, methanol and ethyl acetate.

Another amine sensor developed by Sutarlie et al. (2010) exploited the ability of cholesterol derivatives to form hydrogen bonds. When exposed to vapours of

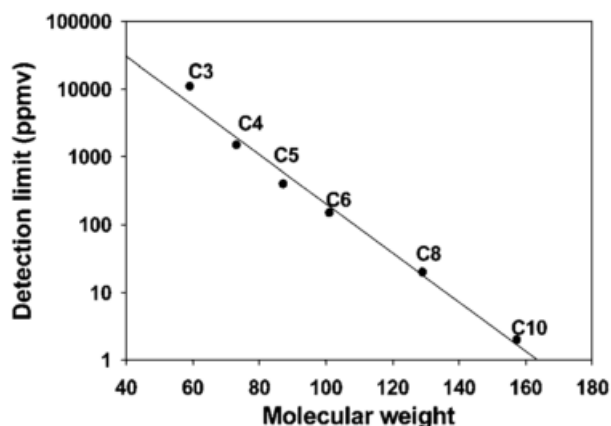


Figure 3.31: A graph showing the linear relationship between detection limits and molecular mass (units gmol^{-1} of primary amine sensors [Sutarlie et al. (2010)]. Chain lengths are marked as C3-C10.

hexylamine and octylamine, PSN*LCs formed by photopolymerisation of various cholesterol derivatives and a photopolymerisable monomer showed a reversible change in reflection band when exposed to primary amine vapours, with no change observed for other VOCs such as heptane or secondary amines such as diisopropylamine. This was attributed to the primary amines being able to insert themselves into the hydrogen bonds formed within the mesogens, resulting in a blueshift in the reflection band. This was confirmed by exposure to non-amine hydrogen bond donors pentanol and hexanol. The detection limits found directly correlated with the molecular weight of the dopant (Figure 3.31).

Hydrogen-bonded PNS-N*LCs as sensors: One important subcategory within PNS-N*LCs is those that contain hydrogen-bonding as a secondary stabilisation mechanism. Hydrogen bonding was also at the centre of recent work by Herzer et al. (2012). By incorporating hydrogen bonding triggers within a PNS-N*LC, they created a film that, once converted into a salt film by treatment with KOH, showed a colorimetric response to different levels of relative humidity. This was attributed to the swelling associated with water entering the hygroscopic salt film.

One benefit was the highly reversible nature of these changes: films exposed to different relative humidities displayed rapid (<2 min.) reversible changes in colour. By varying the temperature, it was shown that the rate of reversibility depending primarily on the rate of water evaporation, with samples maintained below the freezing point of water showing no noticeable change in reflection band over the time monitored. This means that, provided the films are not subsequently exposed to water, they can also act as time-temperature integrators for monitoring goods that need to be maintained below 0 °C.

A similar hydrogen-bonded PNS-N*LC was used by Chang et al. (2012a) in the discrimination of primary alcohols. In this case a non-polymerisable mesogen, 5CB, was included in the initial mixture, and later extracted in order to generate a porous network. This nanoporous structure had previously been demonstrated for smectic LCs, where it was shown that the inclusion of ions changed the order of the PNS-LC [Gonzalez et al. (2008)]. Such porosity is beneficial for sensors as it allows for higher loading of the analyte in question. Chang found that it was possible to not only discriminate between ethanol and methanol using this method, but also to accurately quantify binary mixtures of the two. This was attributed to the difference in molecular affinity of methanol and ethanol towards the hydrogen-bonded PNS-N*LC, as opposed to any effect due to the size of the molecule involved. It was also found that by tuning the composition of the N*LC mixture it was possible to target different compositions of the water/methanol/ethanol mixtures. This and other similar applications of hydrogen-bonded PNS-N*LCs are covered in a excellent recent review by Broer et al. (2012).

Recently, Stumpel et al. (2015) made use of inter-penetrating polymer networks (IPNs) in order to create a responsive LC network-polymer hydrogel film. IPNs consist of an inter-penetrating mixture of two different polymers, including a responsive hydrogel and a second, mechanically stabilising polymer. As

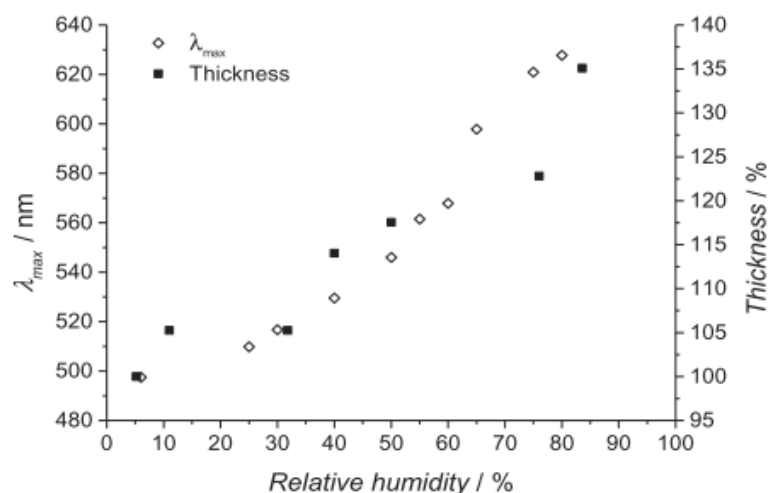


Figure 3.32: Graph showing the change in reflection maximum (λ_{max}) and thickness in response to changes in relative humidity. Stumpel et al. (2015)

hydrogels tend to respond to changes in humidity and pH by changing volume, incorporating a PSN*LC as the second polymer element allows for visual measurement of this swelling. Stumpel *et al.* found that both the reflection maximum and thickness of the IPN film showed a linear response to changes in relative humidity (Figure 3.32). IPNs combined with functional polymers show distinct promise in creating a new type of responsive surface.

Temperature monitoring using chiral nematic liquid crystals

The first sensing application for chiral nematic LCs was as thermometers [Ireland and Jones (1987)]. As noted previously (in Section 3.1.4) the pitch of a N* LC is temperature dependent, and heating a sample will result in a red-shift due to the thermal expansion of the LC matrix. This effect is relatively small, with it taking a significant temperature change to induce a colour change [Sage (2011)]. This is undesirable for high-accuracy thermometer requirements, where larger changes over smaller temperature ranges are generally required. Therefore, LC thermometers instead make use of phase changes in order to rapidly change

colour in response to a change in temperature. The phase change that is commonly exploited is between the smectic A (S_A) and N^* phases. As the N^* phase approaches the transition, the pitch lengthens, resulting in a red-shift of the reflection band. This behaviour is due to a competition between the S_A phase preferring a layered structure, and the helical morphology preferred by N^* materials [Bauman et al. (2002)].

As well as direct thermometer applications, the thermal sensitivity of the N^* LC phase has been exploited in other applications. One such application is the creation of patterned isotropic domains within a PNS- N^* LC by Sousa et al. (2006). By applying a photomask to a polymerisable RM mixture, they were able to selectively polymerise areas within either the isotropic or chiral nematic phase, depending on the temperature of the mixture. Due to differences in the thermal expansion of the isotropic and N^* domains within the PNS-LC, on heating the patterned area would experience different amounts of expansion, allowing for the creation of thermally responsive topologies.

A later temperature-sensitive application of N^* LCs was the creation of a thermally-controlled reflective display by Hu et al. (2009). This device consisted of a mixture of cholesteric and nematic LCs with a hydrogen-bonded chiral dopant complex. Unusually, the device exhibited a blue shift upon heating, which was attributed to the rupturing of the hydrogen-bonded chiral dopant complex, resulting in a significant change in β (Figure 3.33). The display was not bistable, meaning the removal of the heat would result in a change of λ_{max} back to that of the room temperature value. Nematic equivalents of bistable displays have been known since the early 1990s [Kreuzer et al. (1993)], but their chiral nematic equivalent is highly desirable for the ability to produce vividly coloured passive displays.

Another recent application of N^* LCs was based on the use of mechanical embossing to create an optical time-temperature integrator [Davies et al. (2013)].

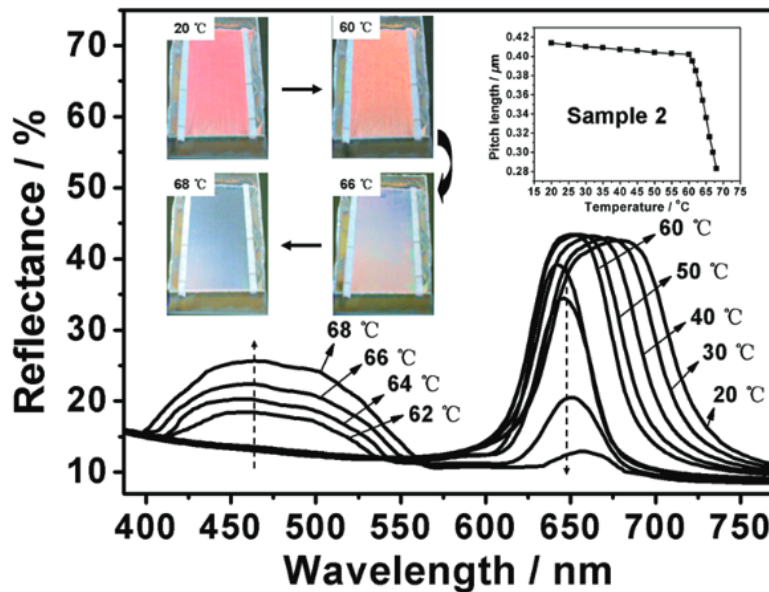


Figure 3.33: The thermally controlled display developed by Hu et al. (2009). The inset shows images of the sample described by the inset graph, labelled Sample 2.

By compressing a PNS-N*LC above the glass transition temperature of the polymer and then cooling it while under compression, Davies *et al.* were able to create patches of PNS-N*LC that had a smaller pitch than the surrounding uncompressed material. On heating above the glass transition temperature, the embossed portion would revert to the pitch of the surrounding material (Figure 3.34). This allows for a passive record of temperature, depending on the glass transition temperature of the polymeric material. This has strong applications in the shipment of temperature controlled substances such as medications or cell samples.

From these later descriptions of temperature sensitivity in LC-based materials it is clear to see that their capabilities go beyond simply monitoring ambient temperature, and indeed beyond simple sensing applications.

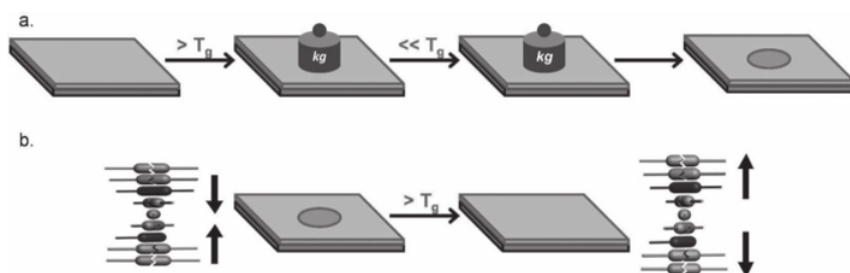


Figure 3.34: An illustration of a) the embossing process and b) the relaxation of the pitch above the glass transition temperature [Davies et al. (2013)].

Sensors incorporating responsive moieties

Another approach is to include a responsive moiety, either mesogenic or as a chiral dopant, within the N*LC. This was first undertaken by Shinkai et al. (1990). They had previously developed a crown-ether functionalised cholesterol derivative in order to study selective ion transport (Figure 3.35) [Shinkai et al. (1989)]. In the later work, they studied the impact of incorporating this into a blend of mesogenic cholesterol blends.

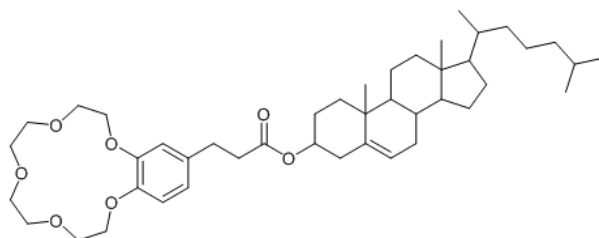


Figure 3.35: A crown-ether functionalised cholesterol derivative [Shinkai et al. (1990)].

They found that when exposed to alkali metal salts, the change in the pitch varied with both the identity of the metal and the counter-ion. The changes as a result of the anion were attributed to the size of the anion, mirroring the swelling effects mentioned previously (Table 3.1).

In the case of the metal ions, this relationship did not hold, with K^+ inducing

Ion	Ionic Radius (nm)	λ_{max} (nm)
Cl ⁻	0.184	474
SCN ⁻	0.209	487
ClO ₄ ⁻	0.225	507
TCIBP ⁻	0.682	537

Table 3.1: Ionic radii and wavelengths of maximum reflection for N*LC films containing crown-ether functionalised cholesterol derivatives when exposed to various anions.

a substantially larger change than Cs⁺, despite being significantly smaller (Figure 3.36). Although this effect was not explained, the fact that changing the crown-ether moiety from 15-crown-5 to 18-crown-6 resulted in a significantly lower λ_R value for K⁺, Li⁺ and Na⁺, while that of Cs⁺ increased, suggests that the strength of the interaction between the crown-ether moiety and the metal cation is responsible for the change in reflection, as opposed to the change being entirely attributable to swelling.

Later work built on this by utilising a second effect of chirally functionalised crown-ethers: their ability to discriminate between enantiomers of ammonium compounds [Kyba et al. (1973)]. Nishi et al. (1991) utilised the previously described crown-ether functionalised cholesterol derivatives in order to measure the difference in pitch when cholesteric blends were exposed to a variety of optically pure ammonium salts. They found that *D*-isomers usually induced significant increases in pitch, while *L*-isomers induced smaller decreases in pitch. When the cholesterol moiety on the reactive dopant was replaced with a non-chiral alternative, most of the chiral analytes caused no change in the pitch, while others caused very small changes ($\Delta\lambda < 10$ nm). This confirmed that a reaction of an analyte with a chiral dopant within a LC matrix could induce a change in the pitch. This work was later expanded on to include boronic acid functionalised cholesterol derivatives as sensors for sacchirides [James et al. (1993)], where again good

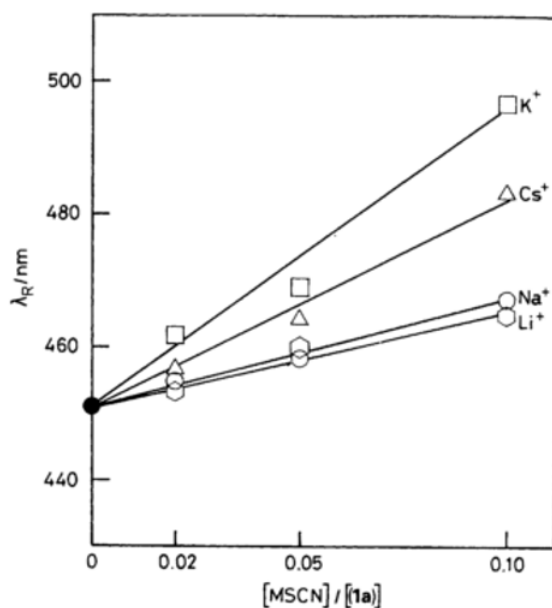


Figure 3.36: A plot of reflection maxima (λ_R) against metal thiocyanate concentration for a variety of alkali metals [Shinkai et al. (1990)].

resolution between enantiomers was found.

If the reaction between the analyte and the dopant is irreversible, then the potential exists to create chemical dosimeters. These would allow for optical identification of the total dose of a given analyte over a specified timeframe, as opposed to real time sensors which can only monitor the concentration of an analyte at a given moment. This is the principle behind the humidity sensor created by Saha *et al.* [Saha et al. (2012a)], although the dosimetric nature of the sensor was not examined in detail. This sensor was based on the creation of a *R*-(+)-1-binaphthol (BINOL) dimer (Figure 3.37), which was expected to have a significantly higher helical twisting power than the monomeric unit, which has been measured to have a low value of β in nematic hosts such as E7 [Gottarelli et al. (1986)]. This expectation was based on previous work showing an increase in helical twisting power of bridged biaryls compared to their open-chain counterparts [Gottarelli et al. (1983)]. This increase is attributed by Eelkema and Feringa as due to a

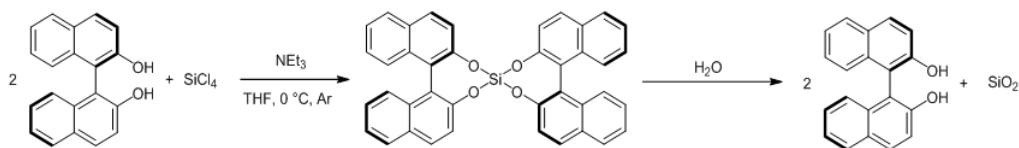


Figure 3.37: Reaction scheme for the formation of a BINOL dimer that is sensitive to water vapour [Saha et al. (2012a)].

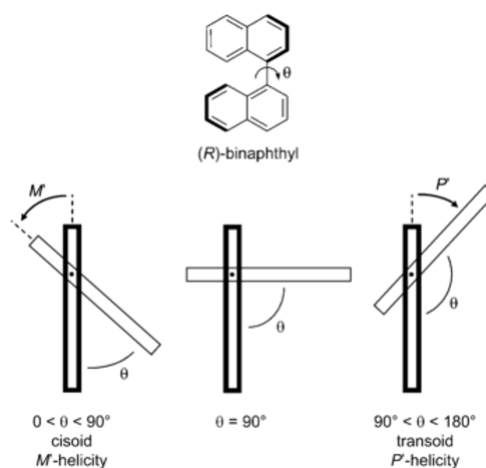


Figure 3.38: Illustration of the transoid and cisoid BINOL forms, which are dependent on the dihedral angle θ . [Eelkema and Feringa (2006)].

change in the dihedral angle formed between the two naphthyl units [Eelkema and Feringa (2006)]. The ability of BINOL derivatives to move from transoid to cisoid forms (see Figure 3.38), depending on the groups present on the 1-naphthyl site has also been identified as the reason why BINOL derivatives of either chirality can form both right and left handed helices [Gottarelli et al. (1983); Eelkema and Feringa (2006)].

When exposed to water vapour, the BINOL dimer undergoes an irreversible reaction which returns it to the monomeric state, which due to the lowered value of β and solubility in the nematic host resulted in a notable increase in the wavelength of the reflection maximum (Figure 3.39).

A similar dopant-analyte interaction was the basis of a barbiturate sensor de-

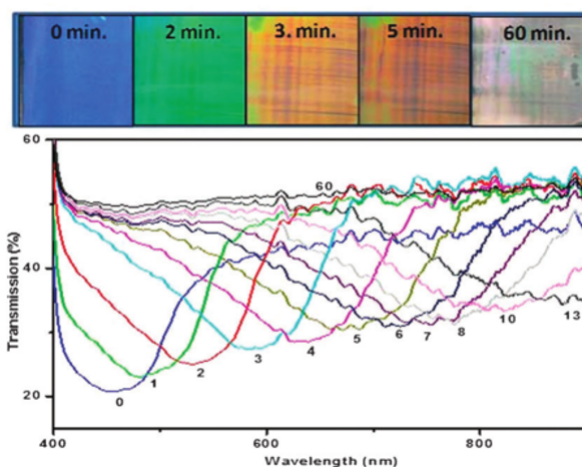


Figure 3.39: The change in wavelength of the reflection maximum as observed as a function of time exposed to air of 75% relative humidity. [Saha et al. (2012b)]

veloped by Carlisle-Chambers *et al.* [Carlisle Chambers et al. (2007)]. This sensor used a mesogen functionalised receptor that formed six hydrogen bonds with the barbiturate analyte, allowing for selective binding, within a cholesteric host. Upon reaction with the analyte, a change in reflection band was observed. This was attributed to a conformational change in the dopant-analyte complex, although no mechanism for the change in reflection band is given.

Work by Han et al. (2010b) extended on this premise by the creation of a complex between an achiral reactive component of the N*LC mix and a chiral auxiliary. This technique was pioneered by Eelkema and Feringa (2005) in early attempts to amplify the helical twisting power of the dopants. This technique circumvents a central problem that sensors based on reactive chiral dopants have to face: finding molecules that are both reactive and have a sufficiently high helical twisting power to induce a N* helix that reflects within the visible spectrum. By combining a reactive material with a chiral auxiliary known to have a high helical twisting power a wider range of reactive dopants are accessible.

In this work, the reactive molecule chosen was 1,2-diphenylhydrazine, which

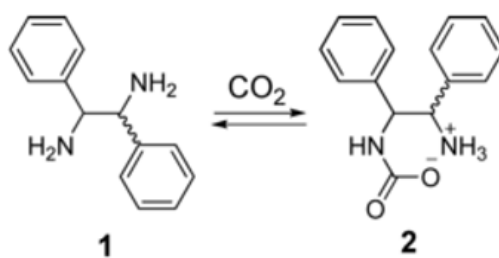


Figure 3.40: The reaction between 1,2-diphenylhydrazine and CO₂, as used by Han et al. (2010b).

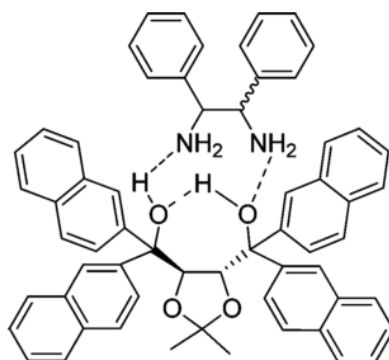


Figure 3.41: The complex between TADDOL and 1,2-diphenylhydrazine that formed the responsive component of the CO₂ sensor developed by Han et al. (2010b).

exhibits well-known reactivity towards CO₂ (Figure 3.40). $\alpha,\alpha,\alpha',\alpha'$ -tetraaryl-2,2-disubstituted-1,3-dioxolane-4,5-dimethanol (TADDOL) was chosen as the complex partner, due to its exceptionally high helical twisting power (Figure 3.41). On exposure to the analyte, the sensor displayed a visible change in colour, with lower concentrations requiring longer exposure times to reach full conversion, and concentrations below 25% never reaching full conversion.

3.4 Conclusion

We have seen that N* LC thin films containing responsive dopants have previously been investigated, and confer some advantages over other LC-sensor systems. As with any sensing platform, it is necessary to choose applications which mirror the strengths of the technology, rather than just competing to obtain the highest sensitivity or lowest detection limits. From the properties delineated above, we can draw some broad conclusions about circumstances under which N* LC thin films containing responsive dopants would be a suitable sensing platform:

- The requirement for significant exposure times, as well as the ability to measure time-integrated exposure levels, lends itself well to applications where the total exposure to a given analyte over time is important. As such, dosimetric applications are more suitable than applications which require rapid response times.
- The low material cost of LC thin films allows for disposable sensors to be created. This can also allow for irreversible reactions, where sensor regeneration, normally an important property, is impossible.
- The reflective properties of N* LC thin films lend themselves well to optical sensors, in situations where visual interrogation is preferable or other

methods of signal determination are unavailable. Visual interrogation is particularly favourable in consumer sensor applications, due to the low cost and complexity.

Chapter 4

Theoretical model for predicting the properties of time-integrating sensors based on chiral nematic thin films containing responsive dopants

4.1 Background and motivation

The modelling of systems based on liquid crystalline materials is a well established field. Due to the mesophasic nature of LC systems, they are intriguing to measure. The combination of both anisotropy and fluid behaviour in particular means there is much to consider from the position of statistical mechanics, and much investigation has followed. As a result, the behaviour of LC systems under a wide range of conditions is well understood.

One area that has hitherto not been investigated is the performance of N* LC thin films containing reactive chiral dopants as sensors. This is largely due to the novelty of the field, with only a handful of devices in existence. Due to the

potential of these devices, as discussed in Chapter 3, combined with significant optimisation costs, it is desirable to create a framework which could predict the properties of sensors based on as little experimental data as possible.

In this chapter, a new approach to modelling these systems is developed, and compared to experimental data from other chapters. It is demonstrated that changes in pitch, detection limits and realistic operational parameters can be modelled for systems based on a variety of detection mechanisms.

4.2 Overview

The pitch for a given chiral dopant can be calculated from the properties of the nematic host and those of the chiral dopant (notably the helical twisting power (β), enantiomeric excess (e_e) and concentration (c_w)). This is expressed in Equation 4.1. As mentioned previously, the transmission effects resulting from changes in \bar{n} are ignored here, as the impact is considered to be trivial in comparison to the effects associated with the change in the properties of the dopant.

$$p = \frac{1}{(\beta e_e c_w)} \quad (4.1)$$

As these sensors operate on the basis of a change to the properties of the reactive dopant, it becomes important to consider both the initial and final states of each of these properties as a potential route for creating sensors. These can be expressed generally as x_i and x_f for property x . When y and z are the properties not under investigation, the change in pitch can be expressed as in Equation 4.2.

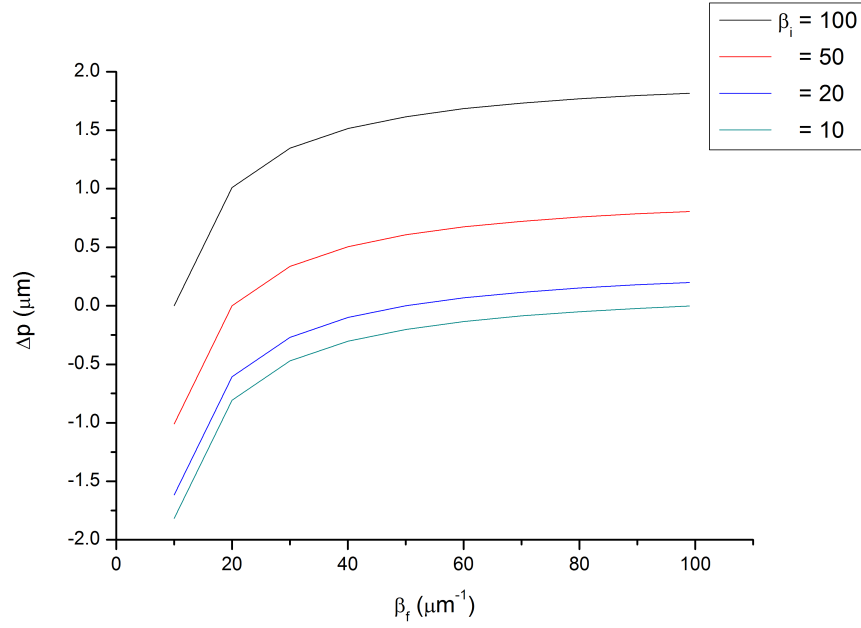


Figure 4.1: A graph showing the effect of changes in β_i on the value of Δp . e_e and c_w are assumed to be constant.

$$\begin{aligned}
 \Delta p &= p_i - p_f \\
 &= \frac{1}{x_f y z} - \frac{1}{x_i y z} \\
 &= \frac{x_f - x_i}{x_f x_i y z}
 \end{aligned} \tag{4.2}$$

As the change in pitch is not dependent solely on the difference between x_i and x_f (Δx), sensors with different values of x_i but the same Δx will have different values for Δp , as illustrated in Figure 4.1.

Another notable feature of Figure 4.1 is that large changes in p only occur when the value of β_f is low. A larger value of $\Delta\beta$ therefore doesn't necessarily increase device performance. The effect of this will be discussed in the conclusion of this chapter.

In order to further develop this model, we must first select the variable we are interested in and how it would be practically utilised in a model system. The three possibilities (varying β , e_e and c_w) are discussed in turn below, along with a brief introduction explaining the variable in question.

4.2.1 Varying helical twisting power (β)

As mentioned in Chapter 3, β represent the helical twisting power of the dopant, which can be thought of as the efficiency of a dopant inducing a helical twist within a given nematic solvent. Due to the reciprocal nature of Equation 4.1, smaller values of β result in larger pitches.

There exist a number of ways to create a chiral dopant. These range from functionalising a chiral molecule with a mesogenic group, in order to aid solubility in a nematic solvent, to using atropisomers such as (*R*)-(+)-1,1'-Bi(2-naphthol) (BINOL) which are inherently chiral due to steric restrictions to rotation. There are two main methods of determining the helical twisting power of a dopant. The first of these is by preparing a film with a known concentration of dopant and then measuring the reflectance or transmission spectrum of light using spectrophotometry. The wavelength of the reflected light can therefore be measured, and from this the pitch calculated.

The second method of determining β is known as the Grandjean-Cano method, in which the LC is placed between two anti-parallel aligned surfaces that are slightly angled (angle = α) with respect to one another. When prepared in this fashion, periodic dark lines emerge in the sample, called Grandjean steps (Figure 4.2). These arise as a result of the inclusion of half-pitch twists (Figure 4.3), with the distance between dark lines (s) being directly related to the pitch according to Equation 4.3.

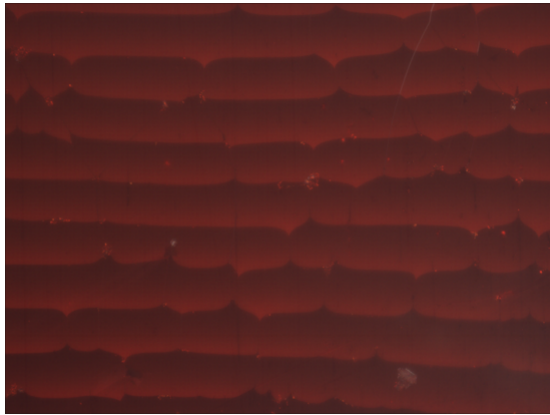


Figure 4.2: Optical microscopy images of a chiral nematic liquid crystal in a wedge cell showing Grandjean steps. Taken through crossed polarisers.

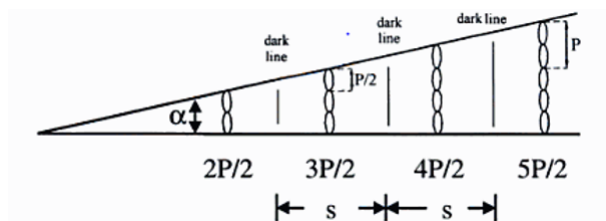


Figure 4.3: Illustration of the Grandjean-Cano method using a wedge cell. Podolskyy et al. (2008)

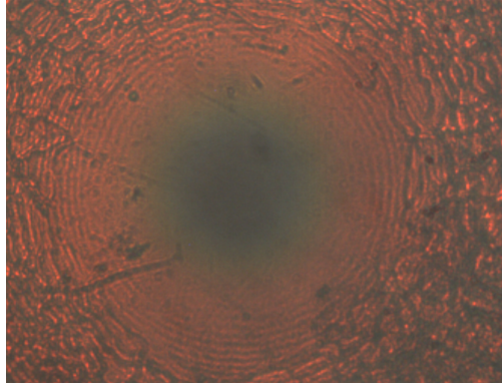


Figure 4.4: Optical microscopy image of a chiral nematic liquid crystal under a lens showing the Grandjean steps. Taken through crossed polarisers.

$$p = 2s \tan \alpha \quad (4.3)$$

The images taken in Figure 4.2 were captured from a non-commercial cell, manufactured by the author, consisting of two pieces of aligned polyimide-coated glass using a combination glass-microsphere/acrylic glue spacer. The measurements obtained from this cell were then used to calculate a value of β for use in later calculations. This is due to the fact that a value of β obtained by UV/Vis spectroscopy would not be independent to the other values used, and therefore may result in conflating errors.

Grandjean also subsequently proposed a second method of creating the Grandjean steps. Placing a lens with a known radius of curvature (r) onto an aligned chiral nematic liquid crystalline film produces a series of concentric rings. An image of this method is included in Figure 4.4, however the variability in the value of β obtained was significant, and therefore the image is included purely for illustrative purposes. The level of variability was assumed to be due to inhomogeneities in the lens surface. In this case, the pitch can be calculated by looking at the difference in the radii of two consequent rings (Δx) (Equation 4.4).

$$p = \frac{\Delta x^2}{r} \quad (4.4)$$

β has been shown to be related to the molecular geometry of the dopant. As the geometry of a dopant depends on the both the electrical and steric properties of the various substituents around a chiral centre, the value of β can simply be altered by carrying out a chemical reaction on or near to the chiral centre. This method allows for the construction of chemosensors, where the reaction between a reactive dopant and an analyte can cause a change in the helical twisting power of a dopant, as outlined in Chapter 3.

Using Equation 4.2, we can express the expected change in pitch as a function of the value of β before and after the dopant-analyte reaction (Equation 4.5)

$$\Delta p = \frac{\beta_i - \beta_f}{\beta_f \beta_i e_e c_w} \quad (4.5)$$

Plotting calculated values of Δp against potential values of β_i and β_f produces Figure 4.1. This gives the maximum possible value of Δp for a given dopant-LC system. In order to compare this to experimental results, it is important to first convert the change in pitch to a change in wavelength of the maximum reflection ($\Delta\lambda_{max}$). This is done by including the mean refractive index, as defined in Equation 4.7

$$\lambda = \bar{n}p \quad (4.6)$$

$$\Delta\lambda_{max} = \bar{n} \frac{\beta_i - \beta_f}{\beta_f \beta_i e_e c_w} \quad (4.7)$$

In most scenarios, the value of $\Delta\lambda_{max}$ obtained will be significantly lower than the ideal value. This can happen when not all of the reactive dopant is converted.

If this is due to insufficient analyte concentration, it allows for quantification of the amount of analyte present, and is highly desirable. Conversely, if the incomplete conversion is due to other factors, such as the existence of an equilibrium point or insufficient time being allowed for the reaction to complete, it can hinder attempts to quantify dopant concentration. It is therefore important to account for the latter by establishing the expected concentration at completion for a device. This can be done by including a concentration factor in Equation 4.7. This concentration factor (C) is defined in terms of the concentration of the analyte initially ($[A]_i$) and once equilibrium has been reached ($[A]_f$) (Equation 4.8).

$$C = \frac{[A]_f}{[A]_i} \quad (4.8)$$

$$\Delta\lambda_{max} = \bar{n}C \frac{\beta_i - \beta_f}{\beta_f \beta_i e_e c_w} \quad (4.9)$$

Lastly, it is important to consider the response of the device to concentrations of analyte lower than that required to induce full conversion. As indicated in Figure 4.1, changes in β do not necessarily give a linear response, particularly when β_i or β_f are close to zero. It therefore follows that the response of a single device may not be linear. In the cases where the predicted value of $\Delta\lambda_{max}$ is large, in order to correctly quantify the amount of analyte present careful device calibration may be necessary. In the majority of cases where $\Delta\lambda_{max}$ is smaller the device response is more likely to be linear, as indicated by the large linear regions of Figure 4.1.

In order to test this model, data from Chapter 5 can be used to predict the device performance, and compare it to experimental results. In doing so, one note of caution must be sounded: due to the number of properties involved in determining the value of β , it is important to include these as a potential source of

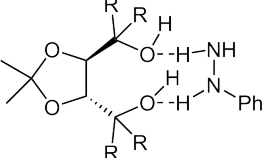
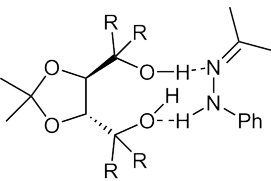
Dopant	λ_{max} (nm)	c_w	e_e
	499.5 ($\pm 0.100\%$)	0.0400 ($\pm 2.69\%$)	0.99 ($\pm 0.50\%$)
	514.5 ($\pm 0.097\%$)	0.0401 ($\pm 2.70\%$)	0.99 ($\pm 0.50\%$)

Table 4.1: Dopant structure, reflection maxima, weight contribution and enantiomeric excess for the chiral dopant before and after the reaction with acetone. Experimental details, including manufacture, are included in Chapter 5.

error in the final predictions. One method of determining this is to use the Root of Sum of Squares (RSS) to combine the individual, uncorrelated sources of error (Equation 4.10).

$$x_{RSS} = \sqrt{x_1^2 + x_2^2 + \dots + x_n^2} \quad (4.10)$$

Another method, the Root Mean Square (RMS), can also be used (Equation 4.11). This has the advantage of producing an estimate of the typical error, which is more useful from a modelling perspective. In this case, both methods will be evaluated.

$$x_{RMS} = \sqrt{\frac{x_1^2 + x_2^2 + \dots + x_n^2}{n}} \quad (4.11)$$

For both RSS and RMS, it is necessary to express the error as a single term. Therefore, first the error in each measurement must be expressed as a percentage (Table 4.1).

From these values, the error in β can be calculated, by adapting Equation 4.1

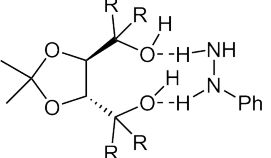
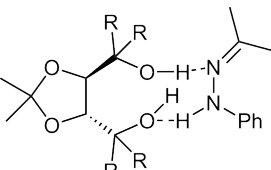
Dopant	β_{abs} (μm^{-1})	err_{RSS} (%)	err_{RMS} (%)
	76.79	± 2.73	± 1.58
	74.71	± 2.74	± 1.59

Table 4.2: Dopant structure, β , RSS error and RMS error for the chiral dopant before and after the reaction with acetone.

to express β (Equation 4.12). These resultant values are summarised in Table 4.2.

$$\beta = \frac{1}{pe_e c_w} \quad (4.12)$$

From this, the total error in the value of $\Delta\lambda$ can now be calculated, when combined with the conversion factor as obtained by GCMS studies, $C = 0.8$ (Figure 4.5). These figures show good experimental agreement with the observed value of $\Delta\lambda$.

As well as the predicted signal, it would be beneficial to establish the operational range of the sensor, defined as the range between the upper and lower detection limits. These limits depend on a number of factors, including the physical dimensions of the sensor, the sensitivity of the detection apparatus and, critically, the absorption of the analyte into the nematic host.

The latter of these was the subject of an investigation by Chang et al. (2011), where they attempted to model the change in λ_{max} as a function of molecular polarisability. They found that the change in the concentration of dissolved VOC could be expressed as an adapted version of Fick's second law, where the ratio

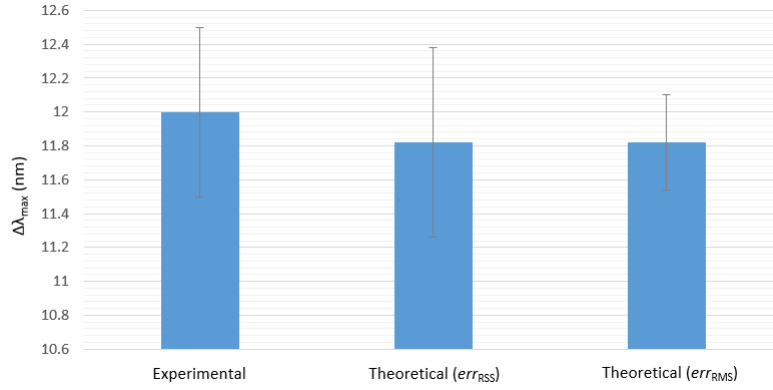


Figure 4.5: A graph comparing the theoretical values, with errors obtained by the RSS and RMS methods, with experimental results from Chapter 5. The error bars on the experimental data indicate the measurement uncertainty of ± 0.5 nm.

weight of VOCs dissolved at a given time (W_t) compared to the weight of VOCs just before phase transition (W_∞) is expressed in terms of the film thickness (L) and diffusion coefficient (D) of the analyte in question (Equation 4.13). From this, they were able to calculate the diffusion coefficient for acetone in the nematic host E7.

$$\frac{W_t}{W_\infty} \approx \sqrt{t \frac{16D}{\pi L^2}} \quad (4.13)$$

Using this value, it is possible to determine the concentration of a film of depth x by considering the diffusion of acetone in one dimension, given the concentration of acetone as outside the film as n_0 , using Equation 4.14. The complementary error function (erfc) can be approximated by using the first two terms of the Taylor series, giving Equation 4.15.

$$n(x, t) = n_0 \operatorname{erfc}\left(\frac{x}{2\sqrt{Dt}}\right) \quad (4.14)$$

$$n(x, t) = n_0 \left[1 - 2\left(\frac{x}{2\sqrt{Dt\pi}}\right) \right] \quad (4.15)$$

Due to the presence of responsive moieties within the nematic host, this model

does not account for the reaction between analyte and the dopant. This effect reduces the concentration of analyte over time, and must be accounted for in this model. This can be accounted for by incorporating the rate equation for the consumption of the analyte into Equation 4.15. These equations can be expressed generally as in Equation 4.16, which depends on the concentration of the responsive moieties and k , the rate constant.

$$\frac{d[A]}{dt} = -k[A]^n[D]^m \quad (4.16)$$

k is in turn defined by Arrhenius equation, where E_a is the activation energy, R is the universal gas constant, T is the temperature and A is the pre-exponential factor (Equation 4.17).

$$k = Ae^{-\frac{E_a}{RT}} \quad (4.17)$$

The actual rate equation for a given analyte-dopant system can only be determined experimentally. Nevertheless, as the concentration of the analyte ($[A]$) will be substantially lower than the concentration of the dopant ($[D]$), as an approximation the reaction can be assumed to be first order with respect to the concentration of analyte. The rate of consumption of analyte can therefore be expressed as in Equation 4.18.

$$\frac{d[A]}{dt} = -k[A] \quad (4.18)$$

The amount of analyte consumed at a given time can be obtained by integration of Equation 4.18 above, by considering the initial concentration of analyte (Equation 4.19)

$$[A]_t = [A]_0 e^{-kt} \quad (4.19)$$

If the rate of diffusion and rate of reaction are similar, then $[A]_0 = n(x, t)$ in Equation 4.15 above, these can be combined to give an overall expression for the amount of analyte dissolved in a film of x thickness after time t , as expressed in Equation 4.20.

$$n(x, t) = (1 - e^{-kt}) \left[n_0 \left(1 - \frac{x}{\sqrt{Dt\pi}} \right) \right] \quad (4.20)$$

In the case of the acetone sensor discussed in Chapter 5, GCMS data indicated that the rate of reaction was substantially slower than the rate of diffusion. In this case, the rate of change in reflection maximum ($\frac{d\lambda}{dt}$) can be expressed as Equation 4.21. This would suggest a linear relationship between $\Delta\lambda$ and analyte concentration, which has been shown experimentally [Cachelin et al. (2016a)].

$$\frac{d\lambda}{dt} \propto k[A] \quad (4.21)$$

Determining the precise value of $[A]$ in this case is not simple. As diffusion into the film is rapid, the concentration of analyte within the film will be in equilibrium with the concentration of analyte in the space immediately above the film, with the rates of diffusion into the film and evaporation from the film being equal. This latter rate in turn depends on the strength of the interaction between the nematic host and the analyte, as well as the vapour pressure of the analyte in solution. As a crude approximation, we will assume that the concentration is equal both inside and without the nematic LC. Therefore, the value of $[A]$ is given by the concentration of analyte to which the sample was exposed.

Additionally, although in theory low levels of dopant conversion should still trigger a change in the N^* pitch, such changes may not be discernible. It is therefore necessary to also calculate the minimum discernible shift ($\Delta\lambda_{min}$). This is more complex to calculate than the change associated with saturation, as it de-

depends on the ability of the detector used to discriminate between different wavelengths. In the case of sensors designed to be assayed visually, this can result in a smaller operational range.

The value of $\Delta\lambda_{min}$ can be expressed in the terms of the difference between the reflection band associated with the unreacted dopant (λ_i) and the reflection band that lies at the minimum discernible wavelength away (λ_{min}), as expressed in Equation 4.22.

$$\Delta\lambda_{min} = \lambda_{min} - \lambda_i \quad (4.22)$$

If partial conversion between dopants can be expressed as an intermediate β value, then we can express the conversion as an intermediate β value, β_{min} , as defined in Equation 4.23.

$$\beta_{min} = \beta_i + \left[(\beta_f - \beta_i) \left(1 - \frac{1 - [D]_t}{[D]_i} \right) \right] \quad (4.23)$$

By substitution of Equations 4.1 and 4.6 we can then work out the concentration of converted dopant required to induce a shift of $\Delta\lambda_{min}$, as shown in Equation 4.24

$$\Delta\lambda_{min} = \bar{n} \frac{1}{\beta_{min} e_e c_w} - \lambda_i \quad (4.24)$$

Using the values from Chapter 5, we can obtain a specific value for $\frac{[D]_t}{[D]_i}$ of 0.095. As the maximum value of $[D]_t$ occurs at saturation when $[D]_t = \check{C}[D]_i$, this can be expressed as 11.1% of the maximum conversion inducing the minimum visible change. This was confirmed experimentally, with λ_{min} being observed at 100 ppm, compared to the 1000 ppm required to induce complete conversion.

Using these figures, we can see that it is mathematically possible to create a detailed image of how these sensors operate from limited knowledge. By combining this with atomistic modelling, it is possible that in the future it will be

possible to simulate a wide variety of sensor targets and predict their operational parameters, along with research to be focussed on those with the highest predicted performance.

We can also use these models to explore the limitation of this sensing mechanism. In particular, as shown in Figure 4.1, large changes in $\Delta\lambda_{max}$ are only possible when either β_{a_i} or β_f are close to zero. As this would require radical changes in the geometry of the dopant this is not possible in the vast majority of cases. As such, more attention should be paid to other detection methods.

4.2.2 Varying the concentration of dopant (c_w)

Another possible detection method, as explored in Chapter 6, is to use a dopant which is consumed in the reaction as the basis of sensing. This could be carried out in a number of ways.

- Reaction of a chiral dopant with the analyte resulting in a material which is insoluble in the LC matrix. This was a contributory factor in the results by Saha et al. (2012b).
- Reaction of a chiral dopant with an analyte resulting in the formation of an achiral compound. This idea is explored more fully in Section 4.2.4.
- Reaction of an achiral solute within the LC matrix resulting in the formation of a chiral compound. This process is the opposite of the above item, although care must be taken to ensure that the reaction is enantioselective, as otherwise a compensated nematic phase is adopted, which is difficult to distinguish from a pure nematic phase.
- Reaction of a chiral dopant which results in the fragmentation of the chiral molecule into small achiral or insoluble fragments. This is the basis of the

dosimeter in Chapter 6.

In all of the above cases, the result can be described as a change in the value of c_w , which describes the concentration of the chiral dopant. As with Section 4.2.1 above, the experimental data obtained in Chapter 6 will be used to determine the accuracy of the models developed here (Section 4.2.3).

As with the systems outlined in Sections 4.2.1 and 4.3, it is possible to adapt Equation 4.2 to reflect a change in c_w (Equation 4.25). As was the case in Section 4.2.1, the reaction kinetics play an important part in predicting the value of c_f after a given amount of time (t) has elapsed. As before, a first-order reaction between the dopant and the analyte is assumed.

$$\Delta\lambda_{max} = \bar{n} \frac{c_i - c_f}{c_i c_f \beta e_e} \quad (4.25)$$

$$c_w = \frac{m_D}{m_D + m_{LC}} \quad (4.26)$$

$$c_f = \frac{m_D e^{-kt}}{m_D + m_{LC}} \quad (4.27)$$

Equations 4.25, 4.26 and 4.27 can be combined to create Equation 4.28.

$$\Delta\lambda = \bar{n} \frac{1 - e^{-kt}}{c_i e^{-kt} e_e \beta} \quad (4.28)$$

Unlike the case outlined in Section 4.2.1, the maximum possible values are not limited, as $\Delta\lambda_{max} \rightarrow \infty$ as $c_w \rightarrow 0$. Therefore, the limitation simply arises from the maximum discernable wavelength of the detector. In the case of visual detection, the maximum value of λ_{max} therefore becomes the upper limit of the visible spectrum, and the maximum value of $\Delta\lambda_{max}$ can be determined by Equation 4.29.

$$\Delta\lambda_{max} = 700 - \lambda_i \quad (4.29)$$

As this value corresponds to a situation where $c_f > 0$, it is therefore possible to calculate the value of c_f that will give rise to a specific $\Delta\lambda_{max}$ and from that to calculate the sensitivity ($\frac{d\lambda}{dc}$) of the device to a given analyte, as expressed in nm/mol.

$$\frac{d\lambda}{dc} = \frac{1}{c_i c_f e \epsilon \beta} \quad (4.30)$$

If the reaction kinetics are known, this case can then be used to create a plot of $\Delta\lambda$ against time for a given analyte concentration, which would allow for accurate quantification of the amount of analyte present in a sample. When combined with the molecular specificity outlined above, this allows for the creation of highly sensitive optical sensors for given VOCs, something that has not previously been possible in portable chemosensors.

4.2.3 Modelling photodegradation

In order to determine ease of photodegradation, it is first necessary to establish the UV dose necessary to induce various amounts of racemisation. The UV dose (D) can be expressed in terms of the UV intensity (I) and the transparency of the barrier between the UV source and the sample (T) as well as the exposure time (t) (Equation 4.31).

$$D = \frac{I}{T} t \quad (4.31)$$

Through the use of circular dichroism spectroscopy, it is possible to directly monitor the value of c_w , provided the initial (c_i) and final (c_f) values are known.

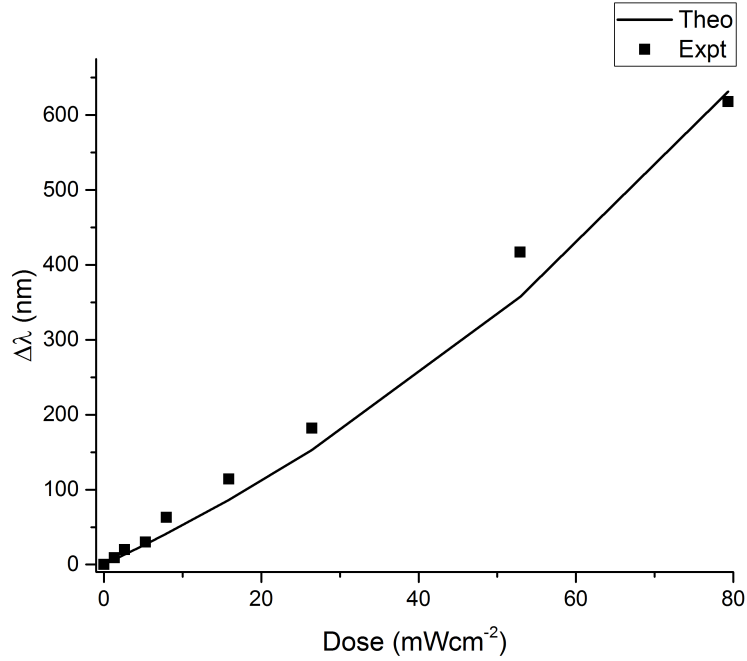


Figure 4.6: A comparison of the theoretical and experimental values of $\Delta\lambda$ for the UV sensor based on the photodegradation of R,R'-bis-2-naphthol. Experimental details are included in Chapter 6.

From this, the ease of degradation (ϵ) can be extracted, expressed in units of $\text{cm}^2\text{mJ}^{-1}$ (Equation 4.32).

$$\epsilon = \frac{c_f - c_i}{D_f - D_i} \quad (4.32)$$

By combining Equations 4.2, 4.31 and 4.32, it is then possible to predict the change in wavelength for a given UV dose, as expressed in Equation 4.33.

$$\Delta\lambda = \bar{n} \frac{D\epsilon}{(D\epsilon - c_w)e_e c_w \beta} \quad (4.33)$$

By comparing the results of this formula with experimental results obtained by UV-Vis spectroscopy, good agreement was found (Figure 4.6).

4.2.4 Change in optical activity

The presence of low concentrations of achiral compounds within a N^* LC has little impact on the N^* pitch [Chang et al. (2012b)]. Therefore, a reaction with an analyte that converts the dopant from a chiral to an achiral form ($D^* \rightarrow D$) would have the net effect of reducing the concentration of chiral dopant present, thereby decreasing the value of c_w . Such a system can be envisioned when the reaction between the analyte and the dopant results in the formation of a plane of symmetry in the responsive dopant, as illustrated in Figure 4.7. The reverse situation would similarly induce a change, creating a nematic system that would spontaneously transform into a N^* system when exposed to an analyte, although it is more complex. For this example, we will focus purely on the $D^* \rightarrow D$ system.

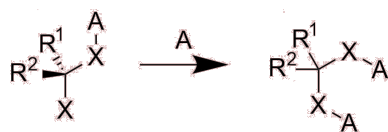


Figure 4.7: The reaction between an analyte (A) and a chiral dopant resulting in the formation of an achiral compound.

Such a system has several notable advantages. The most significant of these is that such systems should portray an unprecedented degree of selectivity: if the analyte is small, such as is the case with VOCs, then only that specific analyte will trigger the chiral nematic to nematic ($N^* \rightarrow N$) phase transition. The reaction with a molecule that shares the targeted functional moiety but is structurally different will not result in the $N^* \rightarrow N$ phase transition occurring, as is illustrated in Figure 4.8. Such selectivity is highly desirable, with applications possible in many industries.

Although the principle of carrying out a chiral \rightarrow achiral transition has not experimentally been performed, a similar system was explored by Saha et al. [Saha et al. (2012b)]. In this case, an irreversible reaction between a binaphthylorthosili-

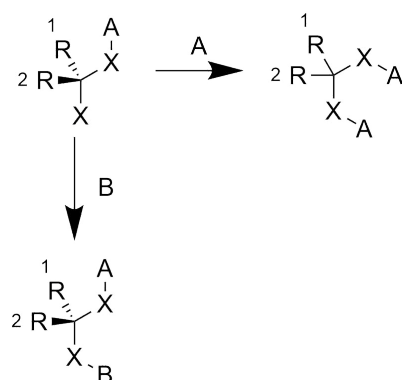


Figure 4.8: An illustration of the molecular selectivity of this dopant system. In this case, molecules A and B share a functional moiety that is targeted by the reactive chiral dopant, but are structurally dissimilar.

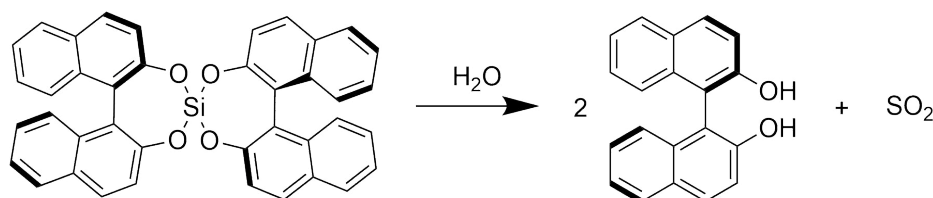


Figure 4.9: The reaction between the silicate ester of BINOL and water yielding BINOL. Note the reaction is irreversible, hence this sensor acts as a time integrating sensor, or a dosimeter.

cate ester and water resulted in the formation of BINOL, which has a significantly lower value of β , alongside a lower solubility in the nematic host E7 (Figure 4.9). In this case, as the reaction proceeds, the amount of orthosilicate present decreases, leading to a lower c_w value. Simultaneously, the concentration of BINOL increases, as two equivalents of BINOL are produced for each orthosilicate consumed.

Using the hydrolysis data provided by Saha et al., it is possible to model the degradation of the silicate ester of BINOL, and from this generate a model for the predicted value of λ_{max} after a given time (Figure 4.10).

The model produced matches the experimental data well (correlation = 0.95). It is possible that including the impact of the created BINOL would result in even

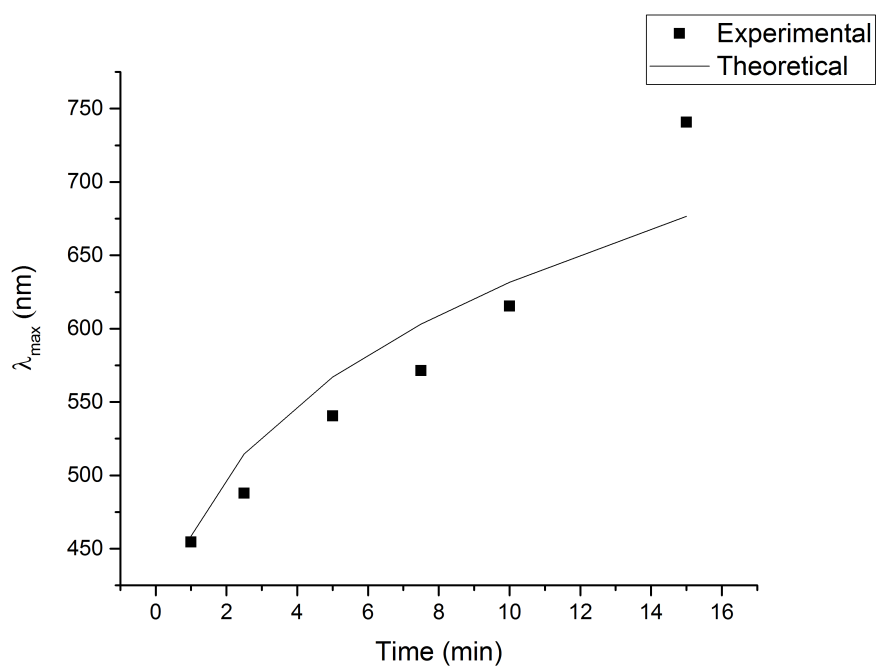


Figure 4.10: The predicted change in λ_{max} compared to the observed values. N.B. this does not include the contribution from BINOL. Experimental details located in Saha et al. (2012b).

better correlation. However, monitoring the effect of two dopants with widely different solubilities and values of β is unfortunately beyond the scope of the model outlined here.

4.3 Varying the enantiomeric excess (e_e)

This section remains entirely theoretical, as no suitable model data can be found. As such, it remains brief. Although it is a potential target for future work, it is not discussed as such, due to the limited nature of racemisation reactions. It is nonetheless included in this work for the sake of completeness.

An optical isomer is a molecule that shares the same molecular configuration of the original molecule, but is non-superimposable on the original molecule. They are called optical isomers due to the difference in the outcome when a solution of one optical isomer is exposed to a plane of polarised light.

This type of isomerism has several causes. The most common is the existence of a stereogenic centre: a carbon atom with four different substituents. When the mirror image of such a molecule is taken, the two forms are non-superimposable, as shown in Figure 4.11.

There are other methods of inducing optical isomerism. These are through the use of inherently chiral molecules such as calixarenes or fullerenes, or planar chirality such as is present in bis-2-naphthol. In both these cases it is the structure

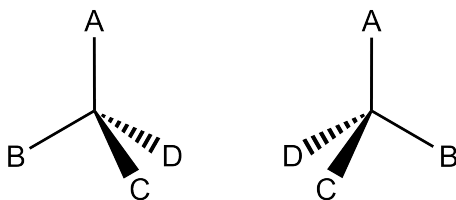


Figure 4.11: A representation of a stereogenic centre. Note that the two molecules are not superimposable, despite having identical structures.

of the molecule that prevents the interconversion between isomers.

In order to express the extent of racemisation it is important to be able to quantify the amount of the optical isomers present within a sample. This is done through the enantiomeric excess, which is defined as in Equation 4.34.

$$e_e = \frac{[R] - [S]}{[R] + [S]} \quad (4.34)$$

As in Section 4.2.1, Equation 4.2 can be adapted to express a sensor that operates on the basis of a change in the value of e_e (Equation 4.35).

$$\Delta p = \frac{e_i - e_f}{e_i e_f \beta c_w} \quad (4.35)$$

As before, there is a non-linear relationship between e_e and Δp , with high values of the latter only observed when e_i or e_f approach zero.

This method has several advantages over sensing based on a change in β . The major advantage is that e_e can adopt any possible value within the range 0 - 1, whereas the value of β_i is limited to the range of $\beta_i - \beta_f$. This means that a wider range of values of Δp are expected.

There are two primary methods by which a change in e_e can be induced for standard stereogenic centres

- Altering the valence of the stereogenic centre. This can be observed by the loss of enantiomeric purity in molecules that undergo SN_1 reactions, where inversion of chirality can occur.
- Thermal racemisation. Inversion can occur at the stereogenic centre if enough energy is supplied. As inversion is random and can occur multiple times to a given molecule, this can very rapidly result in complete racemisation.

In the case of planar chirality, it is possible to convert between optical isomers by adding sufficient energy to overcome the energy barrier to free rotation. It is also possible to induce racemisation *via* the creation of an excited state which has a lowered barrier to rotation, as has been described by Solntsev et al. (2009). Attempts have also been made at inducing chirality through illumination with circularly polarised light, such as by Zhang and Schuster (1992), although these have been unsuccessful.

4.4 Conclusion

The aim of this section was to demonstrate that it is possible to predict aspects of the performance of a sensor based on basic information about the properties of the reactive components of the mixture, notably the change to the helical twisting power, concentration and enantiomeric excess of the dopant.

We have demonstrated that it is possible to determine the performance of a given dopant-analyte system with a high level of accuracy from basic information. This will help with our stated aim of creating systems for effectively screening dopants without heavy optimisation.

In particular, we have demonstrated that although investigations in this area have previously focused primarily on devices that respond by a change in the helical twisting power of the dopant, other methods of operation are not only possible but could produce highly efficient devices.

We have also been able to draw conclusions which will hopefully be able to inform future investigation in this area. There are two primary conclusions drawn:

- While substantial changes in one of the properties governing the interaction of a chiral dopant with the nematic host (e.g. helical twisting power) is beneficial, it is possible to further extend the sensitivity of these systems by

ensuring that the initial or final state lies close to zero.

- There exist inherent limitations to systems based on a change in helical twisting power that do not extend to systems based on other variables, and that the study of these latter systems has been sadly neglected

The methods analysed do not cover all possible mechanisms for a system based on a responsive chiral dopant within a nematic host, and further investigation is needed to determine the comparative efficiency of other sensing regimes, such as systems based on an interaction between the chiral host and another component of the liquid crystalline mixture. Nevertheless we believe that we have provided a firm theoretical foundation that was previously lacking, and believe that this method can provide a framework to allow for more systematic investigation of these exciting materials in the future.

Chapter 5

Optical monitoring of ketone vapours by the use of a TADDOL-phenylhydrazine complex

N.B. This work was carried out in collaboration with J. P. Green and is the subject of the following publication: P. Cachelin, J. P. Green, T. Peijs, M. Heeney and C. W. M. Bastiaansen, *Adv. Opt. Mater.*, 2016, **4**, 592-596.

5.1 Introduction

This chapter describes in detail the work undertaken in the investigation of an acetone sensor based on a phenylhydrazine-TADDOL complex as a reactive chiral dopant within a chiral nematic (N*) liquid crystal (LC) matrix.

I am indebted to Joshua P. Green and Martin Heeney for their assistance in this work, in particular the characterisation of the phenylhydrazine-TADDOL complex by NMR, and GC-MS studies.

In this chapter, I will give a brief overview of what constitutes the state-of-the-

art in acetone sensing, as well as looking at other LC-based acetone sensors. This is covered in Section 4.1

An outline of the experimental work undertaken is given in Section 5.3. This will outline the experiments performed. This is followed by the Results and Discussion (Section 5.4) and the Conclusions (Section 5.5).

5.2 Background

5.2.1 Acetone

Acetone is widely used as a solvent, both in industry and in the home; it's ability to dissolve seemingly any organic compound has fascinated undergraduate chemistry students for years. Despite being freely available, acetone has a number of side-effects from overexposure. These range from mild side-effects such as irritation of the mucous membranes and headache to more serious effects such as central nervous system depression and cardiorespiratory failure at extremely high levels [Arts et al. (2002); Ziem and Castleman (1989); Fujino et al. (1992); Wigaeus et al. (1981); Kumagai et al. (1998)]. Additionally, there are neurobehavioural effects from prolonged exposure to low concentrations of acetone vapour [Dick et al. (1989)].

In order to avoid these side effects, health and safety bodies such as the UK's Health and Safety Executive (HSE) and the American Conference of Governmental Industrial Hygienists (ACGIH) set out limits for maximum exposure to acetone vapour. These typically consist of limitations for both short term exposure limits (STEL) as well as longer term time weighted average (TWA) that is designed to limit exposure over a typical working day. Their guidance is summarised in Table 5.1. In order to follow such guidance, it is important that employers have access to systems that are able to accurately monitor the atmospheric concentration of

Body	STEL (ppm)	TWA (ppm)
HSE	1500	500
ACGIH	1000	750

Table 5.1: The exposure limits set out by the UK and US health and safety bodies for exposure to acetone vapour.

acetone within their workplaces.

A second application for acetone sensors is in the monitoring of type 1 diabetes mellitus (T1DM). John Rollo noted in his 1798 work *An Account of Two Cases of Diabetes Mellitus* of the sweet, rotten smell present on the breath of someone in a diabetic coma [Rollo (1798)]. This smell arises due to the presence of significant quantities of acetone on the breath, as a result of diabetic ketoacidosis (DKA). DKA occurs when insufficient insulin causes glucagon levels to rise. This results in lipolysis which increases the amount of free fatty acids present in blood plasma. These free fatty acids are then converted to ketoacids, which increase the acidity of the blood and result in the concentration of acetone in the breath rising. If untreated, DKA can be fatal, and prior to the discovery of insulin therapy, a diabetic coma would often result in death.

The mechanism of ketogenesis is outlined in Figure 5.1. Fatty acids are broken to acetyl-CoA as usual using the β -oxidation pathway. Under normal conditions, the acetyl-CoA produced then enters the Krebs cycle for further breakdown. Under ketogenic conditions, however, the amount of acetyl-CoA produced is in excess of the ability of the Krebs cycle to process. This is then further processed to produce ketone bodies, *via* the intermediates of HMG-CoA and acetoacetate. Acetoacetate can undergo non-enzymatic decarboxylation, which results in the formation of acetone.

This process is triggered by a lack of activity in the Krebs cycle, caused by a low level of glucose and its products such as oxaloacetate. This can be caused

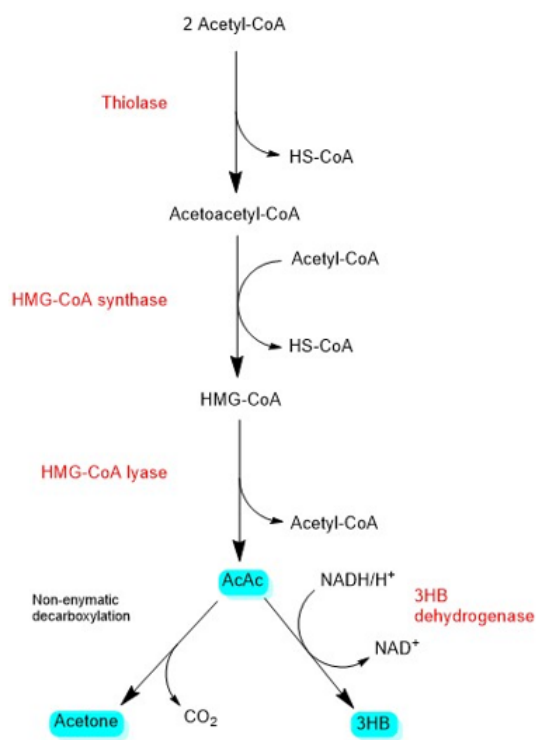


Figure 5.1: The ketogenic pathway that results from the breakdown of free fatty acids.

by a number of conditions, including fasting, diet, disease and strenuous exercise [Spaněl et al. (2011)]. In many of these circumstances, ketosis is a natural metabolic response and ketoacidosis is unlikely to occur. Ketoacidosis can also occur; albeit rarely; in alcoholic patients, and is identified in these cases as alcoholic ketoacidosis [Wrenn et al. (1991)]. These demonstrate that elevated levels of acetone on the breath is not necessarily indicative of DKA, and is regularly present in subjects that are non-diabetic.

These are important considerations for any technology based on the measurement of breath acetone levels to monitor T1DM, but could potentially be circumvented by concurrently monitoring another volatile biomarker, such as methyl nitrate. Despite these setbacks, breath acetone detection remains an attractive target, particularly for patients that feature poor compliance with blood glucose monitoring, such as children.

5.2.2 Non-liquid crystalline sensors for acetone

A number of detection techniques have been used to monitor levels of acetone present in the air, utilising a wide range of different principles of detection, ranging from spectroscopic signatures to chemical reactions. The most well established of these are gas detector tubes. These operate on the basis of drawing a fixed volume of gas through a tube. The tube contains a reagent that reacts with the analyte in question, forming a coloured compound. The concentration of analyte present can be measured by how far along the tube the colour change is observed (Figure 5.2). By altering the bore of the tube, it is possible to create sensors with different operational ranges (defined as the range of concentrations that produce a unique signal in the sensor). Such systems are available for a wide range of analytes, including acetone, and require little in the way of equipment, producing a clear colourimetric signal. However, such sensors are not capable of detecting the low

concentrations of acetone (<10 ppm) required for monitoring T1DM. They are also relatively expensive and non-reusable, meaning that frequent monitoring of concentrations such as that required by T1DM sufferers becomes expensive. As a result, there has lately been a slew of sensors aimed at targeting low concentrations of acetone vapour. Summarised in Table 5.2.3 is a selection of such techniques, including the sensing platform and the concentration range achieved. As a reference, detection in the range of 0.1 - 10 ppm is usually considered suitable for breath acetone monitoring.

5.2.3 Liquid crystalline sensors for acetone

Acetone sensors utilising LCs have also been investigated. The background of sensing with LCs is explored more fully in Chapter 3, but the various acetone sensors developed are discussed below.

The ability to detect the presence of VOCs by monitoring the change in reflection band of a N* LC was first reported by Fergason in 1964 [Fergason (1964)]. One of the VOCs tested by Fergason was acetone, which induced a red → blue shift in a mixture of cholesterol derivatives. This behaviour cannot be explained in terms swelling of the cholesteric host material, which would result in a red-shifting of the reflection band. Instead, the absorption of acetone into the cholesteric host has the effect of decreasing the N* pitch. Although Fergason did not speculate as to the mechanism in play, the fact that the composition of the cholesteric LC could determine if a red- or blue-shift was observed suggests that chemical interactions (such as improved LC solvation) between the VOC and a component of the cholesteric LC is responsible. These effects were later further investigated by Winterbottom et al., who found that by controlling the composition of a cholesteric LC it was possible to change the effect of different VOCs [Winterbottom et al. (2003)]. In this latter case, the introduction of VOCs always

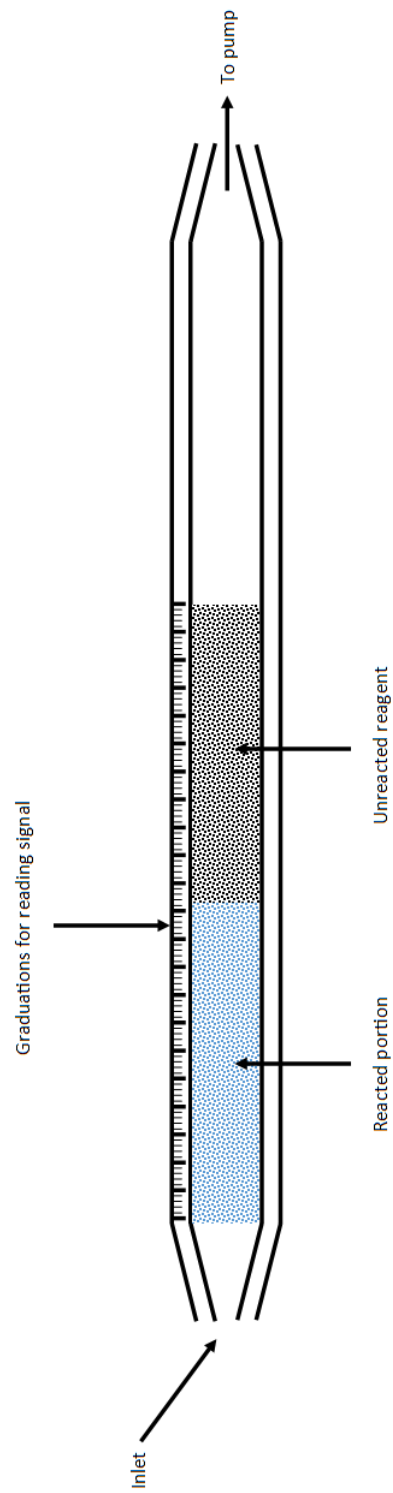


Figure 5.2: A schematic of a gas detection tube.

Sensing platform	Detection Range	References
Gas Detector Tube	10-15,000 ppm	
Selected Ion Flow Tube-MS	>1 ppb	[Adams and Smith (1976); Smith and Španěl (2005)]
Cavity Ringdown Spectroscopy	0.5-5 ppm	[Wang and Mbi (2007); Wang et al. (2010)]
Resistive Chemosensors	>200 ppb	[Wang et al. (2009); Righettoni et al. (2012)]
Chemiluminescence	5-200 ppm	[Zhu et al. (2002); Tang et al. (2008)]

resulted in a red-shift of the reflection band.

Lai et al. (2008) used a PDLC-CNT material as a sensor for acetone. On exposure to high levels of acetone vapour (>1000 ppm) reorientation within the LC domains of the PDLC resulted in the formation of conducting networks of CNTs, decreasing the resistivity of the film. This is similar to earlier work by Chang et al. (2012b) on creating hybrid N*/CNT materials for high detection range monitoring of VOCs, including acetone. Both of these devices are likely to struggle significantly with issues of cross-sensitivity, due to the non-selective nature of VOC absorption.

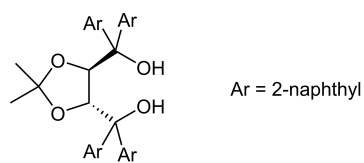
In order to create sensors capable of discriminating between VOCs, it is necessary to specifically target a single analyte or group of analytes. One method is to use a reactive component within a N* LC that changes the bulk property of the film when exposed to the analyte in question. This method is explored below.

5.3 Experimental

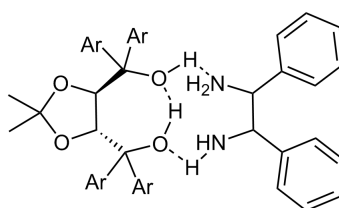
This work builds on work undertaken by Han et al. in creating a CO₂ sensor based on a diphenyldiamine complex with a chiral auxiliary [Han et al. (2010a)]. This approach was chosen as it allows for the possibility of using reactive components that have low values of β or are achiral. The complexation with a dopant with high helical twisting power allows for greater flexibility in the dopants chosen.

The chiral auxiliary chosen by Han et al. was (4*R*,5*R*)-2,2-dimethyl- α,α',α' -teranaphthyldioxolane-4,5-dimethanol (TADDOL, **1**). This complexes with 1,2-diphenyl-1,2-ethylenediamine, to create compound **2**, as was demonstrated by ¹H-NMR and IR spectrometry.

Hydrazines are well known for their reactivity towards carbonyls. The reaction between 2,4-dinitrophenylhydrazine (also known as Brady's reagent) and a



1



2

carbonyl is used as a standard test to determine the type of carbonyl present (Figure 5.3).

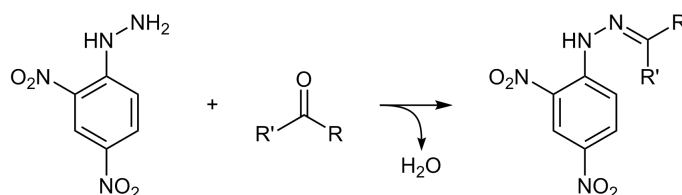


Figure 5.3: The reaction between Brady's reagent and a carbonyl. The colour of the product can be used to determine the type of carbonyl present, and melting point analysis can be used to compare to a library of known carbonyls.

Due to the explosive nature of Brady's reagent, phenylhydrazine (PH) was chosen as the reactive component for this sensor. The aim of this work is to investigate the complexation of PH with TADDOL to form a TADDOL-PH complex, and to investigate the use of this complex as a reactive dopant within a N* LC thin film as a sensor for acetone.

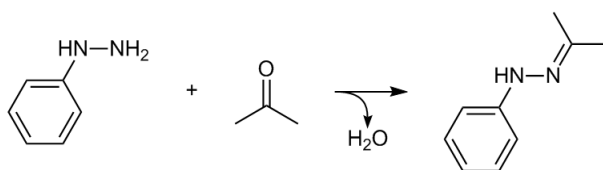


Figure 5.4: The reaction between PH and acetone, resulting in the formation of the imine product, 1-isopropylidene-2-phenylhydrazine (PA).

5.3.1 Reaction between acetone and phenylhydrazine

The reaction of PH with acetone was carried out, both with and without the presence of an acid catalyst. The reaction was carried out without solvent, under an atmosphere of N_2 , and the obtained product evaluated by 1H -NMR and GCMS.

5.3.2 Complexation of phenylhydrazine and 1-isopropylidene-2-phenylhydrazine with TADDOL

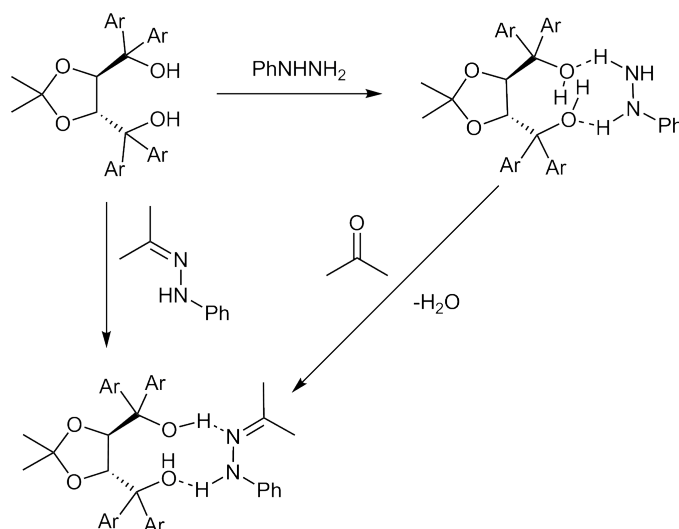


Figure 5.5: The structure and formation of the three dopants discussed. Clockwise from upper right: TADDOL, TADDOL-PH, TADDOL-PA.

Solutions of TADDOL, TADDOL with PH and TADDOL with PA were prepared in *o*-xylene. The solutions were stirred overnight under N_2 in order to en-

courage complexation. The dopants were then isolated, and dissolved in E7. Thin films were prepared by spin-coating the solution onto glass coated with rubbed polyimide. The open films were then analysed by UV/Vis spectroscopy and the helical twisting power of the dopants determined.

5.3.3 Exposure of TADDOL/PH complex to acetone vapour

Solutions of TADDOL, the TADDOL/PH complex and the TADDOL/PA complex in E7, as described in Section 5.3.2, were exposed to air saturated with acetone vapour, as well as acetone vapour at concentrations of 10 - 10000 ppm. These latter experiments were carried out by introducing pure acetone into a sealed vessel containing the sample and allowing it to evaporate. The change in helical twisting power was measured by absorption spectroscopy.

5.3.4 Exposure of TADDOL/PH complex to other ketone vapours.

The TADDOL/PH complex in E7 described in Section 5.3.2 was exposed to a number of ketones and aldehydes, including cyclohexanone, 2-pentanone, 2-methyl-4-pentanone and pentanal. The resulting changes in helical twisting power were measured by absorption spectroscopy.

5.3.5 Exposure of TADDOL/PH complex to other common solvents.

In order to determine the cross-sensitivity of the TADDOL/PH complex to non-ketonic VOCs samples were prepared as before and exposed to 10,000 ppm of propan-2-ol, ethanol and water vapour.

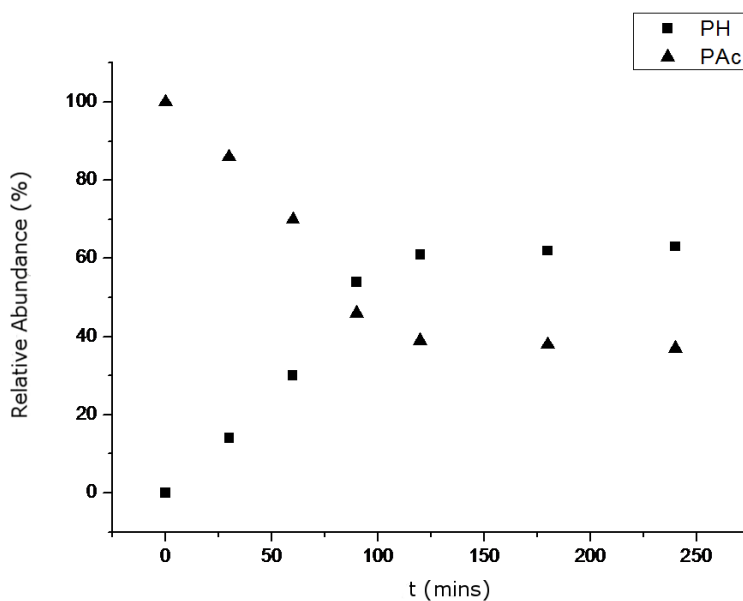


Figure 5.6: Relative abundance of PH and PA over time, as measured by GC intensity. Reaction was carried out without an acid catalyst. Solvent = E7.

5.4 Results and Discussion

5.4.1 Reaction between acetone and phenylhydrazine

The reaction between PH and acetone was monitored by GC-MS (Figure 5.6). The reaction was found to reach an equilibrium at $C = 0.6$, with C defined as in Section 4.2.1:

$$C = \frac{[D]_f}{[D]_i} \quad (5.1)$$

The reason for this equilibrium existing was not determined. One hypothesis is that the water formed as a result of the imine formation reacts with the hydrazinyl moiety, preventing the formation of further product. This is evinced by the existence of other products within the $^1\text{H-NMR}$ studies. (Figure 5.7).

One point of note is the slow rate of reaction between PH and acetone. This

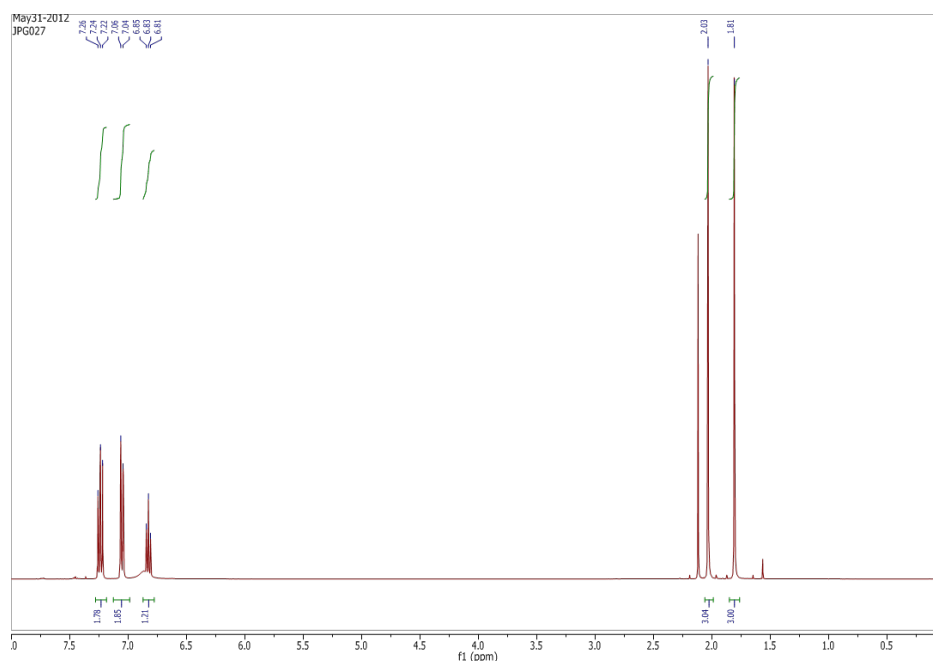


Figure 5.7: ^1H -NMR of the product of the reaction between PH and acetone. The unassigned peaks correspond to unreacted acetone. Solvent is CDCl_3 .

significantly limits the application of these devices to situations where analysis time is not important. If shorter reaction times are required, this could be achieved by increasing the temperature at which the reaction is carried out, thereby increasing the rate constant (k) of the reaction, in line with the Arrhenius Equation (Equation 5.2).

$$k = Ae^{\frac{E_a}{RT}} \quad (5.2)$$

5.4.2 Complexation of phenylhydrazine and 1-isopropylidene-2-phenylhydrazine with TADDOL

The formation of this complex was confirmed by ^1H -NMR (Figure 5.8). The ^1H NMR spectrum of a 1:1 molar ratio mixture of the TADDOL/PH complex

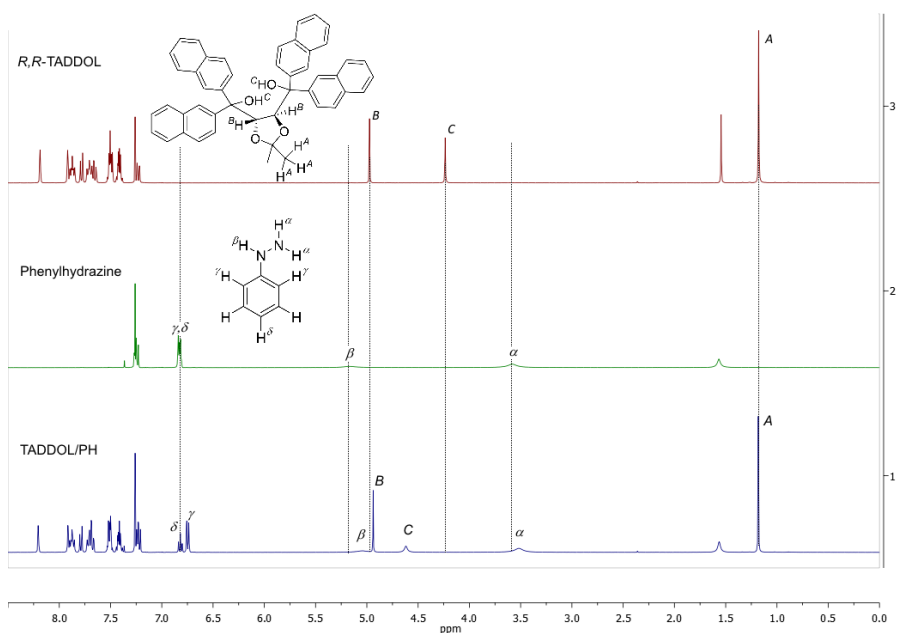


Figure 5.8: ^1H -NMR spectra of (top) TADDOL, (middle) PH and (bottom) TADDOL/PH.

shows several important changes in comparison to those of samples of pure PH and TADDOL. The majority of the aromatic peaks in both TADDOL and PH are largely unaffected by complexation, with changes in chemical shifts of less than 0.02 ppm seen for all peaks except those corresponding to the protons in *ortho*- positions of phenylhydrazine, which shift upfield from around 6.83 to 6.74 ppm in the presence of TADDOL. This is expected as the naphthyl protons on TADDOL are molecularly distant from the predicted complexation site, while the *ortho*- position of PH is directly attached to the hydrazine functional group. The $-\text{CH}$ protons on the TADDOL dioxolane ring show slight shielding from 4.97 to 4.94 ppm, while the methyl groups show no change from their original position. By far the largest shifts are seen for the protons corresponding to the functional groups (hydroxyl for TADDOL and hydrazinyl for PH). The protons of the latter shift upfield from 5.17 to 5.05 ppm and 3.58 to 3.52 ppm for the $-\text{NH}-$ and $-$

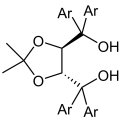
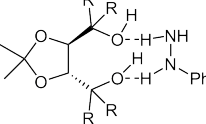
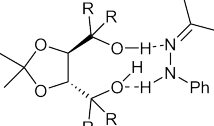
Dopant	λ_{max} (nm)	c_w	pitch (nm)	β (μm^{-1})
	493.5	3.44	324	90.62
	499.5	4.00	328	76.79
	514.5	4.01	338	74.71

Table 5.2: The λ_{max} , c_w , pitch and β for solutions of the dopants in E7.

NH₂ protons, respectively, with the hydroxyl protons shifted downfield from 4.24 to 4.62 ppm. The fact that the hydrazinyl protons shift upfield and the hydroxyl protons downfield indicates that hydrogen bonds form between the two molecules with –NH–/–NH₂ acting as hydrogen bond donors and the –OH groups acting as hydrogen bond acceptors.

When the complexes of TADDOL, TADDOL-PH and TADDOL-PAc were dissolved in E7 at a concentration of 4 wt%, films aligned on a rubbed polyimide surface (thickness $\sim 20 \mu\text{m}$) of the LC-dopant solution exhibited a vivid blue colour, with $\lambda_{max} \sim 400 \text{ nm}$. From the values of λ_{max} , the precise values for β were calculated, using the value $\bar{n} = 1.52$ for E7 (Table 5.2). It was assumed that the low concentration of dopant involved made it unlikely that the value of \bar{n} would have altered significantly from the value associated with pure E7

Notably, the change in β is small, which is reflected in the small change in reflection maximum. The cause and effect of this is examined in more detail in Section 4.2.1. Due to the small value of $\Delta\lambda_{max}$, it is predicted that this device will exhibit low sensitivity.

5.4.3 Exposure of TADDOL/PH complex to acetone vapour

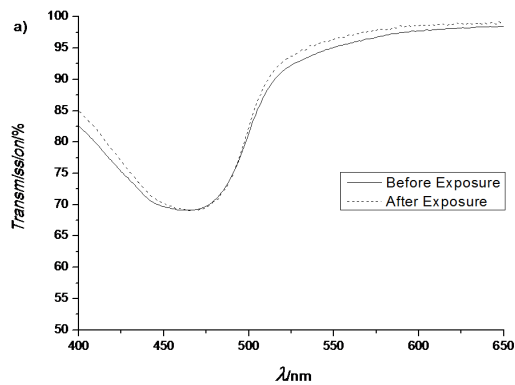
When films consisting of the complexes of TADDOL with PH and PA, as well as pure TADDOL dissolved in LC mixture E7 were exposed to air saturated with acetone vapour, the result was a very rapid increase in reflection maximum ($t \approx 1-10s$), followed by LC droplet formation as the film was dissolved. This matches previous observations that exposure of LC films to high concentrations of acetone vapour disrupts the liquid crystalline order and eventually results in the formation of an isotropic liquid. [Chang et al. (2012b)].

In order to ensure that changes in film thickness or underlying polymer morphology were not responsible for the results observed, it is necessary to sample the same area for each sample. This was achieved through the use of sample holders which were affixed to the body of the photospectrometer, ensuring that sample movement was minimal.

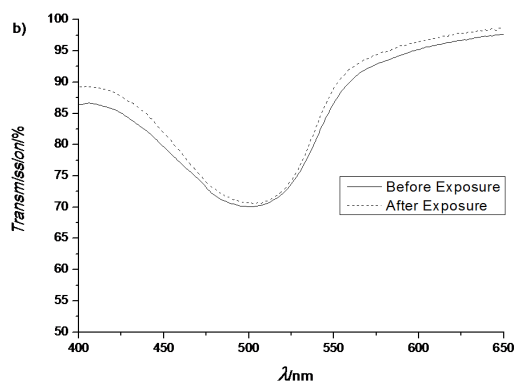
On exposure to acetone vapour at the concentration of 10,000 ppm, this disruption was avoided, although there was still a rapid red-shifting of the reflection band due to the absorption of acetone vapour. This red-shifting was reversible, with the λ_{max} of films of TADDOL and TADDOL/PA returning to their previous values after being removed from the presence of acetone vapour (Figures 5.9a & 5.9b).

When the TADDOL-PH dopant was exposed to acetone vapour at 10,000 ppm, the change was not completely reversed, and a small shift in λ_{max} was observed (Figure 5.9c). This corresponds to a change in $\beta = 1.7 \mu\text{m}^{-1}$, 85% of the change from PH \rightarrow PAc. Due to the low performance of the device, this discrepancy was not investigated further.

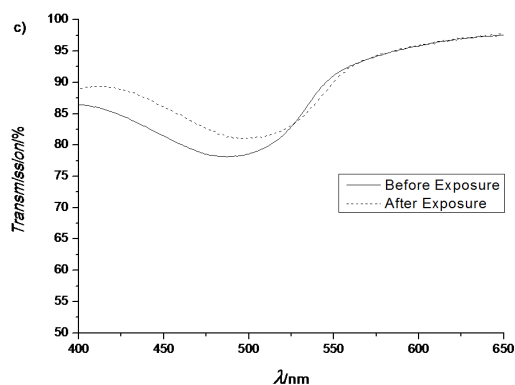
In order to determine the sensitivity of the device, a series of experiments where films were exposed to concentrations of acetone in the region of 10 - 1,500 ppm were performed (Figure 5.10). Two regimes can clearly be seen: an active



(a)



(b)



(c)

Figure 5.9: The absorption spectrum of (a) TADDOL ($c_w = 3.56$), (b) TADDOL-PAc ($c_w = 4.01$) and (c) TADDOL-PH ($c_w = 4.00$) in E7 before and after exposure to 10,000 ppm acetone vapour. All spectra recorded at the same temperature (20 °C).

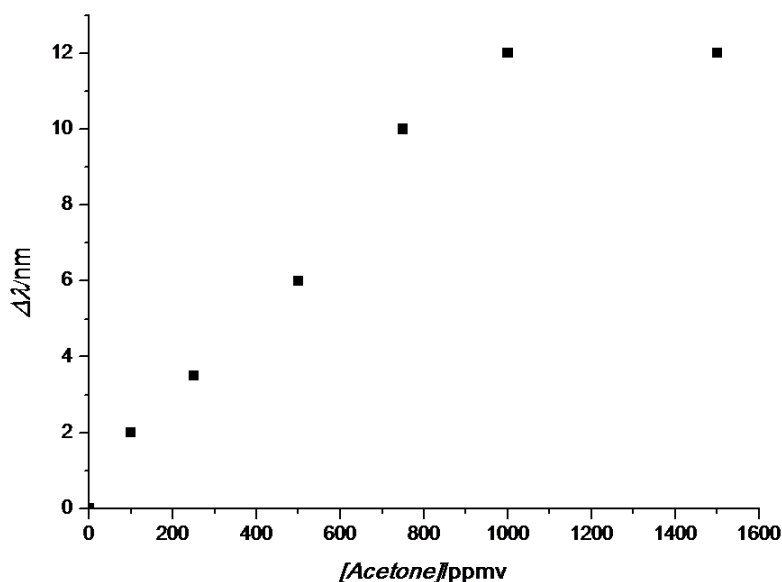


Figure 5.10: A plot of acetone concentration vs. change in λ_{max} ($\Delta\lambda$).

region comprising of the linear change in response observed between 10 - 1000 ppm and an inactive region above 1,000 ppm. As mentioned in Chapter 4, these systems will undergo saturation at a point where all active sites are occupied, resulting in a flat response above the saturation point. By defining the sensitivity in the active region of 10 - 1,000 ppm, s , as the change in the signal per unit of input change (Equation 5.3), the sensitivity of this device can be determined to be 0.0012 nm/ppm in the region corresponding to the peak of maximum reflectance. As a point of comparison, sensors based on the reversible absorption of acetone into a chemically inert matrix have sensitivities on the order of 1 nm/ppm [Chang et al. (2012b)]. The key distinguishing feature is that these devices act as dosimeters, with the output representing the total dose over time, as opposed to the current level of analyte present. This distinction is discussed more fully in Chapter 3.

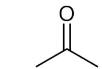
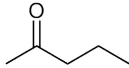
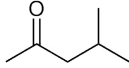
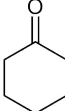
Ketone analyte	λ_{max} (nm)	pitch (nm)	β (μm^{-1})
None	530.5	349	76.79
	541.5	356	75.01
	550.0	362	73.85
	531.0	349	76.49
	564.0	371.0	72.01

Table 5.3: Values of λ_{max} , pitch and β for a variety of ketone analytes.

$$s = \frac{\Delta\lambda}{[D]} \quad (5.3)$$

5.4.4 Exposure of TADDOL-PH complex to other ketones

The low sensitivity of the acetone sensor arises from the small change in β . This is hypothesised to be due to the small change in the molecular geometry of the TADDOL dopant. In order to demonstrate this principle, reactions with a series of ketones that have greater steric bulk were carried out. These results are summarised in Table 5.3.

As can be seen from Figure 5.11, with the exception of 4-methyl-2-pentanone, increasing the size of the analyte results in a decrease in the value of β . The similar values of β in the case of no analyte and 4-methyl-2-pentanone suggest that no reaction is taking place in this scenario. One possible cause is the branching incorporated in the isobutyl moiety of 4-methyl-2-pentanone disfavours the reaction from occurring, although this was not proven.

The inverse relationship between steric bulk and β suggests that the effect of

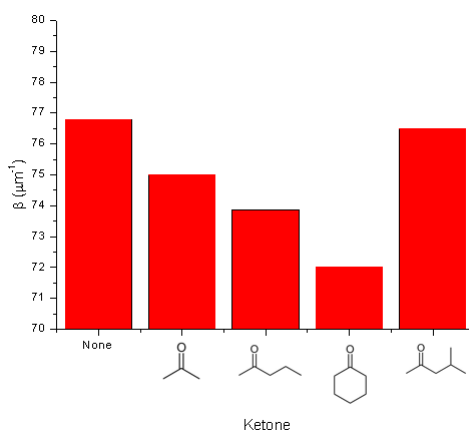


Figure 5.11: A plot of ketone analyte against β of the resultant complex with TADDOL-PH.

analyte inclusion on the molecular geometry of the TADDOL moiety is responsible for the change in λ_{max} observed. In order to investigate this, computational models of the dopant complexes, before and after reaction with the various analytes, were developed. It was hypothesised that the dihedral angle between the two chiral centres was responsible for the change in β .

Due to the low performance of these sensors ($\Delta\lambda_{max} = 33.5$ nm in the best performing case) no further investigations were carried out.

5.4.5 Exposure of TADDOL/PH complex to other common solvents.

After extended (18 hours) exposure to propan-2-ol, a shift of 2 nm was observed. In all other cases, no change in the reflection maximum was observed. This indicates a low level of cross-sensitivity, and these devices can be considered to be significantly selective towards ketones.

5.5 Conclusion

Although it has been demonstrated that it is possible to create chemical dosimeters by utilising an irreversible reaction between a chiral dopant and an analyte within a nematic matrix, these experiments demonstrate well the twin weaknesses of utilising a change in β as the fundamental operating principle of a sensor:

1. Unless there is a substantial change in the value of β , as well as one of the values of β lying close to 0, then the value of $\Delta\lambda_{max}$ is limited. Given the definition of sensitivity outlined in Equation 5.3, this limited value of $\Delta\lambda_{max}$ directly impacts the overall sensitivity of the device. This means that it is not only necessary to identify a dopant that possesses both the ability to interact with the chosen analyte and a substantial β , but that even when developed such a dopant might not have a sufficient sensitivity to produce a viable device.

2. It is difficult to predict the value of β purely from a chemical structure. While there has been much development in this field, notably by the group of Wilson at Durham University [Wilson and Earl (2001)], calculation of β purely from the chemical structure is still both computationally intensive and requires a substantial amount of expertise. In the absence of accessible computation methods, screening for high performance dopants is a labour-intensive process.

Nevertheless, the results observed could still produce applications. The small change observed could be amplified by placing the initial reflection band near to the edge of the visible spectrum, which would then result in a shift from visible to transparent as the value of λ_{max} shifted into the near-IR region of the electromagnetic spectrum. This approach was considered, but due to the weaknesses highlighted above was not investigated further.

Additional factors also limit the potential of chemical dosimeters based on responsive chiral dopants. The most significant of these is the time required to generate a signal, which depends on the kinetics of the dopant-analyte reaction.

As shown in the GCMS studies in Section 5.4.1, the time required to reach equilibrium in the case of TADDOL-PH and acetone is 120 mins. Given that there exist mature technologies that are able to produce an accurate readout within seconds, this results in a weakened case for sensors based on responsive dopants in nematic matrices.

Despite this, several positives can be drawn from the previous work. From Section 5.4.4 it has been demonstrated that it is possible for sensors based on a change in β to discriminate between molecules sharing a functionality, which has not been previously shown. Likewise, the high helical twisting power of the TADDOL-PH complex reinforces the concept from Han et al. that complexes of small reactive molecules with chiral auxiliaries are a powerful method to bypass long synthetic processes to obtain dopants with high helical twisting powers.

Important lessons can be learned from these results about the general applicability of chemosensors based on responsive chiral dopants undergoing a chemical reaction with an analyte. The first, and main, of these is that they are unlikely to be able to compete with resistive or spectroscopic sensors, even when portability is taken into account. The long time required to produce a signal and the fact that time-dose curves allow for results to have multiple possible meanings make it difficult to imagine these sensors being used in any situation where responsiveness or unambiguous results are required. Additionally, given that small values of $\Delta\lambda_{max}$ are likely for most responsive dopants (See Section 4.2.1), applications that produce visually-discernible results are exceptional, and thus many such sensors would instead require laser-photodetector systems to assay.

Once these limitations are laid out, new applications can instead be sought that maximise the benefits of this technology, such as the portability, low cost and the ability to actively record chemical dose without the need for electrical power. One such application that we highly recommend for future researchers in this area is

that of smart packaging.

Smart packaging is a nascent field, and refers to the concept of adding utility to packaging beyond merely protecting the contents of the packaging. Currently, the technology in this field is limited, and usually consists of simple thermometers that can record if a certain temperature has been exceeded. Here, the disadvantages of responsive liquid crystalline chemosensors are either counteracted, and the benefits outlined above can reach their full potential.

The problems associated with long reaction times and multiple interpretations of a signal are no longer relevant, as transit provides sufficient time for any reaction to occur and the transit times are routinely recorded, limiting the possible response to a single time-dose curve. The problems associated with visual discernment are also limited, as it is possible and inexpensive to include a laser-photodetector system as part of a package handling process that is already largely automated.

One factor that has precluded the incorporation of more advanced sensor systems into packaging is cost. Given the large volume of packaging that is used globally, any such system must have a minimal cost, as well as being able to be incorporated into packaging manufacturing techniques, where speed is a significant factor. The solution processable nature of liquid crystalline sensors here is strongly advantageous, as they can be incorporated into existing reel-to-reel processing techniques.

Chapter 6

Optical monitoring of UV dose by the photochemical degradation of BINOL within a chiral nematic thin film

6.1 Introduction

As mentioned in Chapter 3, N*LCs have a long history of being investigated for their UV-sensitive properties, with the first references dating back to 1965 [Jones et al. (1965)]. Throughout this time, photo-addressable liquid crystalline systems have remained of interest, resulting in new technologies such as Ichimura's optical command surfaces [Ichimura et al. (1988)]. This interest is particularly noted for N* LCs, where the ability to create responsive, full-colour displays that require no power is highly attractive. As such, many UV responsive chiral nematic systems have been developed.

Of particular interest to us is the ability to create simple optical UV dosimeters.

UV dosimeters have myriad applications, but one notable application is in the field of solar safety. Studies have indicated that there is a direct link between lifetime incidence of sunburn and the risk of developing malignant cutaneous melanomata, both in childhood [Armstrong (1988)] and adulthood [Dennis et al. (2008)]. One key technology in addressing this is the creation of personal UV dosimeters which allow an individual to determine the total received UV dose and thereby take preventative measures to avoid sunburn occurring.

Dopants that possess a high β and are sensitive to UV light have already been explored, notably by Zhang and Schuster, who used the photoracemisation of 1,1'-bi(2-naphthol) derivatives in an attempt to create a bistable display that could switch between N* and compensated nematic phases on illumination [Zhang and Schuster (1992)]. Although their attempts to revert from the compensated nematic phase back to a chiral nematic phase by illumination with circularly polarised light were unsuccessful, they nevertheless demonstrated that it was possible to radically alter the structure of a N* LC containing 1,1'-bi(2-naphthol) derivatives using UV light.

Here we outline a system, based on the photochemical degradation of (R)-(+)-1,1'-bi(2-naphthol) (BINOL) which undergoes an irreversible photochemical reaction in the presence of UV light, resulting in a permanent shift in the value of λ_{max} . Our choice of dopant was informed by the well-known ability of BINOL and its derivatives to undergo photoracemisation, as has long been demonstrated [Irie et al. (1977)]. Although bridged BINOL derivatives are more likely to undergo photoracemisation, as well as possessing substantially higher values of β , one of the aims of this body of work was to create systems that are created solely using commercially available materials. As such, BINOL was chosen as the responsive dopant in this mixture.

As demonstrated in Chapter 4, it is possible to predict the shift in the value of

λ_{max} using Equation 6.1

$$\Delta\lambda_{max} = 1000\bar{n} \frac{x_i - x_f}{x_i x_f y z}, [x, y, z = \beta, e_e, c_w] \quad (6.1)$$

6.2 Experimental

6.2.1 UV and CD studies of BINOL under HI UV illumination

Solutions of BINOL in toluene were prepared and exposed to high-intensity UV light ($I = 132.02 \text{ mWcm}^{-2}$) with varied exposure times. The UV spectrum and Circular Dichroism (CD) measurements were captured for each sample.

6.2.2 N* LC thin films containing BINOL as a dopant

A solution containing 12% w/w of BINOL in E7 was prepared, with diethyl ether used as a cosolvent to encourage dissolution. Once the diethyl ether was removed by evaporation, the formulated LC mixture was used to fill a liquid crystal cell (20 μm gap, Instec) consisting of anti-parallel aligned ITO electrodes on glass. The UV/Vis/NIR transmission of the cell was measured, and from this the value of β was calculated.

6.2.3 Exposure of N* LC thin films containing BINOL to HI UV light

A cell was prepared as above and exposed to UV light from an Omnicure S2000 UV lamp using a 200W mercury vapor bulb, which produced an output of 0.5 Wcm^{-2} , measured using photodiode with a 253 nm filter. The principal lines of interest are at 253 and 296 nm. The UV/Vis/NIR transmission of the cell was recorded before and after exposure to UV light.

6.2.4 Dose effect and sensitivity of N* LC thin films containing BINOL

A set of cells were prepared as above and exposed to simulated sunlight (AM 1.5 solar simulator, $I = 15.2 \text{ mW/cm}^2$) for different exposure times. The total dose for each sample was calculated and compared to the λ_{max} recorded by UV/Vis/NIR photospectrometry.

From the above information the sensitivity and the predicted value of the dopant weight contribution, c can be determined. By comparing theoretical and experimental values of c the validity of the model developed in Chapter 4 can be determined.

6.2.5 Thermal cross-sensitivity

A set of cells were prepared as above and exposed to UV light (Omnicure S2000 UV lamp, $I = 0.5 \text{ W/cm}^2$) while heated to $50 \text{ }^\circ\text{C}$. The sensitivity was determined and compared to values obtained at different temperatures. All samples were measured at the same temperature in order to eliminate effects thermal expansion of the nematic host.

6.3 Results and Discussion

6.3.1 UV and CD studies of BINOL under HI UV illumination

The results obtained from circular dichroism spectroscopy (Figure 6.1) show a loss of enantiomeric excess resulting from progressive exposure to UV light, as would be expected from the racemisation of BINOL.

Figure 6.2 shows the UV/Vis spectrum of BINOL in toluene. If the reaction taking place is photoracemisation, then progressive UV illumination would have

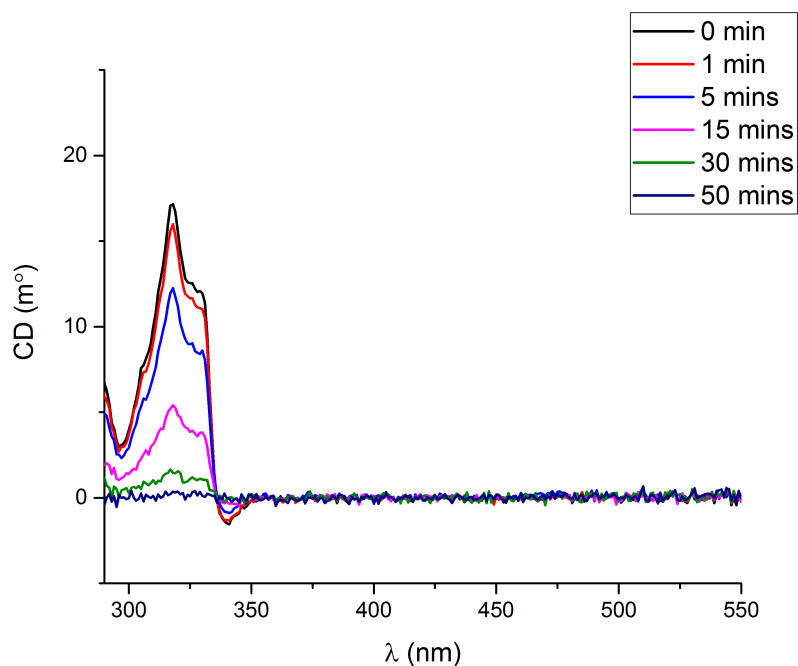


Figure 6.1: The CD measurements of solutions of BINOL in toluene after illumination with high intensity UV light ($I = 132.02 \text{ mWcm}^{-2}$). Sample was contained in a quartz cell with path length $l = 1 \text{ cm}$.

no impact on the intensity of the peak at 333 nm, given that the analyser beam is unpolarised.

As shown in Figure 6.3, progressive irradiation with UV light results in a decrease in the intensity of the peak at 333 nm, indicating that a photochemical reaction is occurring. As no change in the UV/Vis spectrum would be expected for photoracemisation, it is unlikely that this is the mechanism occurring.

Also notable in Figure 6.3 is that increasing irradiation results in increased scattering of the N* LC thin film at all wavelengths. This indicates an increase in the level of disorder present in the nematic host, possibly due to photochemical reactions occurring between the photochemical products and the nematic host. Samples not containing any chiral dopant did not display this behaviour, indicating

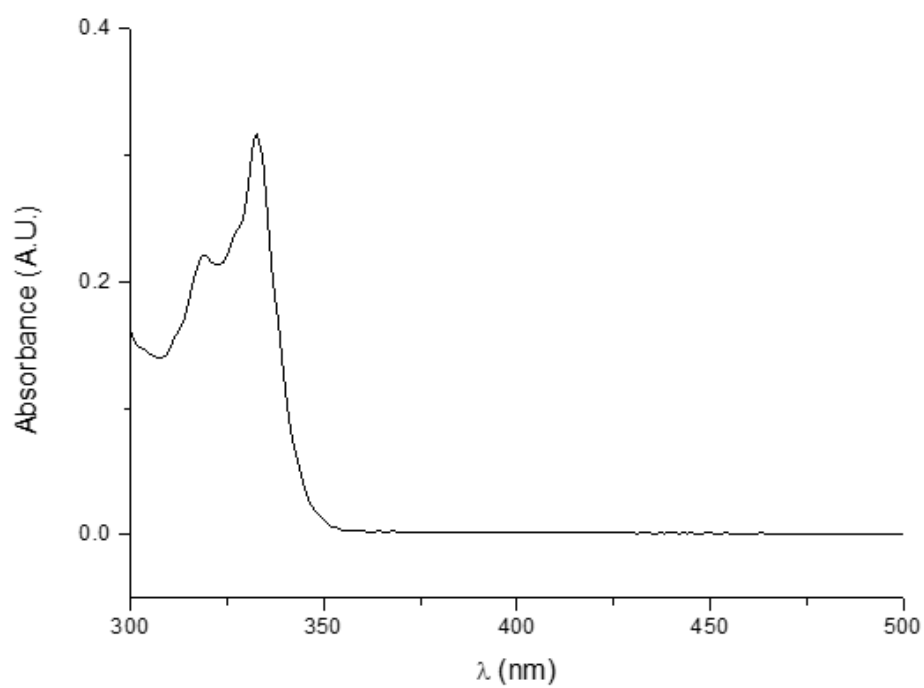


Figure 6.2: The UV/Vis absorption spectrum for a 5 wt% solution of (R)-(+)-1,1'-bi(2-naphthol) in toluene. Sample was contained in a quartz cell with path length $l = 1$ cm.

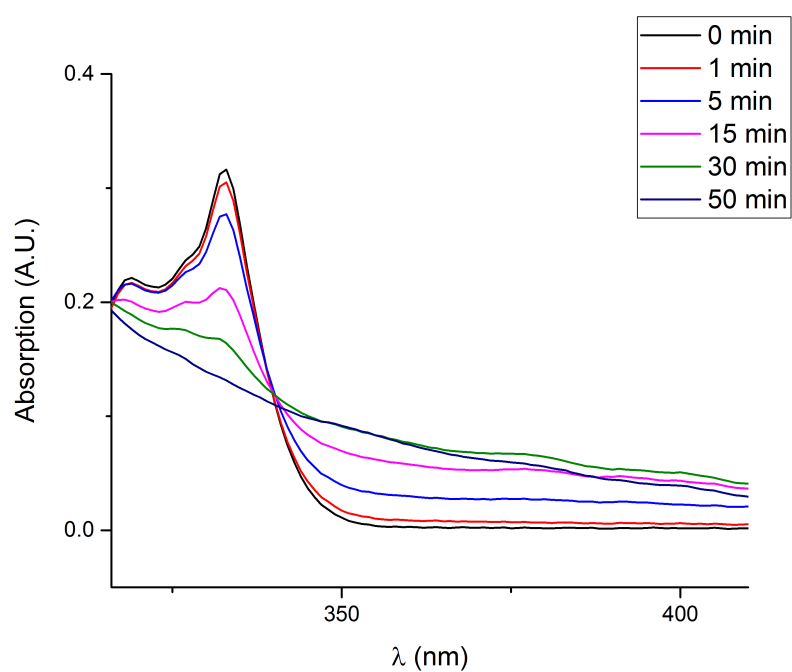


Figure 6.3: UV spectrum of BINOL following progressive irradiation with UV light ($I = 132.02 \text{ mWcm}^{-2}$). Sample was contained in a quartz cell with path length $l = 1 \text{ cm}$.

that photochemical degradation of the nematic host alone is not responsible.

The reduction in CD intensity remains significant however, as it shows a loss of chiral purity of the sample. This process can occur either through racemisation, or by the conversion of a chiral material to an optically inactive state. Given the UV/Vis spectra, it is likely that the mechanism involves the photodegradation of BINOL into achiral photochemical products.

6.3.2 N* LC thin films containing BINOL as a dopant

One feature commonly noted is the relative insolubility of BINOL in nematic hosts such as E7. This has led to significantly varying reports of the value of β . As such, it is important that the value of β be determined experimentally for each system, rather than relying on literature reported values.

6.3.3 Exposure of N* LC thin films containing BINOL to HI UV light

As can be seen in Figure 6.4, exposure of the cell to high intensity UV light resulted in two significant changes: the value of λ_{max} increased by 490 nm, and the transmission intensity decreased slightly. These are both changes that would be predicted for a system based on a chiral \rightarrow achiral transformation. Similar results were also obtained when the BINOL/LC mixture was exposed to direct sunlight for longer times (Figure 6.5).

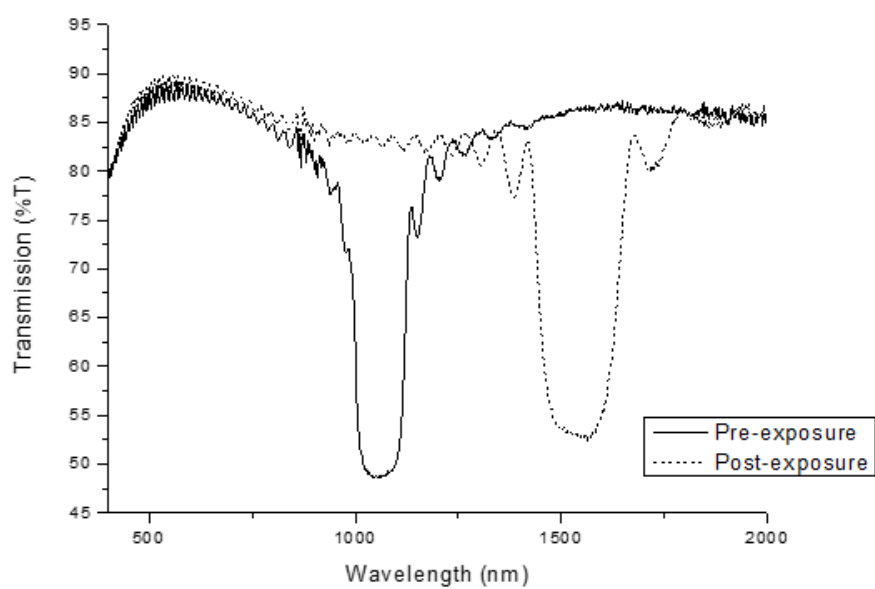


Figure 6.4: The UV/Vis/NIR transmission of 20 μm cells containing 7.5 wt% of BINOL in E7 before and after exposure to high intensity UV light ($I = 0.5 \text{ mWcm}^{-2}$).

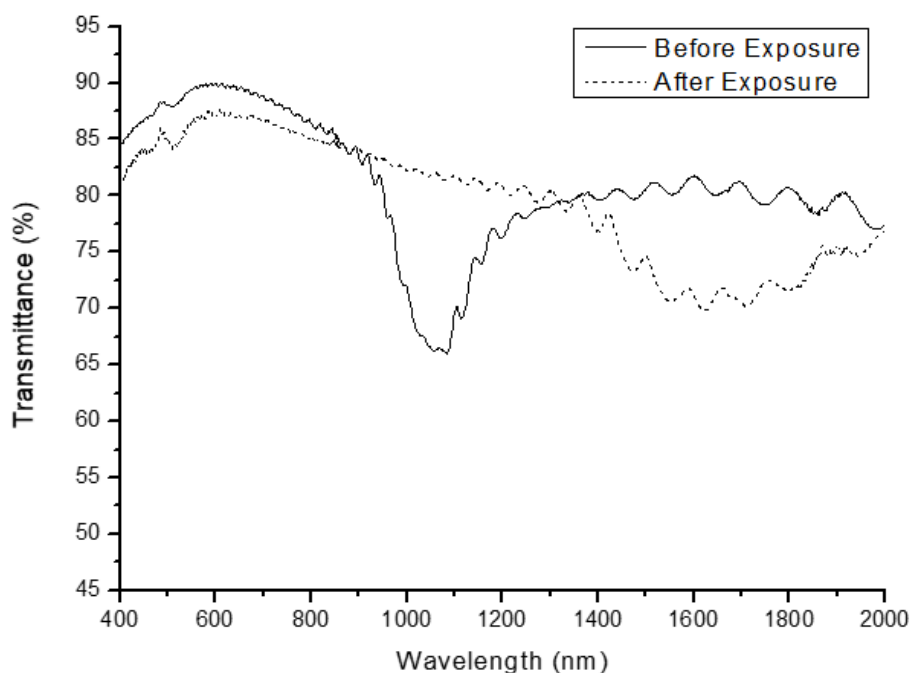


Figure 6.5: The reflection band of a cell containing 12% (R)-(+)-1,1'-bi(2-naphthol) in E7 before and after being exposed to unpolarized direct sunlight (London, 28th June 2016, 11:00 am) for 28 min. $I = 6.67 \text{ mWcm}^{-2}\text{s}^{-1}$. The decreased intensity arises from the use of a LC cell with a small gap ($6.8 \mu\text{m}$), which limits the number of helical twists present.

6.3.4 Dose effect and sensitivity of N* LC thin films containing BINOL

In order to determine the efficacy of a dosimeter, a dose-response curve must be constructed. Ideally, a dosimeter will display a linear dose response, which allows for simple quantification of the device sensitivity, but devices can exhibit a non-linear dose response behaviour.

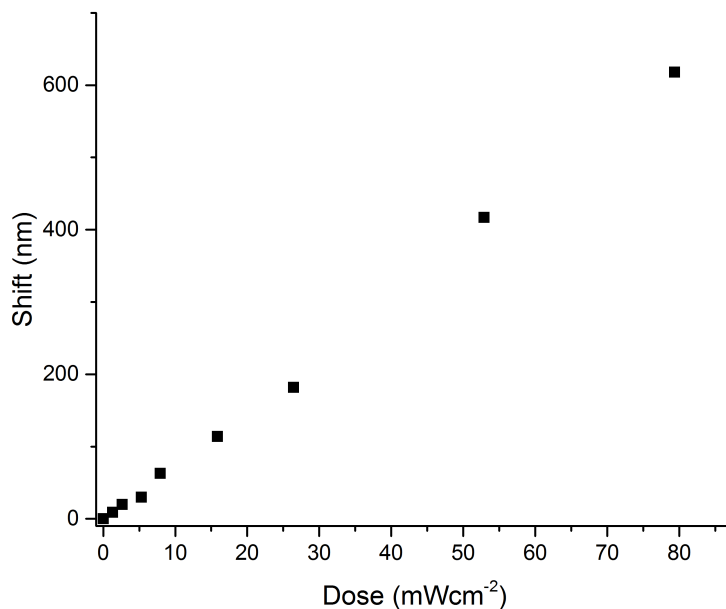


Figure 6.6: The change in λ_{max} ($\Delta\lambda$) as a function of UV dose. UVI = 15.2 mWcm⁻².

As can be seen from Figure 6.6, under the conditions tested N* LC thin films containing BINOL exhibit linear dose response ($R^2 = 0.9983$). Although an exponential relationship is expected according to the predictions made in Chapter 4, the non-linear behaviour would only be noticeable at high levels of conversion. This is discussed in more detail in the aforementioned chapter.

A secondary property of a dosimeter is that the signal does not revert under dark conditions. Samples were tested periodically, but no change in the value of λ_{max} was observed.

From Figure 6.6, the sensitivity of these sensors can be determined to be 121.0 nm/Jcm⁻². Despite previous investigations of dosimeters based on N* LC thin films, sensitivity is typically not reported, so there is little to compare this data to.

In order to determine if this is the correct mechanism, it is necessary to cal-

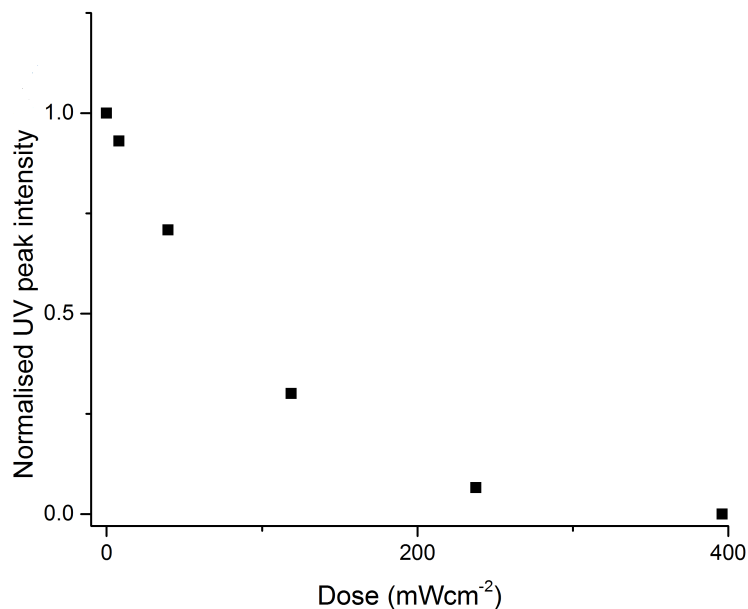


Figure 6.7: A plot of normalised UV peak intensity at 333 nm against dose.

calculate the rate of photodegradation, and from this determine how well theoretical predictions match the experimental observations. In this simplified case study, the contribution from the scattering is ignored, even though Figure 5.3 indicates that it could have a substantial impact. The rate of photodegradation can be determined by plotting the normalised UV peak intensity (N_{UV}) against UV dose (D) (Figure 6.7). Performing exponential regression gives the relationship expressed in Equation 6.2 ($R^2 = 0.9962$).

$$N_{UV} = 1.0945e^{-0.012D} \quad (6.2)$$

Given that the proposed photoproducts formed are achiral, this can be represented as a percentage decrease in the amount of chiral dopant present. This can be represented by using the normalised UV peak intensity as a multiplier for the

value of c in Equation 6.1, which takes the form outlined in Equation 6.3.

As mentioned in the discussion of Figure 6.3, increasing irradiation caused a scattering effect on the films containing the BINOL dopant. This effect is not considered when normalising the UV intensities, but could be accommodated by considering the normalised intensity to be the difference between the peak and the baseline including the impact of scattering. Such analysis will be included in future discussions of this data, but are not included here for the sake of simplicity.

$$\Delta\lambda_{max} = 1000\bar{n} \frac{c_i - c_f}{c_i c_f \beta e_e} \quad (6.3)$$

This can then be used to produce a predicted value of c for a given UV dose, as shown in Figure 6.8. From this, the relationship between UV dose and predicted c can be determined (Equation 6.4).

$$c_{theo} = c_i e^{-0.011D} \quad (6.4)$$

By combining Equations 6.3 and 6.4, it is then possible to predict the value of $\Delta\lambda_{max}$ for a given UV dose. By combining this with the experimental data, it is then possible to determine the accuracy of the model developed (Figure 6.9).

Figure 6.9 shows excellent agreement between the theoretical and experimental data, indicating that the formation of achiral photoproducts is a likely source of the change in the value of $\Delta\lambda_{max}$. This also demonstrates the predictive power of the model developed in Chapter 4.

6.3.5 Thermal cross-sensitivity

As mentioned in Chapter 3, one common problem with sensors based on N* LCs is the presence of substantial cross-sensitivities. By containing the dosimeter within a sealed cell we can eliminate the cross-sensitivity arising from the absorp-

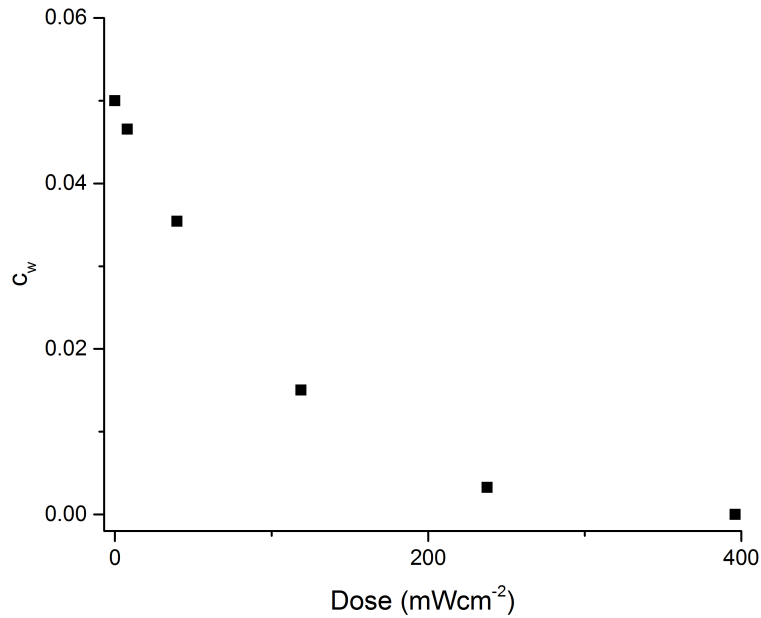


Figure 6.8: Predicted c plotted against UV dose.

tion of volatile organic compounds. A second major source of cross-sensitivity which cannot be avoided is thermal cross sensitivity.

This cross-sensitivity manifests itself in two ways:

1. Cross sensitivity arising from the thermal expansion of the LC host, which can change the value of λ_{max}
2. Cross-sensitivity arising from the rate of the chemical reaction being sensitive to temperature, in line with the Arrhenius equation

$$k = Ae^{\frac{E_a}{RT}} \quad (6.5)$$

Although the first of these can be minimised by using LC hosts with low thermal expansion coefficients, the second is not easily avoided, and must instead

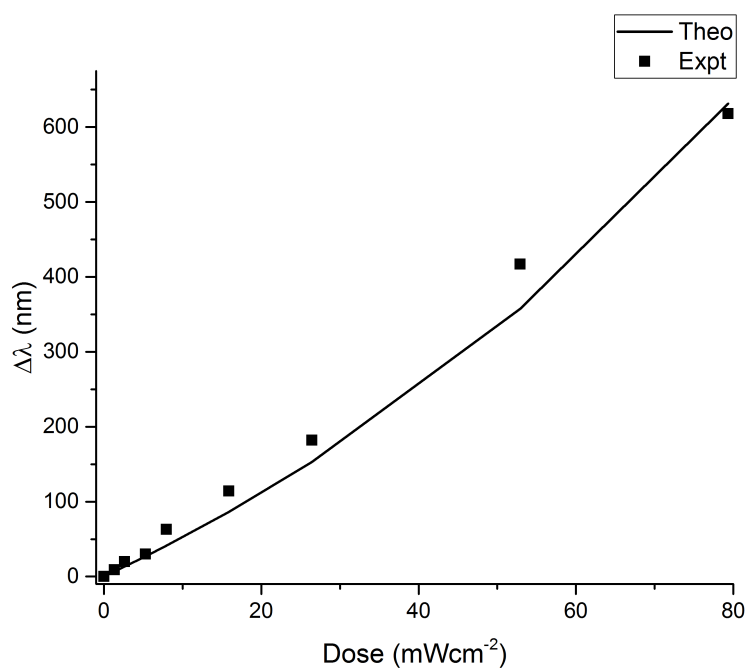


Figure 6.9: Comparison of the experimental and theoretical values of $\Delta\lambda_{max}$ for BINOL in E7 as a function of UV dose.

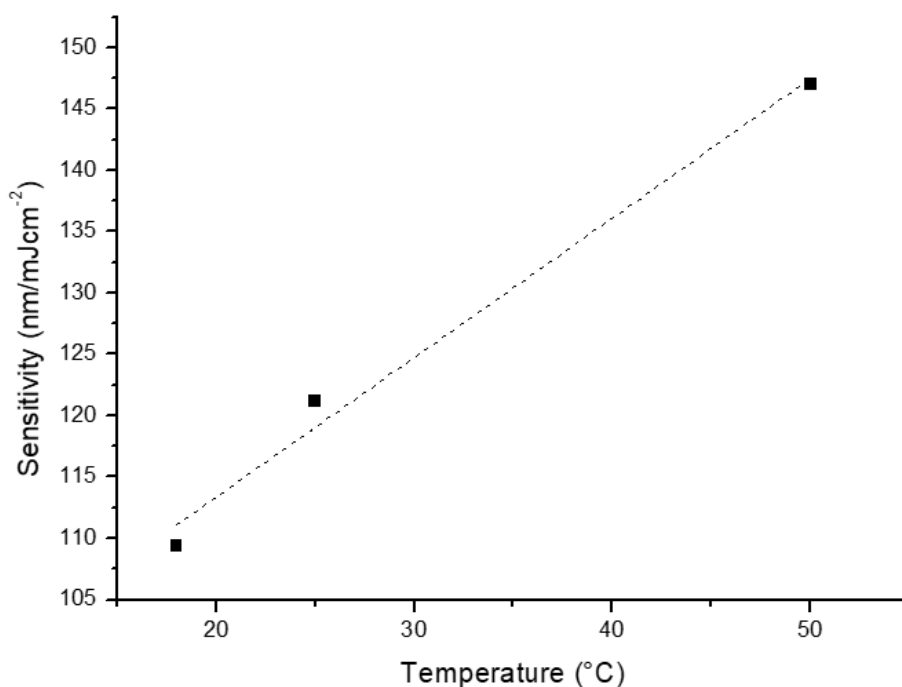


Figure 6.10: The sensitivity of the BINOL/LC mixture to UV light at different temperatures. This also includes results from different UV sources, demonstrating that the dosimeters are source agnostic.

be accounted for by calibration.

As can be seen in Figure 6.10, changing the temperature at the time of exposure had a significant, but predictable, effect on the sensitivity of the device. In particular, increasing the temperature from 18 °C to 50 °C results in an increase of sensitivity from 109 nm/mJcm⁻² to 147 nm/mJcm⁻². This figure represent a 34% increase in sensitivity over a range of 32 °C.

6.4 Conclusion

We have demonstrated that predictable UV dosimeters can be constructed by incorporating a photo-sensitive chiral dopant within a nematic liquid crystalline host. Although initial attempts to probe photo-racemisation as an underlying

mechanism were unsuccessful, a new mechanism was identified in the formation of an achiral photoproduct. As such, this system is an example of a dopant based on a chiral \rightarrow achiral transformation, which was identified in Chapter 4 as another highly sensitive mechanism.

Attempts were also made to access the photoracemisation of BINOL as a possible sensing mechanism. This included investigations on the impact of lower UV doses, as well as the inclusion of a base, as outlined in Solntsev et al. (2009). These investigations were unsuccessful: in the latter case the inclusion of even small amounts of inorganic bases resulted in disruption of the LC film, resulting from crystallisation of the base. Attempts to study the impact of organic bases or lower UV doses were abandoned due to low performance and positive results from other avenues of investigation. We believe that these might still successfully lead to methods of sensing based on photoracemisation, and recommend them as potential future targets.

As noted above, the limited solubility and low β of BINOL gives rise to the poor optical properties of these mixtures, notably the high value of λ_{max} . By using the bridged binaphthyl derivatives developed by Zhang et al. this could easily be adapted to produce sensors that operate within the visible spectrum, and as such could operate as simple colourimetric dosimeters. This is an area of work that is highly recommended for future investigation, as these dopants are synthetically accessible.

Chapter 7

Optical monitoring of UV dose by the photoisomerisation of a menthone-based dopant in a chiral nematic thin film

7.1 Introduction

Work in this section was produced in collaboration with Dr. H. Khandewal and Prof. A. Schenning, TUE.

As mentioned in Chapter 4, photodegradation has significant disadvantages over systems based on photoisomerisation. However, the reversible nature of most isomerisation reactions limits the applicability of this technology in situations where sensors are exposed to ‘broad-band’ light sources such as sunlight, where the forward and reverse reactions are triggered simultaneously. This results in the rapid establishment of an equilibrium state where further measurements cannot be made, and thereby limits the effective range of UV dose over which the sensor is

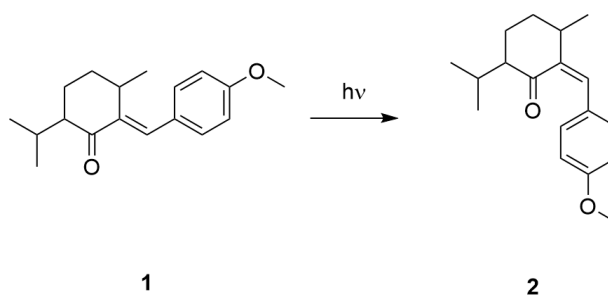


Figure 7.1: The UV-induced photo-isomerisation of a functionalised menthone derivative, **1**, received from Philips.

usable.

This equilibrium state can be avoided by the use of an irreversible isomerisation reaction. The existing literature in this area focuses on thermally irreversible photo-isomerisation reactions [Rameshbabu et al. (2011)], which avoid one technical limitation of devices based on reversible photo-isomerisable dopants. Here, we will instead investigate the use of a photonically irreversible photoisomerisation reaction. As far as we are aware, no attempts at making a irreversible photo-isomerisable dopant for sensing applications have been made.

Our system is based on the photo-isomerisation of a menthol derivative, **1**, which was received from Koninklijke Philips NV (the Netherlands). On exposure to UV light, this dopant undergoes an irreversible photo-isomerisation from the *E*-isomer to the *Z*-isomer. (Figure 7.1) In doing so, it undergoes a transition from a calamitic (aspect ratio = 1:2.37, Figure 7.2a) to a *pseudo*-spherical shape (aspect ratio 1:1.5, Figure 7.2b), with an expected decrease in the value of β .

This dopant is currently being investigated as a component in creating a tunable IR reflector by Khandelwal *et al.*, where the β of **1** and **2** were determined to be $25 \mu\text{m}^{-1}$ and $2 \mu\text{m}^{-1}$, respectively.

We anticipate that the irreversible nature of the photoisomerisation, which we will demonstrate below, is a key step in producing commercially viable N*

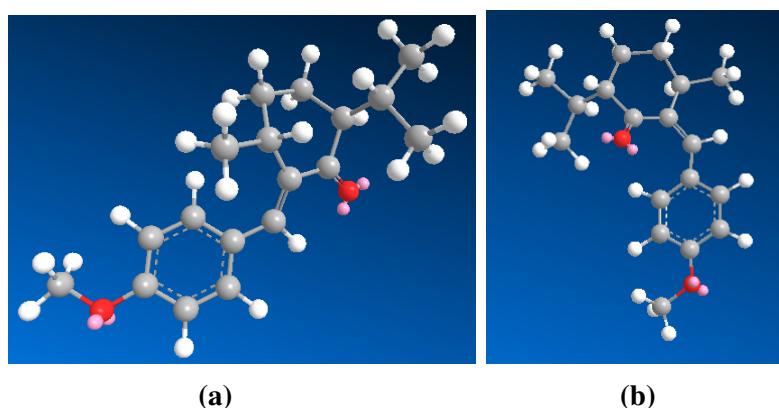


Figure 7.2: The (*E*) and (*Z*) isomers of **1**. Geometry optimised by MM2 method.

LC dosimeters. For a system based on photoisomerisation, such as the optical command surfaces pioneered by Ichimura et al. (1988) to operate as a dosimeter would require the inclusion of a UV filter, so that only the forward reaction is triggered. The inclusion of this filter would significantly increase the complexity, and therefore the cost of such devices.

7.2 Experimental

7.2.1 UV response of dopant **1**

1 was received from Koninklijke Philips NV (the Netherlands) and used without further purification.

Solutions of **1** in toluene were prepared, and UV-vis spectra were taken while the sample was irradiated for different times using UV light ($\lambda = 365$ nm).

7.2.2 Response of N* LC thin films containing **1** to UV light

It is necessary to determine if the photoisomerisation above does result in a change in λ_{max} for a N*LC.

Two LC cells were prepared as in 6.2.2. One of these cells was exposed to UV light (Omniculture S2000, UVI = 56.6 mWcm⁻²) for 5 sec.

7.2.3 UV sensitivity of 1

In order to determine the sensitivity of these devices, LC cells were prepared as in 7.2.2 and then exposed to sunlight as in 7.2.2 for varying times.

In order to show that these devices are effective at a range of UV intensities, a second set of cells were prepared and exposed to UV light (UV intensity = 6.67 mWcm⁻²)

7.2.4 Cross sensitivity

In order to measure the impact of changes in temperature on the sensitivity of these devices, cells were prepared as in 7.2.2 and exposed to artificial sunlight (AM1.5 solar simulator) at a range of temperatures.

7.2.5 Tuning sensitivity

LC mixtures containing 0.53 wt% of UV absorbing compound Tinuvin 328 (Figure 7.3) (Source BASF SE, Ludwigshafen, used without further purification) were prepared as above. UV/Vis spectra before and after illumination (UVI = 10.14 mWcm⁻²) for a variety of exposure times were conducted. A second mixture containing 1 wt% of Tinuvin 328 was prepared, and UV/Vis spectra captured.

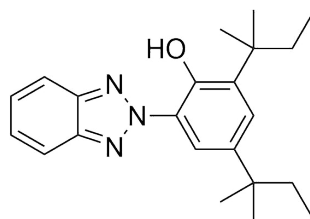


Figure 7.3: The structure of the UV absorbing compound Tinuvin 328.

7.3 Results and discussion

7.3.1 UV response of dopant 1

Figure 7.4 shows the UV/Vis spectrum of **1** in toluene. By illumination with UV light at $\lambda = 365$ nm, it is possible to induce the photoisomerisation, as demonstrated in Figure 7.5.

The irreversible nature of this transformation is the subject of a future work by H. Khandelwal [Personal Communication, 2017]. As such it cannot be discussed here.

7.3.2 Response of N*LC thin films containing **1** to UV light

By comparing the structures of **1** and **2**, it is possible to see the origin of this change in β comes from a change in the molecular geometry of the dopant (Figures 7.2a and 7.2b). The dopant moves from a calamitic state in **1** to a *pseudo*-spherical shape in **2**, which would have a weaker interaction with the calamitic mesogens in LC6553. LC6553 was chosen as the nematic host on advisement of H. Khandelwal (personal communication, 2016) as a suitable nematic host for **1**.

As mentioned in Chapter 4, highly sensitive sensors can only be created when either β_i or β_f is close to zero. Due to the decrease in β observed in this system, any UV dosimeter is likely to express very high sensitivity compared to the system discussed in Chapter 6.

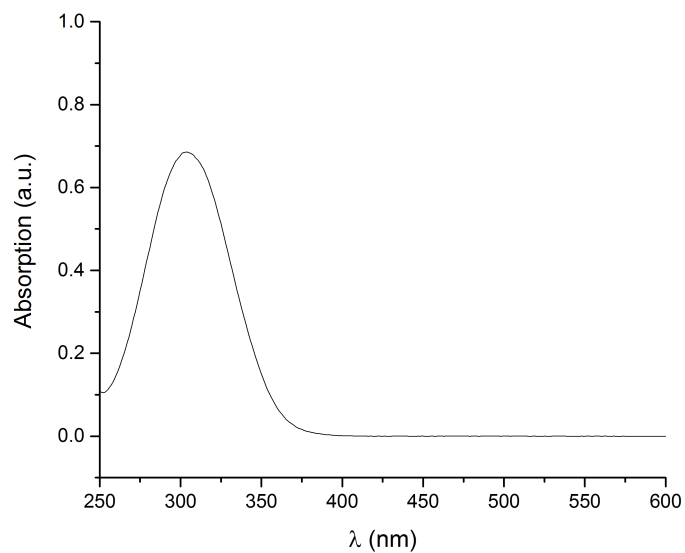


Figure 7.4: UV/Vis absorption of a 5% solution of **1** in toluene. Sample was contained in a quartz cell with path length $l = 1$ cm.

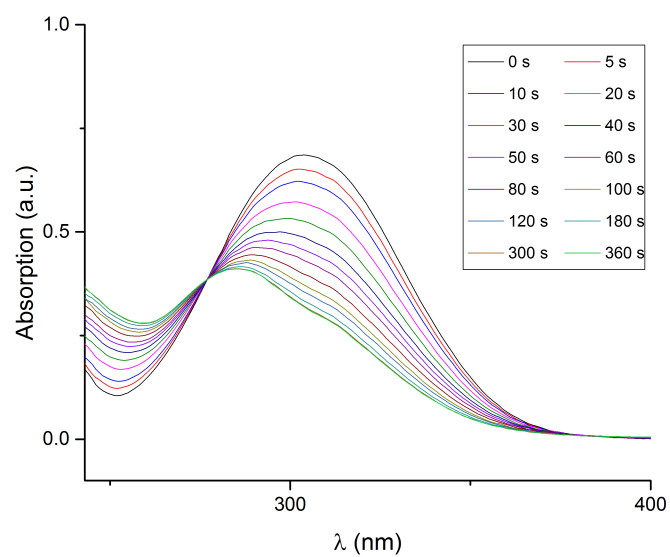


Figure 7.5: The UV/Vis spectra of solutions of **1** following progressive illumination.

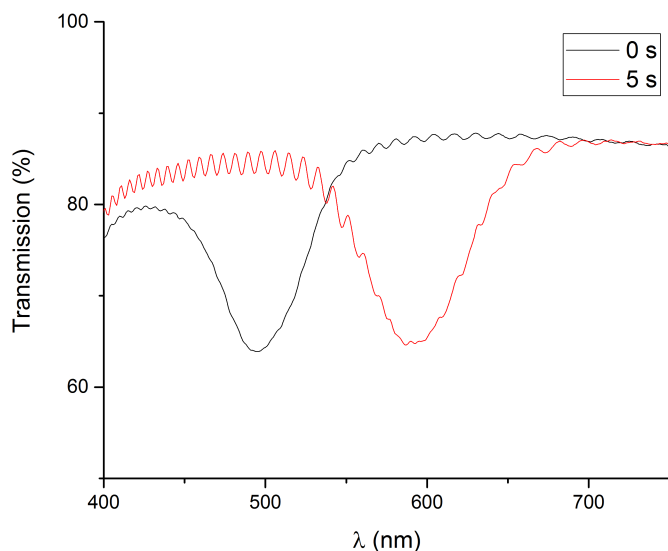


Figure 7.6: The UV/Vis spectra of **1** in LC6553 ($c_w = 0.101$) before and after exposure of UV light for 5 seconds (UVI = 56.6 mWcm^{-2}).

7.3.3 UV sensitivity of **1**

As shown in Figure 7.6, exposing films containing **1** to UV light results in an increase in the value of λ_{max} as predicted above. In order to determine the sensitivity, it is first necessary to determine the transparency of the system at the wavelength of interest. This can be measured by taking a UV/Vis spectrum of a cell not containing the responsive dopant (Figure 7.7) and using this as a background.

From this, we can construct graphs for both the exposure time and dose response of these sensors (Figure 7.8).

The sensitivity of the dopant-LC system can therefore be determined to be 2847 nm/Jcm^{-2} , an increase of more than 2300% compared to the systems discussed in Chapter 6. This is in line with expectations from Chapter 4.

A second important requirement for dosimeters is that the behaviour is truly dosimetric, and therefore source agnostic. By exposing samples to a UV source

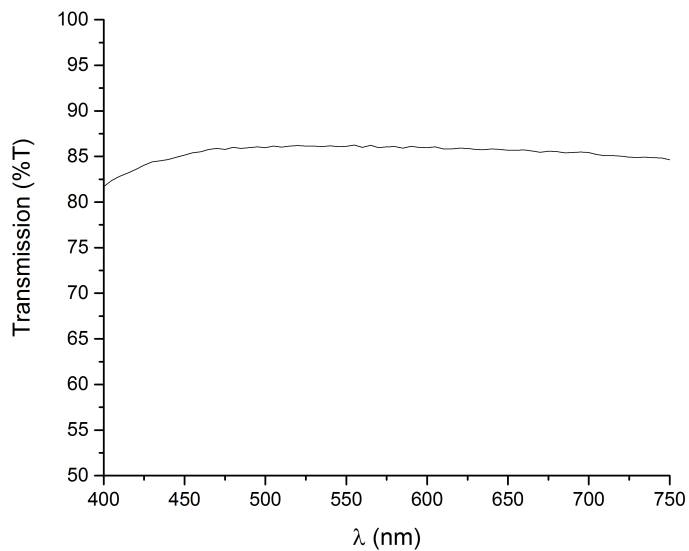


Figure 7.7: The UV/Vis spectrum of LC6553 in a 7.7 μm gap cell containing anti-parallel ITO electrodes.

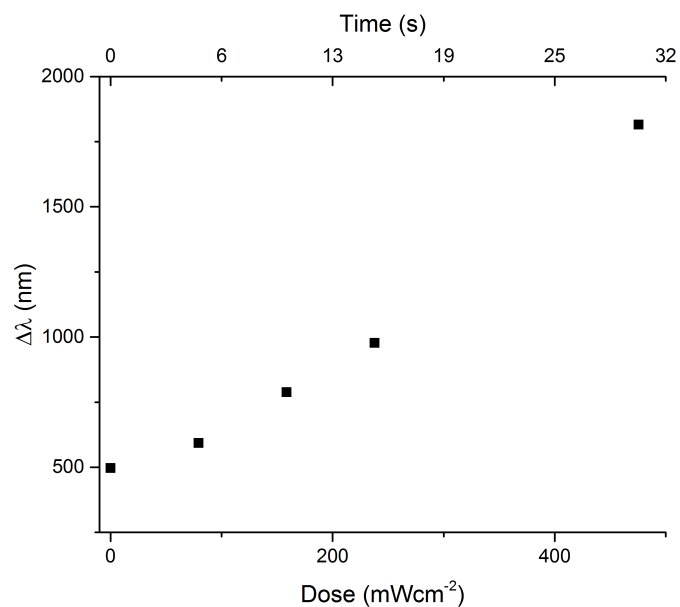


Figure 7.8: The change in λ_{max} for a given UV dose (bottom axis) or exposure time (top axis).

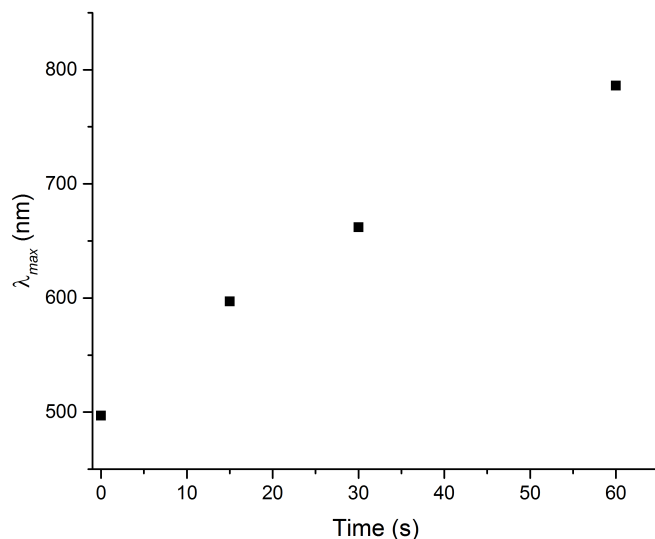


Figure 7.9: The changes in the value of λ_{max} as a function of exposure time for samples containing **1** exposed to simulated sunlight (UVI = 6.67 mW/cm²).

with a different intensity (Figure 7.9), it is then possible to compare the dose response for the different sources (Figure 7.10). From this, it can be seen that a significant change in UVI has a minimal impact on the overall sensitivity of the device, and therefore this dosimetric platform is suitable for use in a range of UV conditions.

7.3.4 Cross sensitivity

As mentioned previously, the encapsulation of these systems in LC cells means that only thermal cross sensitivity needs to be considered. While this does increase manufacturing complexity compared to naked films, the fragility of the LC mesophase means that encapsulation is preferable from the viewpoint of mechanical stability, and thus is an acceptable cost in the case of these devices.

Figure 7.11 shows the impact of increasing the temperature on the sensitivity

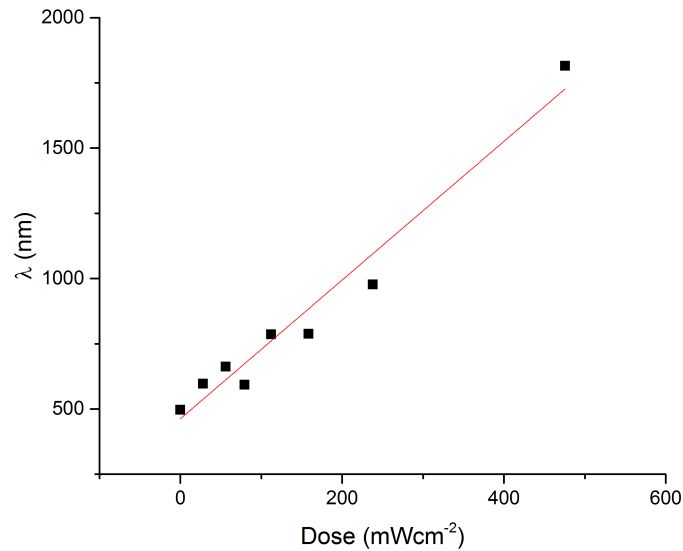


Figure 7.10: The combined dose response for the two above experiments, with different UV intensities.

of these devices. As is predicted based on the Arrhenius reaction, increasing the temperature increases the rate of the reaction, and hence the sensitivity. As the sensitivity increases significantly based on the temperature of the dosimeter, it would be necessary to control for temperature when determining the total UV dose.

7.3.5 Tuning sensitivity

A common challenge facing personal UV dosimeters is the need to produce models with differing sensitivities. This is necessary as different skin types have different responses to UV light, resulting in a variety of MEDs, as opposed to a single universal value. The inclusion of a UV absorber such as Tinuvin 328 allows for facile control over sensitivity. Figure 7.12 indicates that even in the presence of Tinuvin 328, illumination with UV light results in a progressive red-shifting of

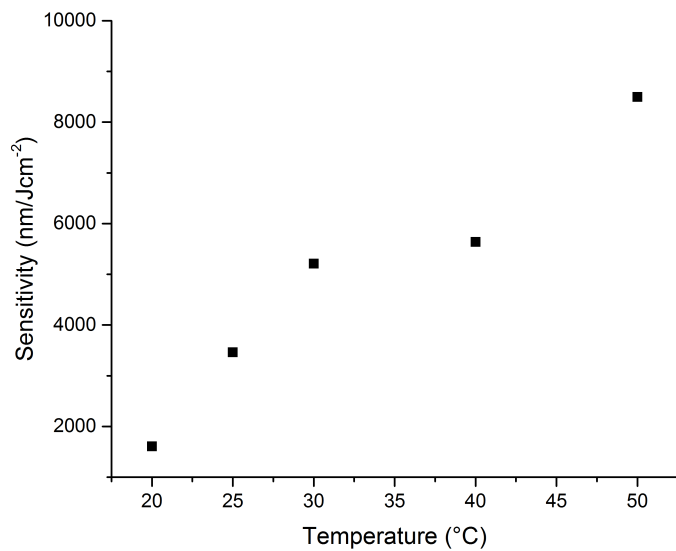


Figure 7.11: The impact of temperature on sensitivity. All samples exposed to simulated sunlight ($UVI = 6.67 \text{ mJcm}^{-2}$) for 15 seconds at a controlled temperature.

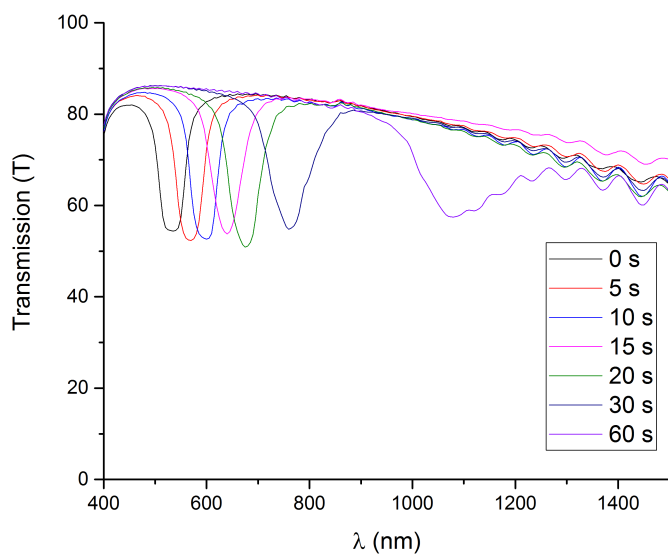


Figure 7.12: The UV/Vis spectra of a mixture containing 0.53 wt% of Tinuvin 328 as a UV absorber. $I = 10.14 \text{ mWcm}^{-2}$.

Tinuvin 328 concentration (wt%)	Sensitivity (nm/Jcm ⁻²)
0	2846
0.53	1257
1.0	993.1

Table 7.1: The effect of Tinuvin 328 concentration on the sensitivity of the dosimeter.

the reflection maximum (λ_{max}).

The overall effect of Tinuvin 328 on sensitivity is displayed in Table 7.1. This clearly demonstrates that the sensitivity of these devices can be tuned for a given value by the inclusion of UV absorbers directly into the N*LC material. Although theoretically this can also be simply controlled by selecting the UV absorptivity of the encapsulating material, the ability to produce dosimeters is highly desirable when considering the response of different skin types of UV radiation, which is a significant factor in avoiding sunburn [Sayre et al. (1981)].

As mentioned in Chapter 6, a dosimeter must not undergo a reversible change when not exposed to the analyte being measured. As before, no change in the value of λ_{max} was observed for sample with and without Tinuvin 328 stored away from UV sources.

7.4 Conclusion

Here we have demonstrated a highly efficient UV dosimeter that produces a clear colourimetric signal without requiring access to electrical power. Photoisomerisation is shown to be a highly efficient method of monitoring exposure to analytes in the cases where there is a significant reduction in β , with one value of β being close to zero.

We also have shown the applicability of this technology to 'broad band' UV sources, where photoisomerisation would not normally be considered feasible.

This is a major step forward in producing commercially viable UV dosimeters based on responsive N* LC thin films, as it significantly lowers the complexity, and therefore price of the assembled devices.

Although significant temperature sensitivity was observed, encapsulation has proven again as an effective method of removing sources of cross-sensitivity. Thermal cross-sensitivity can also be accounted for, either through the use of calibration curves provided with the device, or by the creation of a companion 'app' that is able to access temperature history and correctly determine the received UV dose.

We are now exploring commercial applications of this technology.

Chapter 8

Conclusions & future work

8.1 Summary of main points

Below we will give some of the issues encountered over the course of this project, as well as some potential solutions. This includes a brief overview of some of the work that was undertaken, but did not yield results significant enough to warrant inclusion in the main body of the work.

In summary, we have successfully developed and demonstrated a model for predicting the efficacy of a given dopant-analyte system. This model has been shown to be effective at predicting the behaviour of a range of sensors for a variety of analytes, giving it real utility when choosing what systems warrant further investigation.

Afterwards, we give two examples of systems that we believe are suitable starting systems for further investigation. These are based on the conclusions drawn in Section 8.2. These are systems that were suggested as having significant potential, but that did not fit within the framework of using only commercially available compounds that we imposed on this work.

8.2 Problems and recommendations

There remain significant hurdles in the path of commercialisation of these LC based sensory systems, which will have to be addressed in future research if this technology is to gain significant ‘real-world’ applications. We enumerate the major objections below, along with some possible solutions to be explored.

Some of these hurdles were known and highlighted in the introduction, namely the propensity of these sensors to having significant problems with cross-sensitivity. Some are newly highlighted as a result of the current work carried out, such as the problem of significant reaction times leading to difficulties in determining the accuracy of a device. All of these problems must be addressed.

8.2.1 Reaction times

As demonstrated in Chapter 5, sensors for chemical analytes require significant reaction times, depending on the solubility of the analyte in the matrix. The change of solvent from a liquid to a liquid crystal may also adversely affect the rate of the reaction, due to the significantly increased viscosity of the matrix. This effect has been demonstrated for other reactions [Kyushiki and Ikai (1990)], although not explicitly for liquid crystals.

In addition to high resolution times being generally unfavourable, these increased reaction times lead to two significant problems:

- Short duration, high-intensity signals may not accurately be reflected in the overall output of the device. This severely limits the dosimetric accuracy of these devices, as a series of short, high-intensity doses may result in an artificially low reading.
- Applications where rapid throughput is desirable, such as diagnostics, are

far better served by other technologies, limiting these sensors to fields where resolution time is not important.

Increased reaction times also significantly increase the impact of cross-sensitivity to temperature, although this is discussed in more detail in Section 8.2.2.

There are two ways in which the problem of significant reaction time can be addressed:

- Increasing the rate of reaction by heating the sensor. Heating is well known to increase the rate of reaction, and many reactions are carried out at elevated temperatures. Although effective, this solution is not ideal, due to a number of factors:
 - The narrow temperature range associated with the N* LC phase precludes significant heating, as does the relative volatility of the nematic host used. This impact could be minimised by choosing LC hosts that have large ‘nematic windows’, the range of temperatures over which the nematic phase is exhibited.
 - Small molecule analytes, such as acetone, are usually volatile, and thus heating above a certain point could lower the concentration of analyte within the LC host, leading to lower readings.
 - Utilising Joule heating in order to carry out the analysis at raised temperatures significantly increases the complexity of the device, as well as removing the independence from electrical power.

As can be seen from the above, changing the temperature at which the analysis is carried out is complex, with multiple, possibly conflicting effects on the performance of the device. While a possible resolution to the problem

of long reaction times, it could equally lead to no improvement, or a deterioration in the performance of a device.

- Utilising rapid ‘click’-style reactions as the basis of the analyte-dopant reaction. This is discussed in more detail in Section 8.3.1, but it must be noted that it significantly reduces the range of analytes which can be detected.

In general, we would rate reaction times as one of the most significant challenges that must be overcome by future investigation into the area of chemical dosimeters based on the N* LC thin film platform, alongside the issues of chemical and thermal cross-sensitivity.

8.2.2 Cross-sensitivity

From the outset, the problem of cross-sensitivity was identified as a significant hurdle that must be addressed, and as the largest factor preventing the commercialisation of these devices. Cross-sensitivity can arise from a number of sources, each of which requires a different approach to eliminating it as a source of error. The main sources of cross-sensitivity affecting the devices in this work are given below, along with potential methods of minimising their impact. It is worth noting that some sources of cross-sensitivity can never truly be eliminated.

Thermal Sensitivity to temperature, or thermal sensitivity, has been a significant factor in a wide range of LC technologies. With regards to the devices discussed in this work, there are two primary ways in which the cross-sensitivity to temperature can be expressed:

- Thermal expansion of the nematic host. The change in the value of λ_{max} in response to heating or cooling is well-known, having first been observed

prior to the discovery of liquid crystals by Reinitzer in 1888. As the nematic host expands on heating, so too does the value of p , resulting in a red-shifting of the value of λ_{max} . It is also possible to blue shift at higher temperatures. This effect is unavoidable, although it can be minimised by choosing nematic hosts with a low coefficient of thermal expansion. Similarly, calibrating the end reading to take account of the ambient temperature can remove the impact of this.

- The effect of temperature on the rate of reaction. This is likely the more significant of the two effects. As mentioned in Section 8.2.1, increasing the temperature usually has the impact of increasing the rate of reaction, and thereby decreasing the amount of time required to reach a certain concentration of product. This temperature sensitivity is expressed in the Arrhenius equation, which defines the rate constant, k , for a given reaction:

$$k = Ae^{-\frac{E_A}{RT}} \quad (8.1)$$

In cases where there is significant variations in ambient temperature, common outside of laboratory environments, this can result in the end result not accurately reflecting the received dose, with the dose measured while the ambient temperature is higher being over-represented compared to the dose received at lower temperatures.

The variation in temperature can be partially accounted for by retaining a history of the ambient temperature, in cases where the signal intensity is unlikely to vary significantly. In cases where both the signal and ambient temperature are likely to vary substantially, it may not be possible to determine the total dose accurately, in which case the device has failed in its primary aim. These systems are therefore limited to applications where

changes in signal intensity or temperature are likely to be minimal.

In this work, we sought to determine the impact of temperature on these systems for the two UV dosimeters. In both cases, it was found that over a temperature range consistent with possible changes in external daytime temperature the changes in sensitivity, though significant at ~30%, were unlikely to render a reading completely unusable for the purpose of personal UV dosimetry.

Chemical Cross-sensitivity to chemical substances comes from two possible sources:

- Inclusion of volatile, non-responsive molecules into the nematic matrix. This results in the swelling of the nematic host as the concentration of the interloping molecules increase. At a high enough concentration, the disruption to the LC order is so severe that it cannot be recovered by removing the source of the interloping molecules. At even higher concentrations, it will result in the effective dissolution of the LC host.

This is traditionally more of a problem in systems based on real-time sensing, as time-integrating sensors can be removed from the source of interloping molecules when a reading is made. It can nevertheless be problematic if the sensor cannot be removed from its immediate environment for a measurement to be made, as is the case when the sensor is integrated into some larger unit. In this latter case, briefly heating the sensor prior to recording a measurement may decrease the amount of interloper molecules present, leading to a more accurate reading.

- Chemical reactions occurring between the dopant and non-analyte molecules, including the LC host. This was demonstrated in Chapter 5 by

the sensitivity of the sensor to a variety of non-ketones, including the alcohol analogue of acetone, propan-2-ol. While the sensitivity to propan-2-ol was markedly lower than that of acetone, it is possible that an atmosphere rich in propan-2-ol could be misdiagnosed as one containing small amounts of acetone.

This latter source of error can be reduced by the utilisation of highly specific reactions, such as the ‘click’-type reactions mentioned in Section 8.2.1. This idea is explored more fully in Section 8.3.1.

In the case of the two UV dosimeters developed in this work, chemical cross-sensitivity due to the absorption of non-analyte molecules was removed by the encapsulation of the dosimeter within a chemically impermeable and inert LC cell. This is not possible when the analyte in question must be absorbed into the N* LC matrix, and in these cases again attention must be paid to the specificity of the reaction in question. In Section 4.2.2 we outlined a possible sensing mechanism which would allow for the truly specific monitoring of a given analyte. This is discussed in more detail in Section 8.3.2.

Mechanical Fragility is inherent to liquid crystalline systems, and indeed these sensors cannot be constructed except by exploiting that fragility. This fragility can also have a negative effect, as mechanical disruption of the film can result in a change in the pitch, and therefore in λ_{max} . One common method of minimising the impact of mechanical disruption is through the use of polymer stabilisation, as outlined in Chapter 3. This method operates by increasing the elastic modulus of the host material, increasing the resistance to stress-induced elastic deformation. This is not necessarily appropriate for sensors, as increasing the elastic modulus can lower the sensitivity of the dosimeters due to limiting the ability of the helices to respond to small changes in the geometry of the dopant.

In cases where the sensor can be encapsulated, such as the UV dosimeters discussed previously, attention must only be paid to the possibility of increased pressure affecting the value of λ_{max} , which can be avoided by the inclusion of a rigid structure within the enclosed 'cell'. Systems that are required to have open interfaces are more complex, and more vulnerable to mechanical disruption. One idea which was investigated was the use of SEM grids to act as a rigid scaffold creating open 'pixels'. This system was investigated for two key benefits it provided:

- Increased mechanical stability without affecting the elastic modulus, and therefore the sensitivity, of the device;
- Acting as a simple method of multiplexing the experiments, meaning the inclusion of small sources of distortion, such as dust particles, would not have an undue effect on the overall experiment.

Although the initial results produced were positive, this line of investigation was not continued as later experiments did not require open interfaces.

Micro-encapsulation, through the formation of polymer-dispersed liquid crystals, was also considered, but due to the random orientation of the droplets the decrease in reflective intensity was too severe to warrant further investigation.

Conclusion Overall, cross sensitivity remains the biggest challenge facing these devices. While optical applications are still possible, particularly with the ability to calibrate correctly by using a smartphone camera, chemical dosimeters remain elusive. We strongly recommend that any future work on chemical dosimeters follows the two pathways outlined above: either through the use of rapid, highly selective 'click'-style reactions, or investigation of the use of the loss of optical activity, through the creation of a plane of symmetry in a responsive dopant, as the basis on a sensor.

8.2.3 Sensitivity

Sensors and dosimeters exist with a variety of sensitivities, ranging from ultra-sensitive detection techniques to cheap, industrial sensors that are targeted to specific analyte concentration levels. In order to be relevant as a sensing platform, N* LC thin film sensors must offer significant advantages over existing technologies, either in terms of sensitivity or price. Given that it is a nascent technology, this is most easily done by focusing on a niche that is relatively underexplored, such as optical time-integrating sensors. While the applications within such a niche may be small, it does allow the technology a chance to mature in otherwise highly competitive fields.

Even within the area of optical-dosimetry, the continually decreasing price of computer systems capable of monitoring real-time sensors and determining the dose from this data means that N* LC thin films must also have competitive sensitivities. We outlined strategies for effectively screening potential sensors, so that only the most sensitive systems can be targeted for further investigation. We believe that early application of the model developed in this work is important in ensuring the efficacy of sensor research.

For systems based on a change in the value of β , we have highlighted the importance in considering not just how much the value of β changes, but that the individual values of β_i and β_f must be considered in order to have high sensitivities.

Based on this work, we can draw some general principles for these systems.

- Photo-isomerisation is highly effective as it has significant potential to drastically change the shape of the molecule. Photo-isomerisation reactions are also rapid, reducing some of the problems mentioned in Section 8.2.1.
- This technique is largely suited to larger analytes. Small analytes can only

have a minimal effect on the molecular geometry, unless they involve some radical restructuring of the dopant molecule, such as in the case of Saha et al. (2012b).

- Perhaps the best possible route for chemical dosimeters is reactions that change the interaction between the dopant and the liquid crystal. This is the basis of Saha's highly successful humidity sensor, where the major effect was not the change in molecular geometry but the change in solubility of the dopant [Saha et al. (2012a)].

8.3 Potential systems

Two key methods of accessing chemical dosimeters were mentioned in the discussion above. The first of these is in the use of highly effective and selective 'click' style reactions for the analyte-dopant interaction. The second is based on a mesophasic transition involving the creation of a plane of symmetry in a previously asymmetrical molecule.

8.3.1 'Click' reactions

In chemistry, a 'click' reaction is a chemical reaction between two moieties that proceeds rapidly to completion. There are well established criteria for a reaction to be considered a 'click' reaction. To be considered as such, a reaction must:

- be modular (consisting of joining small units together without depending on the functionality of other moieties present in the units);
- be wide in scope, not limited to specific compounds or conditions;
- give 'very high' chemical yields;

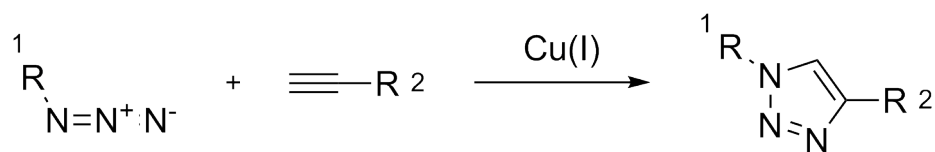


Figure 8.1: The CuAAC reaction. Unlike the Huisgen's 1,3-dipolar cycloaddition, only the 1,4-isomer is formed, fulfilling the stereospecificity requirement.

- generate non-toxic byproducts;
- produce only a single stereo-isomer;
- be stable under physiological conditions;
- exhibit a large thermodynamic driving force (defined as $\Delta H = -84 \text{ kJmol}^{-1}$) to favour a reaction with a given product;
- have a high atom economy.

There are also some conditions that, though desirable, are of secondary importance when denoting a reaction as a 'click' reaction:

- have simple reaction conditions;
- use readily available starting materials and reagents;
- use either no solvent or benign solvents (ideally water);
- not rely on chromatographic separation.

Initially, a 'click' reaction referred specifically to the copper-(I)-catalysed azide-alkyne cycloaddition (CuAAC) outlined in Figure 8.1. This reaction proceeds extremely quickly, regularly producing >95% yields.

Later, more reactions have been added to the 'click' reaction library. One of these, the thiol-ene 'click' reaction, is a suitable model system for investigating the effect of utilising a 'click' reaction-based N* LC thin film sensor (Figure 8.2).

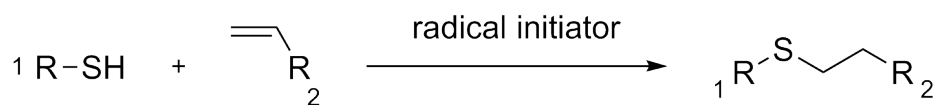


Figure 8.2: The thiol-ene ‘click’ reaction. The reaction can also proceed as a Michael addition, through the use of a nucleophile or base as a catalyst.

Thiols are an interesting target for sensors, with multiple potential applications. Thiols are responsible for the malodor associated with halitosis, as well as being a biomarker for multiple diseases (Taylor et al. (2011)).

Our suggested dopant would consist of a bridged BINOL derivative which contains an alkene moiety. The reaction is predicted to decrease the solubility of the dopant in the matrix, resulting in an increase in p as c_w increases. This is irrespective of changes in β . Basic computational chemistry can be used to determine the impact of the reaction on the dihedral angle of the BINOL, and hence the scale of the changes in β .

8.3.2 Loss of optical activity

Although it is possible to envision a situation where a sensor is constructed from an increase in optical activity, such as an enantio-selective reaction, these reaction often require stringent conditions that are not practical to carry out within a nematic host. Therefore, this section will focus on reactions that result in the loss of optical activity through the creation of a plane of symmetry in the dopant, as outlined in Figure 8.3.

The advantages of this system have been explained in detail elsewhere (see Chapter 4). It remains synthetically challenging, as off-the-shelf compounds with suitable structures do not exist. We believe that we have demonstrated the validity of investigating these dopants, and believe that they represent one of the main avenues by which commercially viable sensors could be constructed.

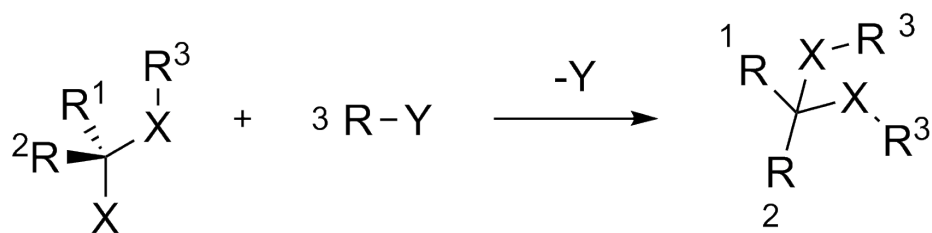


Figure 8.3: One method of decreasing the optical activity of a chiral compound is through the creation of a mirror plane. Note that a different compound, e.g. R^4-Y , would not result in the formation of a mirror plane.

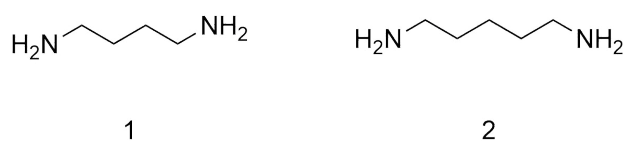


Figure 8.4: Cadaverine (**1**) and putrescine (**2**). Both molecules result from the decomposition of fish.

One advantage of these sensors, aside from the specificity they afford, is that they are believed to be the most sensitive out of the sensors modelled. This sensitivity is in part borne out by the results in Chapter 7, which operate on a similar basis. As such, it is possible to choose model systems where high sensitivity is as desirable as the specificity, so that the commercial utility of the work will still be extant even if the specificity is lower than imagined.

Based on the above, the target analytes chosen is the sensing of the amines cadaverine and putrescine, which are products in the decay of fish (Figure 8.4). While possessing a strongly notable odour which is detectable in the p.p.m. range, levels below this range are thought to be indicative of the early stages of decomposition, which could cause sickness while not possessing the characteristic pungent odour of rotting fish. These molecules also act as an effective test of the discriminatory power of systems based on a change in optical activity, due to their highly similar structure.

These systems still present some significant challenges that must be investi-

gated further. Even freshly caught fish contains putrescine and cadaverine at a < 1 p.p.m. level, so it will be difficult to determine if the level present has increased significantly over long time-scales [Doyle and Buchanan (2012)]. Other amines, notably histidine, are present at higher concentrations than the target analytes, so specificity will prove highly important in the success of such a device. Lastly, unlike in this work it will not be possible to create these systems using only ‘off-the-shelf’ compounds, so it may be desirable to create a simpler sensor to act as a proof-of-concept.

8.4 Computer simulation

One further avenue of investigation that we believe warrants investigation is the use of computational modelling to determine the properties of dopants prior to synthesis and investigation. While this is a contentious area, with limited success in accurately determining the macroscopic properties of systems simulated, it is important that future investigators make the most of this technology as it develops.

We are not far from the point where it will be possible to determine the properties of a N* LC thin film without requiring any experimentation, allowing for large scale screening of these systems prior to selecting targets. Given the substantial time that is involved in optimisation of N* LC systems, we believe that this will become vital if this field is to obtain commercial relevance, rather than remaining a laboratory curiosity.

8.5 Conclusion

Research into the use of N* LC thin films as sensors has largely been conducted on an *ad hoc* basis, with little attention paid to the underlying principles that govern

the performance of these sensors. We have sought to correct this imbalance, by constructing a framework that describes systems that are based around the use of a reactive chiral dopant.

We have also demonstrated that it is possible to perform this kind of investigation utilising simple systems that rely on commercially available compounds while still probing the reliability of the model developed. The systems chosen for investigation also were chosen specifically for having some level of commercial interest, in order to attempt to establish the commercial viability of this sensing technology.

Bibliography

- Adams, N. G. and Smith, D. (1976). The Selected Ion Flow Tube (SIFT); A Technique for Studying Ion-Neutral Reactions. *International Journal of Mass Spectrometry and Ion Physics*, 21:349–359.
- Adgate, J. L., Barteková, A., Raynor, P. C., Griggs, J. G., Ryan, A. D., Acharya, B. R., Volkmann, C. J., Most, D. D., Lai, S., and Bonds, M. D. (2009). Detection of organophosphate pesticides using a prototype liquid crystal monitor. *Journal of environmental monitoring : JEM*, 11(1):49–55.
- Armstrong, B. K. (1988). Epidemiology of Malignant Melanoma: Intermittent or Total Accumulated Exposure to the Sun? *The Journal of Dermatologic Surgery and Oncology*, 14(8):835–849.
- Arts, J. H. E., Mojet, J., van Gemert, L. J., Emmen, H. H., Lammers, J. H. C. M., Marquart, J., Woutersen, R. a., and Feron, V. J. (2002). An analysis of human response to the irritancy of acetone vapors. *Critical reviews in toxicology*, 32(1):43–66.
- Azároff, L. V. (1980). X-ray diffraction by liquid crystals. *Molecular Crystals and Liquid Crystals*, 60(1-2):73–97.
- Bauman, P., Calderer, M. C., Liu, C., and Phillips, D. (2002). The Phase Transition

- between Chiral Nematic and Smectic A * Liquid Crystals. *Archive for Rational Mechanics and Analysis*, 165(2):161–186.
- Beeckman, J., Neyts, K., and Vanbrabant, P. J. M. (2011). Liquid-crystal photonic applications. *Optical Engineering*, 50(8):081202.
- Bertocchi, G., Gottarelli, G., and Prati, R. (1984). Determination of heroin by means of the pitch of induced cholesteric mesophases. *Talanta*, 31(2):138–140.
- Bi, X., Hartono, D., and Yang, K. L. (2009). Real-time liquid crystal pH sensor for monitoring enzymatic activities of penicillinase. *Advanced Functional Materials*, 19(23):3760–3765.
- Bi, X. and Yang, K. L. (2008). Real-time liquid crystal-based glutaraldehyde sensor. *Sensors and Actuators, B: Chemical*, 134(2):432–437.
- Bloisi, F. and Vicari, L. (2003). Polymer Dispersed Liquid Crystals. In Vicari, L., editor, *Optical Applications of Liquid Crystals*, chapter 4, pages 162–215. IOP Publishing, London, 1 edition.
- Broer, D. and Heynderickx, I. (1990). Three-dimensionally ordered polymer networks with a helicoidal structure. *Macromolecules*, pages 2474–2477.
- Broer, D. J., Bastiaansen, C. M. W., Debye, M. G., and Schenning, A. P. H. J. (2012). Functional organic materials based on polymerized liquid-crystal monomers: supramolecular hydrogen-bonded systems. *Angewandte Chemie (International ed. in English)*, 51:7102–9.
- Broer, D. J., Boven, J., and Mol, G. N. (1989a). In-situ photopolymerization of an oriented liquid-crystalline acrylate, 3. Oriented polymer networks from a mesogenic diacrylate. *Die Makromolekulare Chemie*, 190(9):2255–2268.

- Broer, D. J., Finkelmann, H., and Kondo, K. (1988). In-situ photopolymerization of an oriented liquid-crystalline acrylate. *Die Makromolekulare Chemie*, 189(1):185–194.
- Broer, D. J., Mol, G. N., and Challa, G. (1989b). In situ photopolymerization of an oriented liquid-crystalline acrylate, 2. *Die Makromolekulare Chemie*, 190(1):19–30.
- Broer, D. J., Mol, G. N., and Challa, G. (1991). In-situ photopolymerization of oriented liquid-crystalline acrylates, 5. *Die Makromolekulare Chemie*, 192(1):59–74.
- Cachelin, P., Green, J. P., Peijs, T., Heeney, M., and Bastiaansen, C. W. M. (2016a). Optical Acetone Vapor Sensors Based on Chiral Nematic Liquid Crystals and Reactive Chiral Dopants. *Advanced Optical Materials*, 4(4):592–596.
- Cachelin, P., Green, J. P., Peijs, T., Heeney, M., and Bastiaansen, C. W. M. (2016b). Optical Acetone Vapor Sensors Based on Chiral Nematic Liquid Crystals and Reactive Chiral Dopants. *Advanced Optical Materials*, pages n/a–n/a.
- Cadwell, K. D., Lockwood, N. A., Nellis, B. A., Alf, M. E., Willis, C. R., and Abbott, N. L. (2007). Detection of organophosphorous nerve agents using liquid crystals supported on chemically functionalized surfaces. *Sensors and Actuators, B: Chemical*, 128(1):91–98.
- Carlisle Chambers, R., Bell, E. J., Records, T. M., Cherian, A., Ragan, K., and Swartout, B. (2007). Cholesteric liquid crystal displays as optical sensors of barbiturate binding. *Liquid Crystals*, 34(10):1221–1226.
- Carlton, R. J., Hunter, J. T., Miller, D. S., Abbasi, R., Mushenheim, P. C., Tan, L. N., and Abbott, N. L. (2013). Chemical and biological sensing using liquid crystals. *Liquid Crystals Reviews*, 1(1):29–51.

- Castellano, J. A. (2005). *Liquid Gold: The Story of Liquid Crystal Displays and the Creation of an Industry*. World Scientific Publishing Company, Singapore, 1st edition.
- Chang, C.-K., Bastiaansen, C. W. M., Broer, D. J., and Kuo, H.-L. (2012a). Discrimination of Alcohol Molecules Using Hydrogen-Bridged Cholesteric Polymer Networks. *Macromolecules*, 45(11):4550–4555.
- Chang, C. K., Chiu, S. W., Kuo, H. L., and Tang, K. T. (2012b). Cholesteric liquid crystal-carbon nanotube hybrid architectures for gas detection. *Applied Physics Letters*, 100(4):2013–2016.
- Chang, C.-K., Kuo, H.-L., Tang, K.-T., and Chiu, S.-W. (2011). Optical detection of organic vapors using cholesteric liquid crystals. *Applied Physics Letters*, 99(7):073504.
- Chang, S. J., Yin, Y. C., Lin, C. M., and Fuh, A. Y. G. (1996). Relaxation time of polymer ball type PDLC films. *Liquid Crystals*, 21(5):707–711.
- Channin, D. J. (1973). Optical waveguide modulation using nematic liquid crystal. *Applied Physics Letters*, 22(8):365–366.
- Davies, D. J. D., Vaccaro, A. R., Morris, S. M., Herzer, N., Schenning, A. P. H. J., and Bastiaansen, C. W. M. (2013). A Printable Optical Time-Temperature Integrator Based on Shape Memory in a Chiral Nematic Polymer Network. *Advanced Functional Materials*, 23(21):2723–2727.
- Dennis, L. K., VanBeek, M. J., Beane Freeman, L. E., Smith, B. J., Dawson, D. V., and Coughlin, J. A. (2008). Sunburns and risk of cutaneous melanoma, does age matter: a comprehensive meta-analysis. *Annals of Epidemiology*, 18(8):614–627.

- Dick, R. B., Setzer, J. V., Taylor, B. J., and Shukla, R. (1989). Neurobehavioural effects of short duration exposures to acetone and methyl ethyl ketone. *British Journal of Industrial Medicine*, 46(2):111–21.
- Dickert, F., Haunschild, A., and Hofmann, P. (1994). Cholesteric liquid crystals for solvent vapour detection—elimination of cross sensitivity by band shape analysis and pattern recognition. *Fresenius' Journal of Analytical Chemistry*, pages 577–581.
- Dierking, I. (2000). Polymer network-stabilized liquid crystals. *Advanced Materials*, 12(3):167–181.
- Doyle, M. P. and Buchanan, R. L., editors (2012). *Food Microbiology: Fundamentals and Frontiers*. American Society of Microbiology Press, Washington, D.C., 4th ed. edition.
- Drzaic, P. S. (1986). Polymer dispersed nematic liquid crystal for large area displays and light valves. *Journal of Applied Physics*, 60(6):2142.
- Eelkema, R. and Feringa, B. L. (2005). Macroscopic expression of the chirality of amino alcohols by a double amplification mechanism in liquid crystalline media. *Journal of the American Chemical Society*, 127(39):13480–13481.
- Eelkema, R. and Feringa, B. L. (2006). Amplification of chirality in liquid crystals. *Organic & biomolecular chemistry*, 4(20):3729–45.
- Fasel, R., Parschau, M., and Ernst, K.-H. (2006). Amplification of chirality in two-dimensional enantiomorphous lattices. *Nature*, 439(7075):449–452.
- Fergason, J. L. (1964). Liquid Crystals. *Scientific American*, 211(2):76–85.
- Fergason, J. L., Goldberg, N. N., and Nadalin, R. J. (1966). Cholesteric Structure-II Chemical Significance. *Molecular Crystals*, 1(2):309–323.

- Fuh, A. Y.-G., Lee, C.-R., and Ho, Y.-H. (2002). Thermally and electrically switchable gratings based on polymer-ball-type polymer-dispersed liquid-crystal films. *Applied optics*, 41(22):4585–4589.
- Fujino, A., Satoh, T., Takebayashi, T., Nakashima, H., Sakurai, H., Higashi, T., Matumura, H., Minaguchi, H., and Kawai, T. (1992). Biological monitoring of workers exposed to acetone in acetate fibre plants. *British Journal of Industrial Medicine*, 49(9):654–7.
- Fung, Y. K., Yang, D.-K., Ying, S., Chien, L.-C., Zumer, S., and Doane, J. W. (1995). Polymer networks formed in liquid crystals. *Liquid Crystals*, 19(6):797–801.
- Gonzalez, C. L., Bastiaansen, C. W. M., Lub, J., Loos, J., Lu, K., Wondergem, H. J., and Broer, D. J. (2008). Nanoporous membranes of hydrogen-bridged smectic networks with nanometer transverse pore dimensions. *Advanced Materials*, 20(7):1246–1252.
- Gottarelli, G., Hibert, M., Samori, B., Solladi, G., Spada, G. P., and Zimmermann, R. (1983). Induction of the Cholesteric Mesophase in Nematic Liquid Crystals : Mechanism and Application to the Determination of Bridged Biaryl Configurations. *J. Am. Chem. Soc.*, 105(11):7318–7321.
- Gottarelli, G., Spada, G. P., Bartsch, R., Solladi, G., and Zimmermann, R. (1986). Induction of the cholesteric mesophase in nematic liquid crystals: correlation between the conformation of open-chain chiral 1,1'-binaphthyls and their twisting powders. *The Journal of Organic Chemistry*, 51(5):589–592.
- Gray, G. W. (1962). *Molecular Structure and the Properties of Liquid Crystals*. Academic Press, London, 2nd edition.

- Gray, G. W., Hartley, J. B., and Jones, B. (1955). Mesomorphism and chemical constitution. Part V. The mesomorphic properties of the 4'-n-alkoxydiphenyl-4-carboxylic acids and their simple alkyl esters. *Journal of the Chemical Society (Resumed)*, (1412):1412–1420.
- Gunning, W. and Pasko, J. (1981). A Liquid Crystal Tunable Spectral Filter: Visible And Infrared Operation. In Norris, D. D., editor, *Proceedings of SPIE*, volume 268, pages 190–194.
- Han, G.-R., Song, Y.-J., and Jang, C.-H. (2014). Label-free detection of viruses on a polymeric surface using liquid crystals. *Colloids and surfaces. B, Biointerfaces*, 116:147–52.
- Han, Y., Pacheco, K., Bastiaansen, C. W. M., Broer, D. J., and Sijbesma, R. P. (2010a). Optical monitoring of gases with cholesteric liquid crystals. *Journal of the American Chemical Society*, 132(9):2961–7.
- Han, Y., Pacheco, K., Bastiaansen, C. W. M., Broer, D. J., and Sijbesma, R. P. (2010b). Optical monitoring of gases with cholesteric liquid crystals. *Journal of the American Chemical Society*, 132(9):2961–7.
- Hardeberg, J. Y., Schmitt, F., and Brettel, H. (2002). Multispectral color image capture using a liquid crystal tunable filter. *Optical Engineering*, 41(10):2532.
- Herzer, N., Guneyusu, H., Davies, D. J. D., Yildirim, D., Vaccaro, A. R., Broer, D. J., Bastiaansen, C. W. M., and Schenning, A. P. H. J. (2012). Printable optical sensors based on H-bonded supramolecular cholesteric liquid crystal networks. *Journal of the American Chemical Society*, 134:7608–11.

- Heynderickx, I. and Broer, D. J. (1991). The Use of Cholesterically-Ordered Polymer Networks in Practical Applications. *Molecular Crystals and Liquid Crystals*, 203(1):113–126.
- Hikmet, R. A. M. (1991). Anisotropic gels and plasticized networks formed by liquid crystal molecules. *Liquid Crystals*, 9(3):405–416.
- Hikmet, R. A. M. and Howard, R. (1993). Structure and properties of anisotropic gels and plasticized networks containing molecules with a smectic- A phase. *Physical Review E*, 48(4):2752–2759.
- Hikmet, R. A. M. and Zwerver, B. H. (1991). Cholesteric Networks Containing Free Molecules. *Molecular Crystals and Liquid Crystals*, 200(1):197–204.
- Hu, W., Cao, H., Song, L., Zhao, H., Li, S., Yang, Z., and Yang, H. (2009). Thermally controllable reflective characteristics from rupture and self-assembly of hydrogen bonds in cholesteric liquid crystals. *The journal of physical chemistry. B*, 113(42):13882–5.
- Ichimura, K., Seki, T., Hosokita, A., and Aoki, K. (1988). Reversible Change in Alignment Mode of Nematic Liquid Crystals Regulated Photochemically by “Command Surfaces” Modified with an Azobenzene Monolayer. *Langmuir*, 1216(1):1214–1216.
- Ireland, P. T. and Jones, T. V. (1987). The response time of a surface thermometer employing encapsulated thermochromic liquid crystals. *Journal of Physics E: Scientific Instruments*, 20:1195–1199.
- Irie, M., Yoshida, K., and Hayashi, K. (1977). Laser Photolysis Study of the Photoracemization of 1'1-Binaphthyl. *The Journal of Physical Chemistry*, 81(6):969–972.

- James, T. D., Harada, T., and Shinkai, S. (1993). Determination of the absolute configuration of monosaccharides by a colour change in a chiral cholesteric liquid crystal system. *Journal of the Chemical Society, Chemical Communications*, (10):857.
- Jones, C. H., Ferguson, J. L., and Asars, J. A. (1965). Investigations of Large-Area Display Screen Using Liquid Crystals. *RADC Report*, (TR 54):274.
- Kaafarani, B. R. (2011). Discotic liquid crystals for opto-electronic applications. *Chemistry of Materials*, 23(3):378–396.
- Kato, T. and Frechet, J. M. J. (1989). Stabilization of a liquid-crystalline phase through noncovalent interaction with a polymer side chain. *Macromolecules*, 22(9):3818–3819.
- Kawamoto, H. (2006). The History of Liquid-Crystal Displays. *Proceedings of the IEEE*, 90(4):460–500.
- Kirchner, N., Zedler, L., Mayerhöfer, T. G., and Mohr, G. J. (2006). Functional liquid crystal films selectively recognize amine vapours and simultaneously change their colour. *Chemical communications (Cambridge, England)*, (14):1512–4.
- Knobloch, H., Orendi, H., Buchel, M., Seki, T., Ito, S., and Knoll, W. (1995). Photochromic command surface induced switching of liquid crystal optical waveguide structures. *Journal of Applied Physics*, 77(2):481–487.
- Konforti, N., Marom, E., and Wu, S. T. (1988). Phase-only modulation with twisted nematic liquid-crystal spatial light modulators. *Optics letters*, 13(3):251–253.

- Kopp, V. I., Zhang, Z. Q., and Genack, A. Z. (2003). Lasing in chiral photonic structures.
- Kreuzer, M., Tschudi, T., De Jeu, W. H., and Eidenschink, R. (1993). New liquid crystal display with bistability and selective erasure using scattering in filled nematics. *Applied Physics Letters*, 62(1993):1712–1714.
- Kumagai, S., Matsunaga, I., and Tabuchi, T. (1998). Effects of variation in exposure to airborne acetone and difference in work load on acetone concentrations in blood, urine, and exhaled air. *American Industrial Hygiene Association Journal*, 59(4):242–51.
- Kumar, S., Wachtel, E. J., and Keinan, E. (1993). Hexaalkoxytricycloquinazolines: new discotic liquid crystals. *The Journal of Organic Chemistry*, 58(15):3821–3827.
- Kyba, E. B., Koga, K., Sousa, L. R., Sigel, M. G., and Cram, D. J. (1973). Chiral Recognition in Molecular Complexing. *Journal of the American Chemical Society*, 97:2692–2693.
- Kyushiki, H. and Ikai, A. (1990). The effect of solvent viscosity on the rate-determining step of fatty acid synthetase. *Proteins: Structure, Function, and Bioinformatics*, 8(3):287–293.
- Lackner, A. M., Margerum, J. D., Ramos, E., and Lim, K.-C. (1989). Droplet size control in polymer dispersed liquid crystal films. *SPIE Proceedings*, 1080:53–61.
- Lai, Y.-T., Kuo, J.-C., and Yang, Y.-J. (2014). A novel gas sensor using polymer-dispersed liquid crystal doped with carbon nanotubes. *Sensors and Actuators A: Physical*, 215:83–88.

- Larsen, T., Bjarklev, A., Hermann, D., and Broeng, J. (2003). Optical devices based on liquid crystal photonic bandgap fibres. *Optics express*, 11(20):2589–2596.
- Lockwood, N. A., Gupta, J. K., and Abbott, N. L. (2008). Self-assembly of amphiphiles, polymers and proteins at interfaces between thermotropic liquid crystals and aqueous phases. *Surface Science Reports*, 63:255–293.
- Madsen, L. A., Dingemans, T. J., Nakata, M., and Samulski, E. T. (2004). Thermotropic biaxial nematic liquid crystals. *Physical Review Letters*, 92(14):145505–1.
- Mertz, E., Beil, J. B., and Zimmerman, S. C. (2003). Kinetics and thermodynamics of amine and diamine signaling by a trifluoroacetyl azobenzene reporter group. *Organic letters*, 5(17):3127–3130.
- Mujahid, A., Stathopoulos, H., Lieberzeit, P. A., and Dickert, F. L. (2010). Solvent Vapour Detection with Cholesteric Liquid Crystals—Optical and Mass-Sensitive Evaluation of the Sensor Mechanism.
- Nishi, T., Ikeda, A., Matsuda, T., and Shinkai, S. (1991). Detection of chirality by colour. *Journal of the Chemical Society, Chemical Communications*, (5):339.
- Paleos, C. M. and Tsiourvas, D. (1995). Thermotropic Liquid Crystals Formed by Intermolecular Hydrogen Bonding Interactions. *Angewandte Chemie International Edition in English*, 34(16):1696–1711.
- Palmans, A. R. A. and Meijer, E. W. (2007). Amplification of chirality in dynamic supramolecular aggregates. *Angewandte Chemie - International Edition*, 46(47):8948–8968.

- Pasechnik, S. V., Chigrinov, V. G., and Shmeliyova, D. V. (2009). *Liquid Crystals: Viscous and Elastic Properties*. Wiley-VCH, Weinheim, 1 edition.
- Podolsky, D., Banji, O., and Rudquist, P. (2008). Simple method for accurate measurements of the cholesteric pitch using a “stripe–wedge” Grandjean–Cano cell. *Liquid Crystals*, 35(7):789–791.
- Poziomek, E. J., Novak, T. J., and Mackay, R. a. (1974). Use of Liquid Crystals as Vapor Detectors. *Molecular Crystals and Liquid Crystals*, 27(1-2):175–185.
- Rameshbabu, K., Urbas, A., and Li, Q. (2011). Synthesis and characterization of thermally irreversible photochromic cholesteric liquid crystals. *Journal of Physical Chemistry B*, 115(13):3409–3415.
- Reinitzer, F. (1888). *Beiträge zur Kenntniss des Gholesterins*.
- Righettoni, M., Tricoli, A., Gass, S., Schmid, A., Amann, A., and Pratsinis, S. E. (2012). Breath acetone monitoring by portable Si:WO₃ gas sensors. *Analytica chimica acta*, 738:69–75.
- Rollo, J. (1798). *An Account of Two Cases of Diabetes Mellitus*. T. Gillet, The Poultry, London, 1st edition.
- Sage, I. (2011). Thermochromic liquid crystals. *Liquid Crystals*, 38(11-12):1551–1561.
- Saha, A., Tanaka, Y., Han, Y., Bastiaansen, C. M. W., Broer, D. J., and Sijbesma, R. P. (2012a). Irreversible visual sensing of humidity using a cholesteric liquid crystal. *Chemical Communications*, 48(38):4579.
- Saha, A., Tanaka, Y., Han, Y., Bastiaansen, C. M. W., Broer, D. J., and Sijbesma, R. P. (2012b). Irreversible visual sensing of humidity using a cholesteric liquid crystal. *Chemical communications (Cambridge, England)*, 48(38):4579–81.

- Sayre, R. M., Desrochers, D. L., Wilson, C. J., and Marlowe, E. (1981). Skin type, minimal erythema dose (MED), and sunlight acclimatization. *Journal of the American Academy of Dermatology*, 5(4):439–443.
- Shah, R. R. and Abbott, N. L. (2001). Principles for measurement of chemical exposure based on recognition-driven anchoring transitions in liquid crystals. *Science (New York, N.Y.)*, 293(5533):1296–9.
- Shah, R. R. and Abbott, N. L. (2003). Orientational Transitions of Liquid Crystals Driven by Binding of Organoamines to Carboxylic Acids Presented at Surfaces with Nanometer-Scale Topography. *Langmuir*, 19:275–284.
- Shinkai, S., Nishi, T., Ikeda, A., Matsuda, T., Shimamoto, K., and Manabe, O. (1990). Crown-metal interactions in cholesteric liquid crystals. *Journal of the Chemical Society, Chemical Communications*, 1(4):303.
- Shinkai, S., Shimamoto, K., Manabe, O., and Sisido, M. (1989). Selective Ion Permeation Across Membranes Containing Crown Ethers With Steroid Moieties. *Die Makromolekulare Chemie, Rapid Communications*, 10(7):361–366.
- Singh, S. (2002). *Liquid Crystals-Fundamentals*. World Scientific Publishing Company, Singapore, 1st edition.
- Smith, D. and Španěl, P. (2005). Selected ion flow tube mass spectrometry (SIFT-MS) for on-line trace gas analysis. *Mass Spectrometry Reviews*, 24(5):661–700.
- Solntsev, K. M., Bartolo, E.-A., Pan, G., Muller, G., Bommireddy, S., Huppert, D., and Tolbert, L. M. (2009). Excited-State Proton Transfer in Chiral Environments: Photoracemization of BINOLs. *Israel Journal of Chemistry*, 49(2):227–233.

- Sousa, M. E., Broer, D. J., Bastiaansen, C. W. M., Freund, L. B., and Crawford, G. P. (2006). Isotropic "Islands" in a cholesteric "Sea": Patterned thermal expansion for responsive surface topologies. *Advanced Materials*, 18(14):1842–1845.
- Spaněl, P., Dryahina, K., Rejšková, A., Chippendale, T. W. E., and Smith, D. (2011). Breath acetone concentration; biological variability and the influence of diet. *Physiological Measurement*, 32(8):N23–31.
- Stumpel, J. E., Gil, E. R., Spoelstra, A. B., Bastiaansen, C. W. M., Broer, D. J., and Schenning, A. P. H. J. (2015). Stimuli-Responsive Materials Based on Interpenetrating Polymer Liquid Crystal Hydrogels. *Advanced Functional Materials*, 25(22):3314–3320.
- Sutarlie, L., Qin, H., and Yang, K.-L. (2010). Polymer stabilized cholesteric liquid crystal arrays for detecting vaporous amines. *The Analyst*, 135(7):1691.
- Tan, H., Li, X., Liao, S., Yu, R., and Wu, Z. (2014). Highly-sensitive liquid crystal biosensor based on DNA dendrimers-mediated optical reorientation. *Biosensors & Bioelectronics*, 62:84–9.
- Tang, L., Li, Y., Xu, K., Hou, X., and Lv, Y. (2008). Sensitive and selective acetone sensor based on its cataluminescence from nano-La₂O₃ surface. *Sensors and Actuators, B: Chemical*, 132(1):243–249.
- Taylor, P., Fenske, J. D., and Paulson, S. E. (2011). Human Breath Emissions of VOCs Human Breath Emissions of VOCs. (October 2012):37–41.
- Thomsen, D. L., Keller, P., Naciri, J., Pink, R., Jeon, H., Shenoy, D., and Ratna, B. R. (2001). Liquid crystal elastomers with mechanical properties of a muscle. *Macromolecules*, 34(17):5868–5875.

- Tkachenko, V., Abbate, G., Marino, A., Vita, F., Giocondo, M., Mazzulla, A., Ciuchi, F., and Stefano, L. D. (2006). Nematic liquid crystal optical dispersion in the visible-near infrared range. *Molecular Crystals and Liquid Crystals*, 454(1):263/[665]–271/[673].
- Toliver, W. H., Ferguson, J. L., Sharpless, E., and Hoffman, P. E. (1970). Liquid crystal trace contaminant vapor detector with an electronic input. *Aerospace Medicine*, 41:18–20.
- van Oosten, C. L., Bastiaansen, C. W. M., and Broer, D. J. (2009). Printed artificial cilia from liquid-crystal network actuators modularly driven by light. *Nature Materials*, 8(8):677–682.
- van Oosten, C. L., Harris, K. D., Bastiaansen, C. W. M., and Broer, D. J. (2007). Glassy photomechanical liquid-crystal network actuators for microscale devices. *The European Physical Journal. E, Soft Matter*, 23:329–336.
- Wang, C. and Mbi, A. (2007). A new acetone detection device using cavity ring-down spectroscopy at 266 nm: evaluation of the instrument performance using acetone sample solutions. *Measurement Science and Technology*, 18(8):2731–2741.
- Wang, C., Mbi, A., and Shepherd, M. (2010). A study on breath acetone in diabetic patients using a cavity ringdown breath analyzer: Exploring correlations of breath acetone with blood glucose and. *IEEE Sensors Journal*, 10(1):54–63.
- Wang, L., Yun, X., Stanacevic, M., Gouma, P. I., Pardo, M., and Sberveglieri, G. (2009). An Acetone Nanosensor For Non-invasive Diabetes Detection. *AIP Conference Proceedings*, 206(1):206–208.
- Wigaeus, E., Holm, S., and Åstrand, I. (1981). Exposure to acetone. Uptake and

- elimination in man. *Scandinavian Journal of Work, Environment & Health*, 7(2):84–94.
- Wilson, M. R. and Earl, D. J. (2001). Calculating the helical twisting power of chiral dopants. *Molecular Topology in Liquid Crystals Materials Chemistry Discussion No 4 Meeting*, (July):2672–2677.
- Winterbottom, D. A., Narayanaswamy, R., and Raimundo, I. M. (2003). Cholesteric liquid crystals for detection of organic vapours. *Sensors and Actuators, B: Chemical*, 90(1-3):52–57.
- Wrenn, K. D., Slovis, C. M., Minion, G. E., and Rutkowski, R. (1991). The syndrome of alcoholic ketoacidosis. *The American Journal of Medicine*, 91(2):119–128.
- Wu, S. T. (1989). Design of a liquid crystal based tunable electrooptic filter. *Applied Optics*, 28(1):48–52.
- Yamagishi, F. G., Miller, L. J., and van Ast, C. I. (1989). Morphological control in polymer-dispersed liquid crystal film matrices. *SPIE Proceedings*, 1080:24–31.
- Yamaguchi, R., Ookawara, H., and Sato, S. (1992). Thermally Addressed Polymer Dispersed Liquid Crystal Displays. *Japanese Journal of Applied Physics*, 31(Part 2, No. 8A):L1093–L1095.
- Yashima, E., Maeda, K., and Nishimura, T. (2004). Detection and Amplification of Chirality by Helical Polymers. *Chemistry - A European Journal*, 10(1):42–51.
- Yu, L. J. and Saupe, A. (1980). Observation of a biaxial nematic phase in potassium laurate-1-decanol-water mixtures. *Physical Review Letters*, 45(12):1000–1003.

- Zakerhamidi, M., Shoarinejad, S., and Mohammadpour, S. (2014). Fe₃O₄ nanoparticle effect on dielectric and ordering behavior of nematic liquid crystal host. *Journal of Molecular Liquids*, 191:16–19.
- Zhang, M. and Schuster, G. B. (1992). Photoracemization of optically active 1,1'-binaphthyl derivatives: light-initiated conversion of cholesteric to compensated nematic liquid crystals. *The Journal of Physical Chemistry*, 96(7):3063–3067.
- Zhang, R., Deng, H., Valenca, R., Jin, J., Fu, Q., Bilotti, E., and Peijs, T. (2012). Carbon nanotube polymer coatings for textile yarns with good strain sensing capability. *Sensors and Actuators A: Physical*, 179:83–91.
- Zhong, S. and Jang, C.-H. (2014). Highly sensitive and selective glucose sensor based on ultraviolet-treated nematic liquid crystals. *Biosensors & bioelectronics*, 59:293–9.
- Zhu, Y., Shi, J., Zhang, Z., Zhang, C., and Zhang, X. (2002). Development of a Gas Sensor Utilizing Chemiluminescence on Nanosized Titanium Dioxide. *Analytical Chemistry*, 74(1):120–124.
- Ziem, G. E. and Castleman, B. I. (1989). Threshold Limit Values: Historical Perspectives and Current Practice. *Journal of Occupational Medicine*, 31(11):910–918.